Doctoral Dissertation

New strategies in the treatment of radioresistant tumor cells by using synchrotron radiation and metallic compounds

Sílvia Gil Duran

Centre d'Estudis en Biofísica,

Departament de Bioquímica i Biologia Molecular

Universitat Autònoma de Barcelona

Ph.D. Advisor: **Dr. Manel Sabés**

Ph.D. Co-Advisor: **Dra. Yolanda Prezado**

July 2012

Universitat Autònoma de Barcelona

NEW STRATEGIES IN THE TREATMENT OF RADIORESISTANT TUMOR CELLS BY USING SYNCHROTRON RADIATION AND METALLIC COMPOUNDS

Memòria presentada per Sílvia Gil Duran per optar al grau de doctora.

Aquesta tesi ha estat realitzada al Centre d'Estudis en Biofísica del Departament de Bioquímica i Biologia Molecular de la Universitat Autònoma de Barcelona, sota la direcció del Dr. Manel Sabés Xamaní (Centre d'Estudis en Biofísica, UAB) i la co-direcció de la Dra. Yolanda Prezado Alonso (*Centre National de la Recherche Scientifique*, França).

Vist-i-plau del director i co-director,

Dr. Manel Sabés

Dra. Yolanda Prezado

Bellaterra, juliol del 2012

Agraïments

En primer lloc vull agrair als meus directors, el Manel Sabés i la Yolanda Prezado, l'oportunitat de realitzar aquesta tesi amb ells, així com tot el que m'han ensenyat durant aquests quatre anys. Em sento una afortunada per haver pogut treballar amb vosaltres! Moltes gràcies igualment a la Fundació Oncològica de Catalunya per confiar sempre en el projecte i financiar-lo.

Un agraïment enorme a tota la gent amb la que he tingut l'honor de treballar en el CEB, l'ESRF, i el CENBG, per l'ajut que m'heu ofert, i pels bons moments que hem viscut junts. Agrair també la paciència i la bona disposició de tot el personal de radioteràpia oncològica de l'Hospital Clínic de Barcelona, i al Sergi Segarra per tots els comentaris propostos en ortografia i gramàtica.

Per descomptat agrair també als amics que sempre esteu quan se us necessita, i que heu viscut d'aprop les bones i les no tan bones èpoques d'aquests quatre anys. Gràcies per la vostra paciència i optimisme i per no donar-me per perduda tot i els meus possibles deliris en moments puntuals...

Moltes gràcies a la meva família (als que hi són i als que hi són d'una altra manera) per estar incondicionalment amb mi, i donar-me verdaderes lliçons de vida. Moltes gràcies als meus pares, la Montse i l'Albert, per ser els meus metges, els meus cuiners, els meus psicòlegs, i en definitiva, per ser el mirall en el que intento reflexar-me cada dia. Per últim, vull agrair-li al Carles TOT el que ha fet per mi i pel "nostre" doctorat durant aquests anys. No només m'ha animat i encoratjat en tot el que he emprès, sinó que a més va acceptar que un tercer s'immiscuís entre nosaltres: l'Skype.

De nou, MOLTES GRÀCIES a tots!

INDEX

CHAPTER V. Results: *In vivo* experiments

CHAPTER VI. Final conclusions

APPENDICES

List of abbreviations

AIFIRA	*Applications Interdisciplinaires des Faisceaux d'Ions en Région Aquitaine*
BB	white Broad Beam
BBB	Blood Brain Barrier
BNCT	Boron Neutron Capture Therapy
BNL	Brookhaven National Laboratory
BS	Backscattering Spectrometry
BSA	Bovine Serum Albumine
CENBG	*Centre D'Etudes Nucléaires Bordeaux-Gradignan*
CNS	Central Nervous System
COE	Clinical Orthovoltage Equipment
c-t-c	center-to-center distance
DEF	Dose Enhancement Factor
DNA	Deoxyribonucleic Acid
DSB	Double-Strand Break
eq.	equation
ESRF	European Synchrotron radiation Facility
FA	Formaldehid
FITC	Fluorescein Isothiocyanate
FSC	Forward Scattering
GB	Glioblastoma
GBM	Glioblastoma Multiforme
HR	Homologous Recombination
HVL	Half Value Layer
ICP-MS	Inductively Coupled Plasma Mass Spectrometry
ICN	*Institut Català de Nanotecnologia*
ILS	Increased Life Span
ID	Insertion Device
IF	Immunofluorescence
IR	Infrared radiation
i.v.	intravenous
LET	Linear Energy Transfer
LUV	Large Unilamellar Vesicle
MBRT	Minibeam Radiation Therapy
MGMT	O^6-methylguanine-DNA-methyltransferase
MeST	Median Survival Time
MLV	Large Multilamellar Vesicle
MRT	Microbeam Radiation Therapy
MT	Metallothionenins
NER	Nucleotide Excission Repair
NHEJ	Non-Homogeneous End Joining
NI	Nano-Imaging
NP	Nanoparticle
ICP-OES	Inductively Coupled Plasma Optical Emission Spectrometry
PAT	Photon Activation Therapy
PBS	Polyphosphate Buffered Saline
PC	Phosphatidylcholine
PI	Propidium Iodide
PIXE	Proton Induce X-ray Emission
PMMA	Polymethyl Methacralate
ppb	parts per billion
PS	Phosphatidylserine
PVDR	Peak-to-Valley Dose Ratio
RBE	Relative Biological Effectiveness
ROS	Radical Oxygen Specie
RT	Radiotherapy
SE	Standard Error
Ser	Serine
SD	Standard Deviation
SR	Synchrotron Radiation
SSB	Single-Strand Break
SSC	Side Scattering
SSD	Source-Surface Distance
SSRT	Stereotactic Synchrotron Radiation Therapy
SUV	Small Unilamellar Vesicle
TMZ	Temozolomide

Units

Gy	**Gray**
h	hour
min	minute
s	second
J	**Joule**
kg	kilogram
g	**gram**
mg	milligram
µg	microgram
ng	nanogram
l	**liter**
ml	milliliter
µl	microliter
m	**meter**
mm	millimeter
µm	micrometer
nm	nanometer
MeV	Megaelectronvolts
keV	kiloelectronvolts
eV	**electronvolts**
mA	milliampere
nA	nanoampere
mM	millimolar
µM	micromolar
nM	nanomolar
MV	Megavoltage/Megavolts
kV	kilovoltage/kilovolts
v/v	**volume/volume**
rad	**radians**

Symbols

Au	Gold
Al	Aluminium
B	Boron
Be	Beryllium
C	Carbon
Ca	Calcium
cisPt	cisplatin
Cu	Copper
CsBr	Cesium bromide
Fe	Iron
Gd	Gadolinium
H	Hydrogen
H^+	Proton
He	Helium
HNO_3	Nitric acid
H_2O	Water
I	Iodine
Ir	Iridium
K	Potassium
N	Nitrogen
Na	Sodium
NaCl	Sodium chloride
O	Oxygen
Si	Silicon
Tl	Thallium
transPt	Transplatin
Zn	Zinc
ZnTe	Zinc tellurium

Preface

Glioblastoma and glioblastoma multiforme are the most common adult brain tumors, and also ones of the most lethal despite modern treatments. The high morbidity of the surrounding healthy tissues arises as the main obstacle to reach a curative treatment in conventional radiotherapy. The gold standard treatment based on temozolomide followed by a complete brain irradiation provides only a slight increase of survival (Stup *et al.* 2005). To overcome these limitations, new radiotherapy approaches are under development at synchrotron sources.

The distinct features of the synchrotron radiation (high brilliance and low angular divergence) allow to explore new avenues.

- Novel protocols based on the incorporation of high-Z atoms in the tumors prior irradiations.

These techniques consist in loading the tumor with a chemical compound containing a high-Z atom and irradiating it with monochromatic kilovoltage X-rays.

When the high-Z element is administered in form of contrast agent, the subsequent increase of the photoelectric effect leads to a local dose enhancement in the tumor. In the case of a high-Z element forming part of a chemotherapy drug, the small concentration achievable in the cells due to its high cytotoxicity led to question whether the increase in treatment effectiveness was due to the dose deposition of Auger electrons near/into the cell DNA or to a radiosensitization effect.

- Spatial fractionation of the dose.

The way that the dose is deposited is known to have an impact on tissue response to radiation. Indeed, healthy tissue exhibits a remarkable ability to recover after very high doses of radiation (> 100 Gy in one fraction) when submillimetric irradiation field sizes and a spatial fractionation of the dose are employed. This phenomenon was firstly observed in preclinical trials with Microbeam Radiation Therapy (MRT), in which 50-µm wide beams were used.

One pioneer experiment in 2006, seemed to indicate that the use of thicker beams of around 600 µm still keeps (part of) the high healthy tissue sparing capability observed in MRT.

The possibility of extending the so-called Minibeam Radiation Therapy (MBRT) outside the synchrotron sources with modified X-ray equipment triggered its implementation at the ESRF.

The different beam widths and spacing in MRT and MBRT might lead to completely different biological effects. Hence, *in vitro* and *in vivo* experiments were warranted to understand the effects of MBRT. In this frame, this Ph.D. thesis compiles all the results of one of the first *in vitro* experiments with MBRT. The main objectives were:

1) to detect and quantify different kinds of cell damage after MBRT irradiations,
2) to compare them with those caused by white broad beam (BB) irradiations,
3) to estimate the endpoints and delimit to some extent the range of doses where the therapeutic window (i.e., endpoint) for a new treatment could be expected. This would help to better design experiments with small animals, and
4) to study possible ways to increase the therapeutic index of gliomas treatments by using compounds containing high-Z atoms as cisplatin (cisPt) concomitantly to radiation.

In addition, new strategies were investigated in order to reduce the cisPt cytotoxicity. Those included the use of biological-like vesicles, named liposomes, to improve the drug delivery into the cells, whereas decreasing the cisPt toxicity on healthy cells. To better understand the effects of liposomes, the concentration and distribution of Pt inside both alive and dead cells were analyzed after this treatment. Indeed, it was the first time that dead cells were studied. Another alternative explored was the reduction of cisPt concentration by combining cisPt with the promising gold nanoparticles (AuNPs).

Finally, the tolerance doses on healthy rat brains were investigated. Therefore, it could be demonstrated not only the effectiveness of MBRT in killing glioma cells, but also the sparing capability of healthy tissues after such irradiations.

This Ph.D. manuscript is organized in the following way:

- The first part (Chapter I) provides an introduction to the main topics that will be dealed through the thesis, i.e., the difficulties to treat gliomas, fundamentals of radiotherapy techniques, an overview of synchrotron sources, etc.

- In the second part (Chapter II), all the procedures and techniques used in this thesis are described. It comprises cell cultures, the different post-treatment cell analyses, the irradiation features (dosimetry and set-up), etc.

- The third part (from Chapter III to IV) reports all the results obtained *in vitro*, concerning the effectiveness of the different radiation treatments (white MBRT and BB synchrotron radiation, monochromatic X-rays exposures, irradiations with COE), alone or concomitantly to cisPt administration. Moreover, new strategies such as cisPt combined with AuNPs and cisPt associated to liposomes are also investigated in this part.

- In the fourth part (Chapter V) the study of dose tolerances of healthy rat brains and the effects obtained after MBRT exposures will be presented.

- Finally, the main conclusions and repercussion of this Ph.D. dissertation in publications and congresses are exposed.

CHAPTER I. Introduction

1 Introduction. Gliomas and treatments

1.1 Cancer: A very brief overview

Cancer is a general name for more than 100 diseases characterized by abnormal cellular proliferation leading to the formation of tumors, which often invade normal surrounding tissue. This process is called carcinogenesis. Malignant tumors have the ability to metastasize, i.e., to spread to a site in the body distant from the primary site through the bloodstream and lymphatic system. Around 80% of cellular mutations are caused by external factors such as sunlight, radiation or cigarrette smoke, whereas 20% of cases arise from random mutations that occur during normal cellular replication (Washington & Leaver 2009).

Data provided by European Comission pointed at cancer as the second most common cause of death in the European Union (ec.europa.eu). Cancer treatment highly depends on tumor type, location and patient conditions. Surgery, radiotherapy and chemotherapy constitute the most frequent treatments. In addition, it is common to combine all or several of these techniques.

However, despite the great improvements in the treatment of cancer, the outcome of some tumors remains unsatisfactory. This is the case of high-grade gliomas, a cancer of glial cells, which is the most frequent and aggressive type of brain tumor. In Spain, according to the data provided by *Asociación Española Contra el Cáncer* (AECC), gliomas have an incidence of 8.7 for 100,000 inhabitants/year in males, and 5.4 in females (www.aecc.es). This kind of tumors, as well as its main features are further described through the next section.

1.1.1 Gliomas

The central nervous system (CNS) is composed of two structures: the brain and the spinal cord. The latter one begins below the base of the skull and extends downward, protected by the vertebral column. It is mainly responsible for the connection between brain and muscles. Both brain and spinal cord are externally protected by the cranial bones, meninges and cerebrospinal fluid (Washington & Leaver 2009).

The brain is formed by three components: the cerebrum (also called brain), the cerebellum and the brainstem (Figure 1.1).

The cerebrum or brain is one of the most complex organs in the body, being the center of memory, learning, reasoning, judgement, intelligence and emotions. The cerebellum plays a major role in the coordination of voluntary muscular movement and in body balance. Interconnection between the brain and spinal cord is established through the brainstem (Washington & Leaver 2009).

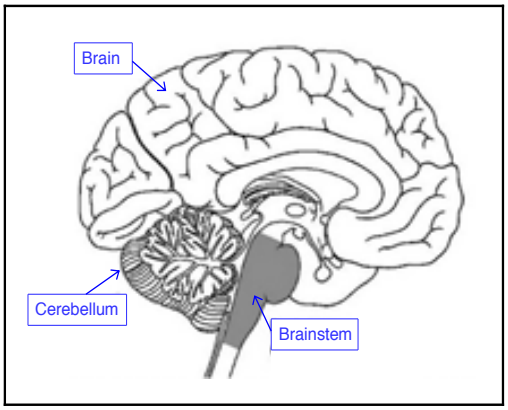

Figure 1.1. *Composition of the brain, the cerebellum and the brainstem*.

The core component of CNS is a kind of non-proliferating in adults end cells called neurons. They are highly specialized cells, which are able to process and to transmit information to other nerve cells through its cable-like extensions or axons. The process is named synapses (Hall & Giaccia 2006). Besides neurons, the CNS is composed of 60% white matter and 40% gray matter or glia (Washington & Leaver 2009).

White matter comprises bundles of nerve fibers, axons and dendrites in charge of carrying impulses toward the cell body (Washington & Leaver 2009). They are depicted in Figure 1.2. Glia is considered as connective elements in the CNS that fill the space between nerve elements (Zhang 2001). Glial cells not only connect the nerve elements together, but also guide neuronal migration, remove damaged cells and form part of blood-brain barrier (BBB), which will be decribed at the end of this section. Thus, glia maintains the homeostatic environment for appropiate functions of neuronal cells. Moreover, a proportion of 10:1 of glial cells with respect to neurons is estimated (Zhang 2001).

There are at least three kinds of glial cells in the CNS (see Figure 1.2): microglia, astrocytes and oligodendrocytes (Zhang 2001, Washington & Leaver 2009):

- Microglia: they constitute 20% of the total glial cell population of the brain. These type of cells act as macrophagues, being the first and main form of active immune defense in the CNS.

- Astrocytes: these star-shaped cells are found between neurons and blood vessels and they provide support to neurons, regulating also the transport of ions. They control the release of growth factors which allow the reparation of neuronal connections after brain damage.

- Oligodendrocytes: they resemble astrocytes, although they are smaller. Their main function is to produce myelin to be provided to the nearby axons (Washington & Leaver 2009). Myelin is only found around the axon of neurons, and it is essencial for the adequate functioning of the CNS.

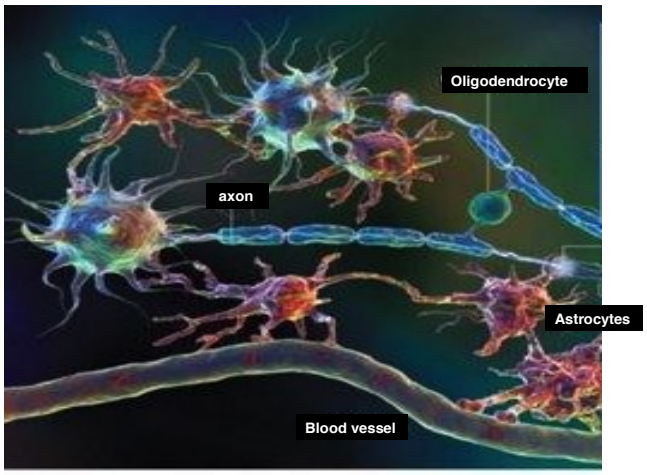

Figure 1.2. *Some of the principal components of the CNS: neurons (with its axons), astrocytes and oligodendrocytes, and blood vessels.*

Both astrocytes and oligodendrocytes may develop into brain tumors as direct consequence of some factors including environmental exposures, lifestyle, medical conditions, and genetic factors. Moreover, these tumors may derive from cerebral metastases of mammalian and lung cancers (Hall & Giaccia 2006, Nguyen & Massagué 2007).

Gliomas are brain tumors that develop from normal astrocytes cells. They are one of the most common primary brain tumors with an incidence of about 5 to 10 new cases per 100,000 inhabitants every year (Legler *et al.* 1999). Gliomas are usually classified according to its growth rate and malignancy following a widely-used grading system (Washington & Leaver 2009): I- or II-grade refer to the lowest grades of gliomas, which constitute the 25% of all gliomas, whereas the III- and IV-grade are considered as high-grade tumors, with an incidence of 75%.

Both glioblastoma (GB) and glioblastoma multiforme (GBM) are considered the most lethal brain tumors. This is due to its high infiltrative growth pattern, which leads to an overall survival of about one year regardless of the treatment (Behin *et al.* 2003). Another feature of GBM is the neovascularization and the subsequent alteration of the BBB permeability in the tumoral area of the brain (Adam *et al.* 2005*a*, Adam *et al.* 2005*b*, Barth *et al.* 2005). The BBB is a functional barrier which ensures the protection of the brain from all potentially toxic substances. The BBB permeability not only can be altered by the infiltrative pattern of high-grade gliomas, but also for instance, if high doses are delivered in radiotherapy treatments. This might be used to selectively deliver some chemotherapy drugs to specific areas of the brain.

Despite intensive research and development, the treatment of high-grade gliomas still remains palliative. The gold standard treatment based on temozolomide administered previously to radiotherapy achieves only a modest (around 14 months) increase in survival (Stupp *et al.* 2005). In part, this is due to the fact that radiotherapy treatments are limited due to the dose tolerance of surrounding healthy tissues, which is lower than dose required for the ablation of those brain tumors. Thus, systematic investigations are required to develop new radical and curative radiation treatments, such as those carried out in synchrotron's biomedical beamlines during last decades. They arise as promising techniques in the quest of ways to widen the therapeutic window of high-grade gliomas.

1.2 Radiotherapy (RT)

RT is the use of ionizing radiation to treat tumors, as well as benign lesions like artero-venous malformations. It is one of the most important methods for cancer treatment. In fact, at least 70% of patients will receive RT at some point in the course of their illness (IAEA-TRS-461 2008).

Throughout next sections, the interactions between ionizing radiation and matter, which lead to the deposition of dose within tissues will be described.

1.2.1 Interactions of photons with matter

Nowadays, RT is performed with different types of beams (protons, electrons, photons, etc.). The beam type determines how the energy is deposited in the different biological tissues. Since in this work only X-rays were employed, this section will be enterely devoted to the interaction of photons with matter.

X-rays are a kind of electromagnetic radiation with energies ranging between 0.1 and 10^3 keV approximately. See Figure 1.3.

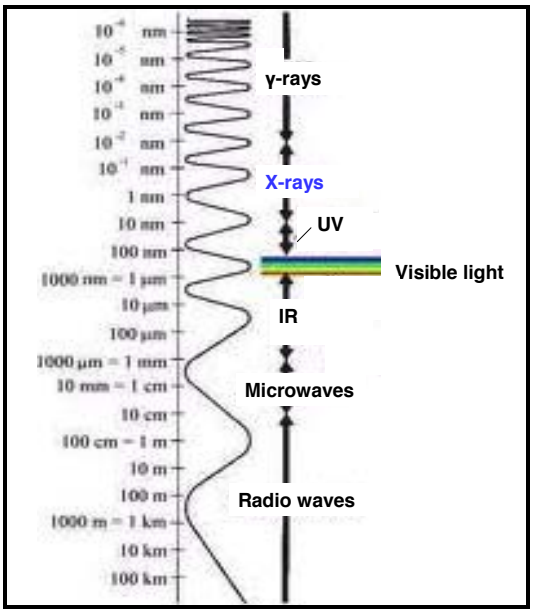

Figure 1.3. *Spectrum of electromagnetic radiations. X-rays are denoted in blue, set immediately above of UV (ultraviolet radiation), visible light and IR (infrared radiation).*

Mainly two processes play a role after interaction between matter and X-rays at the energies used in therapy: i) photoelectric absorption, and ii) Compton scattering effect.

- Photoelectric absorption:

This process is the absorption of an incoming photon after interaction with an atom (see Figure 1.4). As a result, one electron (called photoelectron) is ejected from the corresponding edge, with a kinetic energy (T) given by:

$$T = E - E_B \qquad (eq.\ 1)$$

where, E is the energy of incident photon, and E_B is the binding energy of the electron. The absorption edge is more pronounced at the K-shell, where electrons are strongly attracted by the nucleus, and therefore a higher E_B is required to remove the electron.

Figure 1.4. *Photoelectric process, with one photoelectron ejected as a result.*

The probability of a photoelectric interaction, i.e., the cross-section (σ_{ph}), is given by:

$$\sigma_{ph} \ \alpha \ (\rho\, Z^4 / E^3) \qquad (eq.\ 2)$$

where ρ is the density and Z the atomic number of the material, while E corresponds to the incident energy (Mayles *et al.* 2007). Equation 2 explains why cranial bones (high effective Z) offer higher beam attenuation (or absorption) in comparison with brain tissue at the same beam energy.

After ionization, the excited atom can de-excitate by two main pathways: via a radiative process (fluorescence emission, Figure 1.5-A), or through a non-radiative process (emitting an Auger electron, Figure 1.5-B).

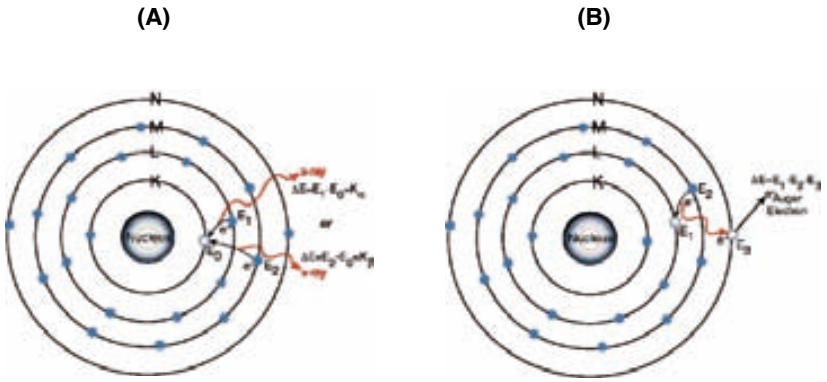

Figure 1.5. *Relaxation processes after atom ionization: A) by a radiative process emitting fluorescence rays, or B) by a non-radiative process in which the particles emitted correspond to Auger electrons.*

The relative probability of fluorescence X-ray emission is measured by the fluorescence yield (ω). The fluorescence yield is the ratio of the number of K X-ray photons emitted to the number K-shell vacancies created. For large values of Z, X-ray fluorescence emission is dominant. Thus, (1- ω) expresses the probability for Auger electron emission. Oppositely, for atoms with $Z < 80$ Auger effect is predominant because of the lower attraction between nuclear protons and electrons (Mayles *et al.* 2007, Nikjoo *et al.* 2008).

In particular, in the case of Auger electron emission process, a second inner shell vacancy is created by the initial decay event. The excess of energy is released by a series of subsequent transitions that can be assumed to occur like a cascade. In general, all atoms except H and He are able to emit Auger electrons.

- Compton scattering effect:

Compton scattering is the interaction between an incident X-ray photon and an electron belonging to an outern shell of the atom. In particular, a fraction of the incident X-ray energy is transferred to this electron which is ejected from the atom, whereas the incident photon is deflected with a lower energy (see Figure 1.6). This photon with reduced energy might origin new further interactions. It is an incoherent or inelastic scattering.

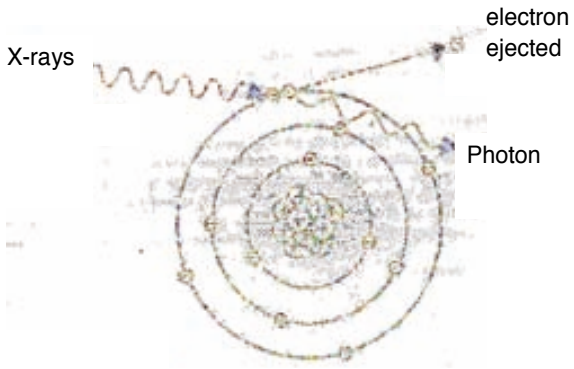

Figure 1.6. *Compton scattering effect. The incoming photon is deflected after transferring part of its energy to an electron that will be finally ejected.*

The cross-section ($d\sigma_{Co}/d\Omega$) for Compton scattering process is given by Klein-Nishina formula (Mayles *et al.* 2007),

$$\frac{d\sigma_{Co}^{KN}}{d\Omega} = \frac{r_e^2}{2}\left(\frac{E_C}{E}\right)^2\left(\frac{E_C}{E} + \frac{E}{E_C} - \sin^2\theta\right) \qquad \textit{(eq. 3)}$$

where, r_e is the electron orbital, E_C is the energy of the scattered photon, E corresponds to the initial energy of photons, and θ is the photon angular deflection.

This process is independent of atomic number (Z), but it is proportional to the tissue electron density, and it is only weakly dependent on the energy of the incident X-ray. Thus, after a Compton interaction with the i-th shell, the consequent electron is ejected from the atom with a kinetic energy $E_e = E - E_C - U_i > 0$, where U_i is the ionization energy of the considered shell.

ºTherefore, X-rays are capable of ionizing materials either via photoelectric or Compton effect, leading to chemical and biological changes in tissues. As it passes through matter, the X-ray beam undergoes a gradual reduction in the number of photons as a consequence of the different interactions suffered with matter. This process is named **attenuation** and it is determined by material thickness, density, and effective atomic number (Mayles *et al.* 2007):

$$I(x) = I(0)\, e^{-\mu x} \qquad (eq.\ 4)$$

where $I(x)$ is the beam intensity transmitted through a thickness x of material, $I(0)$ is the intensity recorded without any absorber, and μ is the linear attenuation coefficient of the absorber at the photon energy of interest. The linear attenuation coefficient is found to increase linearly with absorber density and usually is expressed in cm^{-1}. At the energies used in therapy (keV) this coefficient arises as the result of the contribution of two factors, as it is depicted hereafter (Mayles *et al.* 2007):

$$\mu = (\tau + \sigma)\, \rho \qquad (eq.\ 5)$$

where τ is the contribution of the photoelectric effect, σ is the part due to Compton scattering, and ρ corresponds to the absorber density. Thus, μ involves both absorption ($\tau = Z^3/E^3$) and scattering ($\sigma = 1/E\ Z$) processes. Figure 1.7 depicts the most feasible interaction (photoelectric effect, Compton scattering and pair production) as a function of the photon energy E (MeV) and absorber Z.

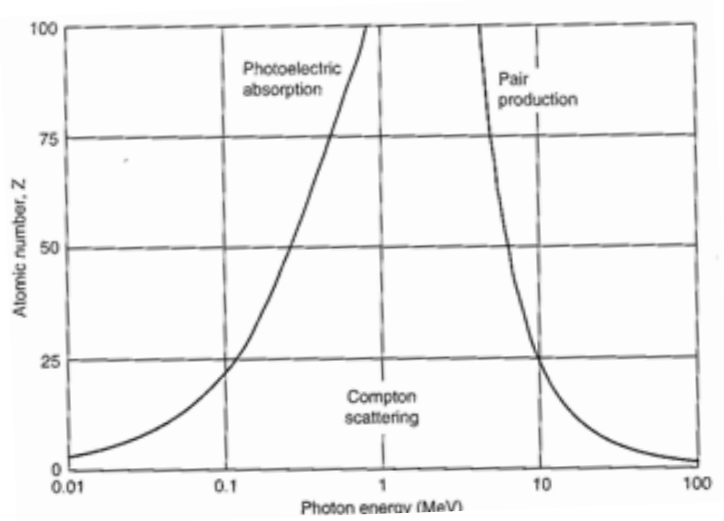

Figure 1.7. *Most probable interaction versus photon energy for absorbers of different Z. At low energies the photoelectric effect*

predominates, whilst at increasing energies the Compton scattering and the pair production become more relevant.

The pair production is the process for which an electron and a positron are generated at the same time as a consequence of the interaction between matter and X-ray beams at energies above 1.02 MeV. Since RT treatments considered in this thesis use beams at keV energies, the pair-production component (κ) is zero (Mayles *et al.* 2007).

As it has just been explained, when radiation passes through matter, it deposits energy in the material concerned. This energy deposition leads to some damages in cells, such as those which will be explained in section 1.4.

The effectiveness of ionizing radiation for cancer treatments relies on localized release of large amounts of energy in tumors. This effectiveness will depend on several factors such as i) absorbed dose, ii) the dose rate, iii) LET, and iv) temporal beam fractionation.

i) A magnitude playing a major role in RT is named **dose**. It is the mean energy deposited on matter by ionizing radiation. Dose is measured in Gray (Gy), being 1 Gy equal to 1 J/kg. Before the *Gy*, the *rad* was the unit of absorbed dose, being 100 rad equal to 1 Gy.

ii) The **dose rate** is the time required to deposit a certain dose on the target. The dose-rate effect is crucial in RT since it is correlated to the sublethal repair damage during a long γ- or X-rays radiation exposure. A dose–rate effect has been observed for reproductive failure, division delay, chromosome aberrations and cell survival.

At low dose rate each cell that suffers a particle interaction will experience a larger delay before a second particle interact again, enabling a major cell recovery during irradiation. Therefore, low dose rates are considered less efficient in producing cell damage than high dose rates, where cells cannot postpone their reparation.

iii) **Linear energy transfer (LET)** is a measure of the energy transferred to a material as an ionizing particle travels through it. LET quantifies the energy transferred to the material surrounding the particle track by means of secondary electrons with energies lower than a certain value Δ,

$$L_{\Delta} = dE_{\Delta}/dx \qquad \text{(eq. 6)}$$

For instance, photons used in conventional RT are considered as low LET radiations. Typical LET values for this sparsely ionizing radiation may range from 0.3 to 3.0 keV/μm (Washington & Leaver 2009). Nevertheless, Auger electrons arising as a secondary particles possess a high LET (10-25 keV/μm), being able to deposit their energy in the immediate vicinity (Karnas *et al.* 1999), and thus, minimizing the dose deposition in surrounding tissues.

As LET decreases, irradiation results in less cell killing per Gy. This occurs since lesions are more prone to be repaired correctly, as a consequence of a lower amount of potentially lethal damage. Since different LET radiations produce different biological responses, LET value plays a role in what is called **relative biological effectiveness (RBE)**. RBE is defined as the ratio of doses deposited by a reference radiation source and other source to produce the same biological effect. The reference beam quality is usually chosen either 250-kV X-ray irradiator or from ^{60}Co-bomb.

Sparsely ionizing low-LET radiation is expected to be less efficient (lower RBE values) because a larger number of particles should pass through the cell to kill it. Oppositely, densely ionizing high-LET (higher values of RBE) deposits the enough energy per cell to inactivate it. Charged particles are considered as high-LET radiation (Mayles *et al.* 2007). In fact, nowadays there are other RT methods, called **hadrontherapy**, based on external irradiations with H^+, alpha particles, C^+, Ne, etc. (Brahme 2004), or with neutrons that cause the activation of ^{11}B compounds previously injected in tumor cells (Boron Neutron Capture Therapy, BNCT), which emit charged particles of high LET locally in the target (Barth *et al.* 2005).

iv) Modern radiation therapy treatments are given in daily fractions over an extended period until 6-8 weeks. This radiation scheme is known as **temporal fractionation** and it allows to replace a single and high-dose radiation treatment, by several low-dose fractions of 1.5 or 2 Gy with the aim to allow normal tissue enough time to recover. As a consequence, the surrounding healthy tissue remains within the tolerance doses (Washington & Leaver 2009).

Despite RT treatments with particles have improved the dose deposition locally in the tumor, and the temporal dose fractionation allows to keep the healthy tissue within the dose tolerances, new RT approaches are being explored at synchrotron sources with the aim of improving the therapeutic ratio of glioma treatments. In particular, some of the techniques developed at synchrotrons are based on spatially dose fractionation by using submillimetric fields. This radiation modality opens a new way of dose deposition, which involves different biological

responses with respect to the seamless modes. All these synchrotron-based techniques will be explained through the next section.

1.2.2 Exploring new paths in radiotherapy techniques: High dose-rate and energy radiation

Since 1990s synchrotron radiation has been used as a valuable tool for experimental RT. The distinct characteristics of this radiation (high brilliance, low divergence, etc.) (Renier *et al.* 2008) allow to explore new dose delivery methods which might improve the therapeutic ratio of high-grade gliomas. The **therapeutic ratio** (also called therapeutic index) is defined as the dose that produces toxicity in 50% of population divided by the minimum dose to reach a desired effect on a biological target. In other words, the therapeutic ratio may be understood as the tumor response for a fixed amount of damage on the healthy tissue (Hall & Giaccia 2006).

With the aim of improving the therapeutic ratio, two new avenues are being explored with synchrotron radiation:

- Novel combinations of high-Z atoms loading tumor cells and irradiations, and
- New modes of dose deposition based on the spatial fractionation of the dose.

Through this section, the fundamentals of synchrotron radiation (SR) will be described. A special emphasis will be done on the third-generation synchrotrons, such as the ESRF, which account with insertion devices to produce SR.

1.2.2.1 Synchrotron radiation sources

Charged particles emit electromagnetic radiation when accelerated (Jackson 1998). In particular, SR is generated when a charged particle moving at a relativistic speed follows a curved trajectory.

SR can occur as undesired energy loss or produced on purpose for certain applications. The widespread usefulness of SR mainly in physics, material science and biology has led to the build of special facilities devoted to SR generation, which are named synchrotrons. These facilities accelerate charged particles (typically, electrons) in a circular orbit by means of electromagnetic fields. Electrons are generated in termoionic cathodes (typically made of tungsten), and they are pulled out by a strong electric field at the end of the gun.

A synchrotron facility is usually composed of the following parts, which are depicted in Figures 1.8 - 1.10:

1) Linear accelerator (linac):

Electrons are ejected from a termoionic cathode and they are subsequently accelerated by radiofrequency waves through the linac. Commonly, linacs have a lenght of around 10 m.

Figure 1.8. *Picture of the linac of the ESRF (Grenoble, France).*

2) Booster or pre-accelerator:

Electrons coming from the linac enter the booster in order to be accelerated up to the maximum operational energy (6 GeV at the ESRF or 3 GeV at ALBA (*Cerdanyola del Vallès,* Barcelona)).

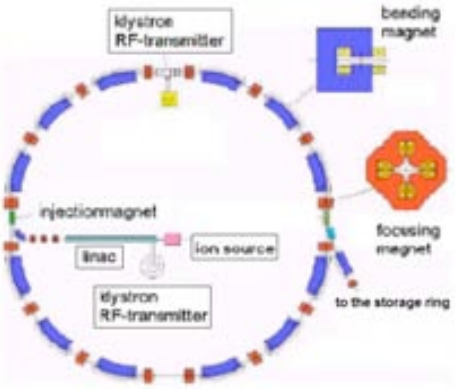

Figure 1.9. *Scheme of the booster, where bending, quandrupole and sextupole magnets can be found.*

3) Storage ring:

Storage ring comprises both straight and curved sections under ultra-high vacuum (< 10^{-8} mbar). Dipole magnets are located in the curve sections to bend the electrons trajectory in order to maintain them in a closed orbit and/or produce SR with a continuous spectrum. The electron beam is steered and focused by quadrupoles and sextupoles in order to keep the beam within a defined quasi-circular orbit for many hours.

Several cavities with a radiofrequency accelerating field are distributed along the storage ring in order to compensate the energy loss of the electrons.

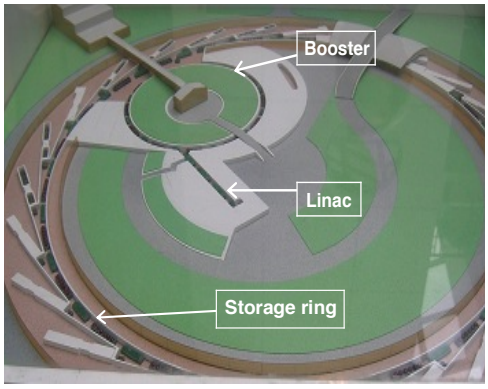

Figure 1.10. *ESRF model with the linac, booster and storage ring. Note that the beamlines appear tangecially to the storage ring.*

In third-generation synchrotron sources, specialized devices called insertion devices (ID) are located in the straight sections between bending magnets. ID can be wigglers and undulators, which both consist of an array of magnets which are used to generate a spatially periodic magnetic field along the electron beam path (see Figure 1.11).

The features of the photons emitted clearly differ in intensity from bending magnets to ID, as it is depicted in Figure 1.11. Note that the most intensity beam is achieved when electrons pass through an undulator.

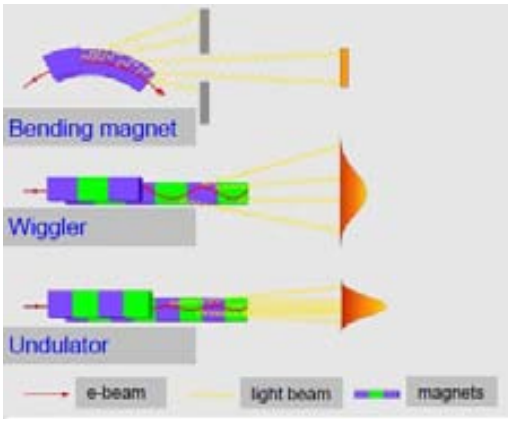

Figure 1.11. *Physical characteristics of photons in function of the source: bending magnet, wiggler or undulator.*

Thanks to ID, synchrotron radiation presents the following interesting key features:

- Very high brilliance and flux**:** both considered as figures of merit for a light source. Concretely, brilliance is defined as number of photons per second, per unit area and per unit solid angle within the 0.1% of the spectral range, or in easier way, the density of "useful" photons per unit area and per unit solid angle (Figure 1.12).

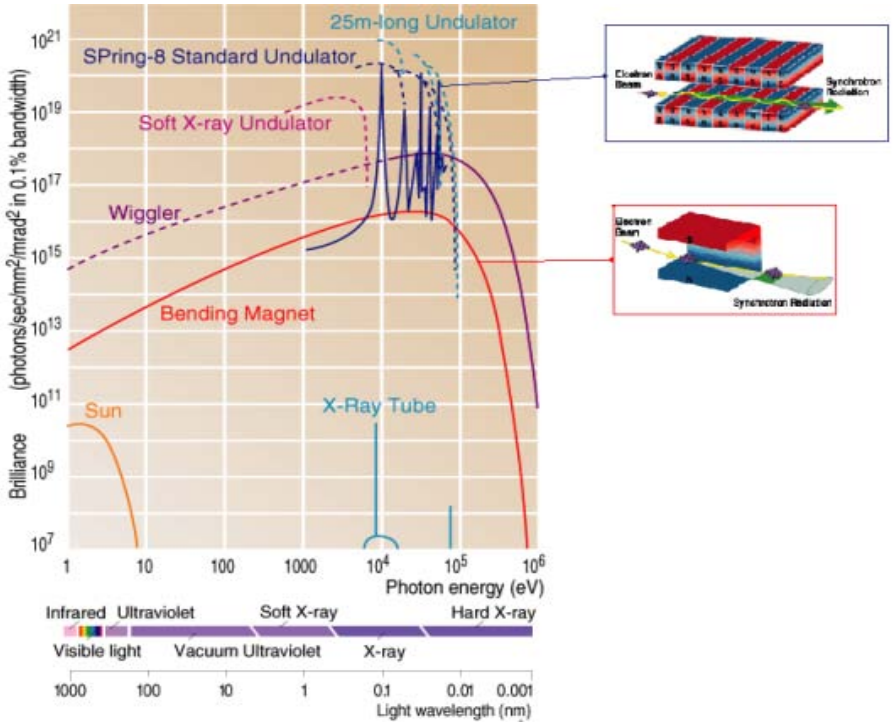

Figure 1.12. *Brilliance of the photons of Spring-8 (japanese synchrotron) according to the source of emission (www.spring8.or.jp). A wiggler (upper figure) and a bending magnet (lower figure) have also been represented.*

ID, in particular undulators provide the most brilliant beams, whereas the brilliance of beams from conventional X-ray tubes are around 6 orders of magnitude lower.

On the other hand, the flux of a source is the number of photons per unit time. These both parameters are the responsible for the very high dose rates achievable at synchrotrons.

- High-collimation and low emittance (phase space area comprising 90% of particles divided by π). Both features lead to small angular beam divergence (typically few mrad), even at several meters from the source.

- High temporal and lateral coherence, as a consequence of the small size of the source and its large distance from the radiation target. A light source is generally considered to be coherent when an experiment made with this source shows interference fringes (Baruchel *et al.* 2000, Langeler 2001).

- High polarization: which can be tunabled being linear, circular or elliptical. It allows, for instance, to make synchrotron techniques more sensitive to molecular rotations.

- A wide and continuous energy spectrum: which ranges from infrared (IR) to hard X-rays, as it is shown in Figure 1.12.

Synchrotron beams possess thus relevant characteristics (mainly high flux, low divergence and very high dose rates) which allow to develop new radiotherapy techniques based on distinct dose delivery methods. Some of these new avenues are being developed at the biomedical beamline at the ESRF, called ID17, which is described hereafter.

1.2.2.2 ID17 Biomedical Beamline

ID17 is one of the two longest beamlines at the ESRF in which three main research areas are developed: i) medical imaging, ii) radiation biology, and iii) radiation therapy (Suortti & Thomlinson 2003).

As it is depicted in Figure 1.13, this beamline possesses two different experimental hutches with their corresponding optical hutches. The first one is placed at 40 m from the wiggler and it is devoted to spatially fractionated RT techniques, such as MRT and MBRT (see section 1.2.2.4). These irradiations are featured by a white beam coming from a wiggler of 15-cm period, after passing through some filters. The second experimental hutch is located at about 150 m from the source (a wiggler with a period of 12.5 cm). This is used for monochromatic broad beam irradiations in RT (SSRT and PAT, both described in section 1.2.2.3) and in medical imaging experiments.

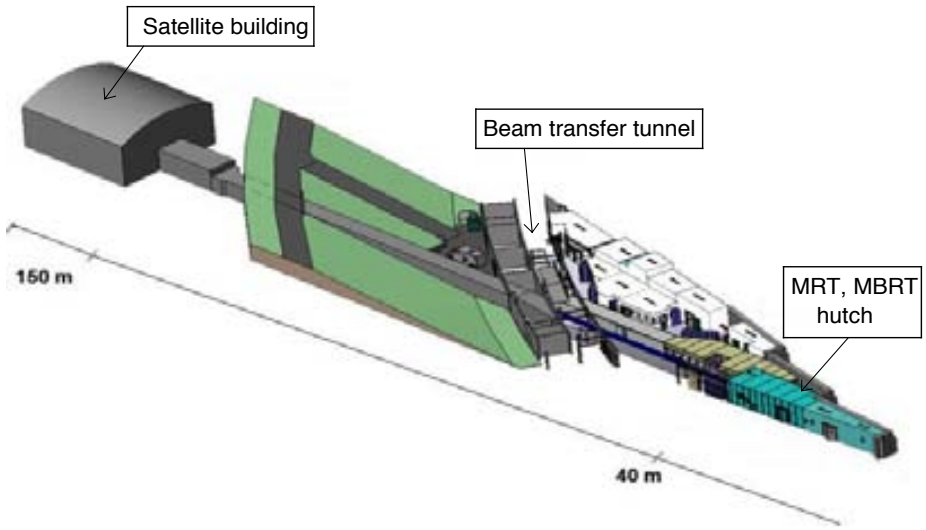

Figure 1.13 *ID17 layout (www.esrf.fr), where the 2 experimental hutches are differentiated. MRT, MBRT and white BB exposures are performed at 40 m from the source, whereas monochromatic irradiations are performed in the satellite building, at 150 m from the wiggler.*

Monochromatic beams are obtained from a fixed-exit monochromator set just before the experimental hutch of the satellite building (Figure 1.13). Further technical details on the beamline can be found in Renier *et al.* 2008. In fact, this larger distance from the wiggler source enables to obtain a better spatial resolution either for imaging or RT techniques, due to the higher efficiency of monochromator to select one wavelenght.

Two new avenues are being developed in this frame at the ID17 biomedical beamline at the ESRF, with the aim of improving the therapeutic ratio:

- Novel combinations of high-Z atoms loading tumor cells and irradiations, and
- New modes of dose deposition based on the spatial fractionation of the dose.

Both synchrotron RT schemes are further described through the next section.

1.2.2.3 RT combined with high-Z elements in the tumor: SSRT and PAT

When tumor cells are loaded with enough concentration of a compound containing high-Z atoms and irradiated with beam energies of several dozens of keV, an enhancement of the photoelectric effect is obtained, as it can be deduced from equation 1. Since the products of those interactions have a short range, the dose is deposited locally in the tumor.

Because of high-intensity and tunability of monochromatic X-rays with a high energy resolution, synchrotron facilities arise as ideal sources for the development of this kind of radiotherapeutic techniques (Boudou *et al.* 2005).

Two different approaches were developed in parallel at the ESRF biomedical beamline: i) Stereotactic Synchrotron Radiation Therapy (SSRT), and ii) Photon Activation Therapy (PAT).

- SSRT:

This technique is based on the administration of agents routinely used as imaging contrast, such as iodine (I), prior irradiations. The irradiation is then performed in stereotactic conditions from several angular ports (Prezado *et al.* 2009*a*).

The contrast agents are injected to the pacient, where they accumulated in the tumor interstitium due to the increased permeability of the BBB as a consequence of tumor growth. Concentrations from 1 to 5 mg/ml of iodine are typically reached by intravenous (i.v.) infusions (Mesa *et al.*1999). For a therapeutic treatment, an optimized administration protocol should be used for increasing the iodine tumor uptake. For instance, an increase of iodinated compounds concentration in the tumor is feasible when they are administered adjuvanted by a BBB opener such as mannitol (Adam *et al.* 2006).

The concept was first proposed by Fairchild & Bond (1984), and by Santos-Mello *et al.* (1983) after the observation of additional blood damages in pediatric diagnostic radiology when using contrast agents (Callisen *et al.* 1979). After having modified a computer tomography scanner into a therapy machine (Iwamoto *et al.* 1990), the preclinical studies (Iwamoto *et al.* 1993, Norman *et al.* 1997) ended up to the phase I of clinical trials on brain metastasis (Rose *et al.* 1999). Monte Carlo simulations have shown that the use of intense monochromatic X-rays tuned at the optimal energy could significantly improve the dose distributions (Boudou *et al.* 2005, Edouard *et al.* 2010). The biological equivalent doses received by the organs at risk were determined to remain within tolerances (Prezado *et al.* 2009*a*). Preclinical studies were carried out at the ESRF with rats bearing high-grade F98 gliomas. Rats treated with iodinated contrast agent before monochromatic irradiations at 50 keV X-rays showed a significant improved survival (until of 110%) when compared to rats irradiated without high-Z element (Adam *et al.* 2003, 2006).

Those promising results served as base for planning the clinical trials foreseen in the near future at the ESRF. Irradiation protocols for clinical trials are based on monochromatic irradiations with a beam energy of 80 keV (Prezado *et al.* 2009*a*). The choice of this energy relies on a balance between a significant dose enhancement in the tumor while keeping the skull bone under tolerances (Boudou *et al.* 2005, Prezado *et al.* 2009*a*, Edouard *et al.* 2010). Dose delivery schemes based on beams in tumor from different incidence directions (estereotactic mode) permits also to control up to a certain limit the superficial dose in skin and bone.

Similar dose enhancement factors (DEF) were obtained for other two contrast agents, gadolinium (Gd) and gold (Au), at the same concentration than I (10 mg/ml) when irradiated at energies from 50 to 90 keV (Edouard *et al.* 2010). Gd, like I remains extracellularly, whereas Au can be incorporated into tumor cells when administered in form of nanoparticles (NPs), as it will be explained through the section 1.3.3.

However, a larger number of *in vitro* experiments are required in order to investigate the toxicity of Gd and Au at those high concentrations, as well as the optimal energy irradiation for both high-Z elements respectively.

- PAT:

PAT is based on the administration of drugs containing heavy elements which are able to penetrate up to the nucleus of tumor cells. Subsequent irradiations at energies at or just above the K-edge of those elements lead to the emission of electrons of low mean free path, such as Auger electrons that are able to release large amounts of energy in its immediate surrounding. This might increase the number of DNA double-strand breaks (DSBs) (Corde *et al.* 2003, Biston *et al.* 2004).

Pt-containing drugs (cisplatin, carboplatin, oxaliplatin) seem to be a good option for PAT since they bind DNA by forming DNA adducts. However, because of the high intrinsic toxicity of those chemotherapy compounds only small concentrations (nM to few μM) can be brought to the DNA. Therefore, it was not clear whether a dose enhancement can really occur under those circumstances.

Experiments based on the comparison of cell damage provided between synchrotron irradiation at 78.8 keV and an exposure of a clinical 6 MV source showed that high-energy photons caused a low but significant amount of both DNA single- and double-strand breaks (Biston *et al.* 2009). Moreover, little differences on the percentage of surviving rats were found between both chemo-radiotherapeutic treatments (Biston *et al.* 2009, Rousseau *et al.* 2010), which seems to indicate that none dose enhancement was playing a role. Monte Carlo simulations reported in Appendice 1 were coherent with those experimental results, since they proved that no dose enhancement occurred neither when cells loaded with cisplatin 7 μM are irradiated at 79 keV in *in vitro* experimental-like conditions.

Despite that, an increase of life span from 300% to 700% approximately was observed in several *in vivo* experiments carried out at the ESRF (Biston *et al.* 2004, 2009). Thus, cisPt probably acts like a radiosensitizer enhancing a synergic effect between Pt-based drugs and irradiation, and therefore the effectiveness of those treatments.

For instance, inhibition of the non-homogeneous end joining (NHEJ) repair pathway (see section 1.4.1) arises as a consequence of Pt-DNA adducts (Yuan *et al.* 2010). Thus, a larger proportion of DNA DSBs might be achieved as a consequence of unrepaired breaks when cells pretreated with platinated compounds are exposed to SR tuned at around 78.4 keV, corresponding to the Pt (Z = 78) K-edge energy (Corde *et al.* 2003, Biston *et al.* 2004).

1.2.2.4 RT based on the spatial fractionation of the dose: MRT and MBRT

Both Microbeam Radiation Therapy (MRT) and Minibeam Radiation Therapy (MBRT) combine the use of very small field sizes and a spatial fractionation of the dose. They explore the limits of what is called dose-volume effect: the smaller the irradiation field, the higher the healthy tissues tolerances (Zeman *et al.* 1959, Curtis 1967, Lawrence *et al.* 2010). It might allow to deposit higher and potentially curative doses in the tumor thanks to increased tissue tolerances.

The gain in tissue tolerances observed migh be explained by the stem cell depletion hypothesis, which states that for each organ there is a critical volume that can be repopulated by a single survival stem cell which can migrate from the surrounding undamaged tissue to the radiation-damaged one to repare it (Yaes & Kalend 1988).

The spatial fractionation of the dose allows to gain in surface/volume for tissue recovery, and it results in dose profiles consisting of a pattern or peaks and valleys. High doses are deposited along the beam path (peaks), whereas lower doses are delivered within the space between two peaks (valleys). Indeed, the dose in the valley results from scattered particles originated in the beam path.

The peak-to-valley dose ratio (PVDR) arises as an important dosimetric magnitude either in MRT or MBRT. It depends on the tissue composition, as well as on the irradiation features. The PVDR must be high, i.e., valley doses set below the tolerance dose in order to assure the sparing of healthy tissue. Oppositely, low PVDR values are requested in tumor to cause a high density of lethal lesions (Dilmanian *et al.* 2002).

The lateral distance with a dose fall-off ranging from 80% to 20% of maximum dose is named penumbra. It depends on the energy, on the peak and valleys widths, as well as on the distance between both regions (Prezado *et al.* 2009*b*). Generally, it is well-assumed that penumbra is of 8-9 μm for MRT, and 40 μm for MBRT, although both values can vary in function of the features of each radiation mode and on depth. These smaller penumbras in comparison with several mm in conventional radiosurgery make MRT and MBRT perfect candidates for the treatment of tumors close to an organ of risk.

At the ESRF, the energy spectrum for both RT techniques ranges from 50 to 600 keV (Martinez-Rovira *et al.* 2010), with a mean energy set around 100 keV. This range of energies makes feasible to further improve their outcome by loading the tumor with a high-Z element

prior irradiations (Prezado *et al.* 2009*c*, Martinez-Rovira & Prezado 2011). Moreover, high doses delivered by MRT and MBRT have been reported to produce a temporary disruption of the BBB which can be useful for selective delivery of chemotherapy agents into tumors (Serduc *et al*. 2006).

- MRT:

MRT was initially developed at Brookhaven National Laboratory (BNL) at National Synchrotron Light Source in New York (United States) in early 1990s (Slatkin *et al.* 1992). Clinical trials are currently in preparation at the ESRF.

In MRT, a multislit collimator fractionates the initial broad field into several micrometric beams (Bräuer-Krisch *et al.* 2009) whose size varies from 25 to 100 μm, and the interbeam separation ranges from 500 to 700 μm (Figure 1.14).

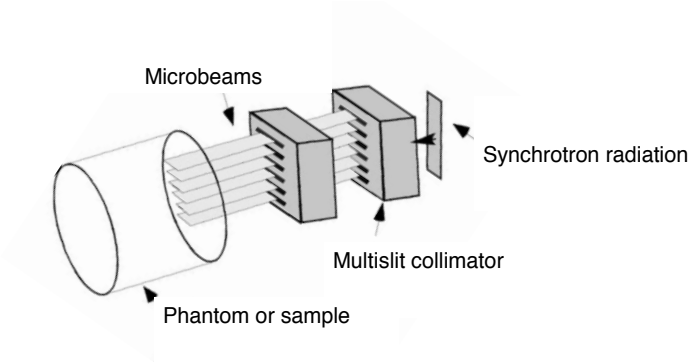

Figure 1.14. *Microbeams are generated by using a multislit collimator, which splits the initial synchrotron broad beam into several submillimeter beams.*

Already the first experiments showed the healthy tissue sparing capability of MRT (Slatkin *et al.* 1995, Laissue *et al.* 1998). Despite the biological basis of this effect has not been yet completely understood, later investigations seem to point at the biological repair of the microscopic lesions by the minimally irradiated contiguous cells (Laissue *et al.* 1998, Dilmanian *et al.* 2001, 2007, Regnard *et al*. 2008).

Undamaged undifferentiated glial cells in healthy tissues would migrate from the valley to peak regions several days after irradiations as it is depicted in Figure 1.15 (Dilmanian *et al.* 2007).

Once there, those cells could proliferate and differenciate leading to a complete tissue recovery three months later (Dilmanian *et al.* 2007). Migration and differentiation of the undifferentiated glial cells might be initiated by distant bystander effects from dying cells (Dilmanian *et al.* 2007).

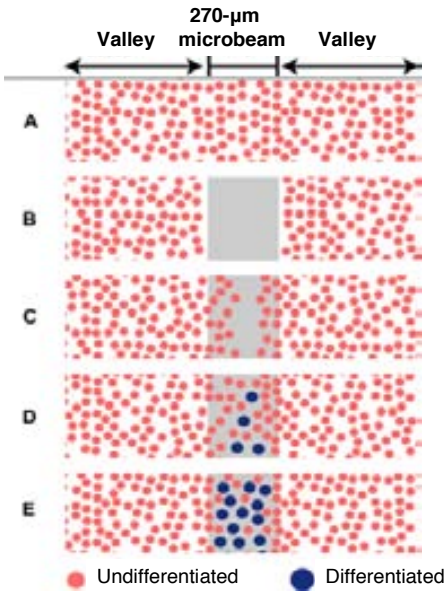

Figure 1.15. *Hypothesis proposed by Dilmanian et al. (2007) for the regeneration of the CNS healthy tissues after MRT. A) Untouched region, B) depleted region, C) migration of minimally irradiated cells, D) cell proliferation, and E) cell differentiation leading to the generation of mature glial cells.*

Previous investigations demonstrated that this spare of healthy tissues vanishes when the valley dose approaches the healthy tissue tolerance for a broad beam irradiation. Hence, the valley dose plays an important role in controlling tissue damage (Dilmanian *et al.* 2002).

A preferential tumoricidal effect at high doses of MRT has also been observed (Laissue *et al.* 1998, 1999, Dilmanian *et al.* 2002, 2003, Regnard *et al.* 2008, Serduc *et al.* 2009). This was hypothesized to be a consequence of the low recovery of immature tumoral vascular network after MRT irradiations rather than a larger tumor cell lethality (Dilmanian *et al.* 2002, Serduc *et al.* 2008).

To interlace at least two arrays of submillimeter beams to produce a quasi-homogeneous dose distribution in the tumor volume has allowed to increase the survival time of bearing-tumor animals in preclinical MRT (Dilmanian *et al.* 2003, Serduc *et al.* 2008). Despite all those outcomes of MRT, irradiations with thin microbeams present however some disadvantages:

- They can only be generated by synchrotron sources, limiting thus their widespread clinical implementation. MRT requires very high dose rates to deliver the dose in a very short lapse of time in order to avoid the beam smearring from any move, such as the cardiosynchronous pulsations (Poncelet *et al.* 1992).

- The use of higher energies, which would lead to provide low dose deposition at the entrance is restricted in an adult human head. For instance, energies > 200 keV would lead to the loss of the healthy tissue sparing of MRT as a consequence of the overdose produced by the lateral scattering (Prezado *et al.* 2009*b*).

In an attempt to overcome those difficulties, Dilmanian *et al.* (2006) have recently proposed to use thicker beams, in what is called MBRT. It is based on arrays of beams, ranging from 500 to 700 μm, with an interbeam distance of 600 μm. The features of MBRT are explained hereafter.

- MBRT:

The first *in vivo* experiment with MBRT was succesfully carried out at the BNL by Dilmanian and coworkers (Dilmanian *et al.* 2006). Beams as thick as 0.68 mm seemed to keep (part of) the sparing healthy tissue observed with microbeams (Dilmanian *et al.* 2006). In addition, MBRT overcomes the aforementioned main drawbacks of MRT (Prezado *et al.* 2009*d*).

Moreover, treatments based on interlaced minibeams, i.e., beams from different incident directions, with the aim of producing a broad beam at the tumor are technically much less challenging that with thinner microbeams (Prezado *et al.* 2011).

For all the aforementioned advantages, MBRT has been recently implemented at the ESRF ID17 biomedical beamline (Prezado *et al.* 2009*d*).

White-beam minibeams are generated by using a white-beam chopper (Figure 1.16). This device consists of ten tungsten carbide, 6-mm thick blades, assembled in a squirrel cage. Its axis of rotation is perpendicular to the incident white beam, leading to a duty cycle formed by alternance of beam in and beam off (Prezado *et al.* 2009*d*).

Figure 1.16. *Picture of the chopper used in ID17 (ESRF) to generate minibeam patterns.*

Since the thicker beams and spacings employed in MBRT may lead to different biological effects than those observed in MRT, experimental studies are warranted to elucidate the possible different tumor and normal tissue's responses to MBRT with respect to MRT and other RT methods. This Ph.D. dissertation reports part of the first histological studies with MBRT. Those first *in vitro* experiments with F98 cells, which are explained through Chapter III, pretended to investigate the effects of MBRT on cells. In addition, they were perfomed at the ESRF in order to prepare and design the subsequent *in vivo* irradiations. To elucidate the possible sparing of MBRT on healthy tissue, preclinical experiments have been carried out for the first time at the ESRF with healthy rats. Results of those experiments led to establish a tolerance dose up to 150 Gy in one direction for the whole normal rat brain irradiations (see Chapter V). Some others *in vivo* studies were carried out (Prezado *et al.* 2012) showing that interlaced MBRT geometry provided a factor three of gain in the life span of 9L gliosarcoma-bearing rats with respect to controls.

In spite of this work was focused only in white-beam MBRT, monochromatic minibeams were developed in parallel at the ESRF. A higher therapeutic ratio was obtained as well from the first preclinical trials concerning monochromatic MBRT. They were based on two monochromatic (at 80 keV) minibeams arrays interleaved in the tumor which showed a two-fold increase in survival time of F98 glioma-bearing rats when compared to untreated animals (Deman *et al.* 2011). However, further investigations concerning monochromatic MBRT are warranted.

1.2.3 Clinical orthovoltage radiation: Low dose-rate and energy radiation

Clinical orthovoltage units are characterized for their low degree of beam penetration, and thus, these equipments are useful in the treatment of superficial tumors. The low energy Gulmay D3100 generator allows to perform cellular experiments. The main parts of this type of equipment are briefly explained below:

1) The X-ray irradiator's head:

The cathode is based on a single tungsten filament that is heated by an electrical current passing through it, and emitting electrons by thermoionic emission (see Figure 1.17-A). A negative-charged cup avoids electrons from spreading out, focusing them, and ensuring that the electrons beam will move to the anode with a small cross-sectional area. Electrons are accelerated up to the anode thanks to an almost constant potential difference between the negative-potential cathode and the positive-potential anode, corresponding of around cents of kV.

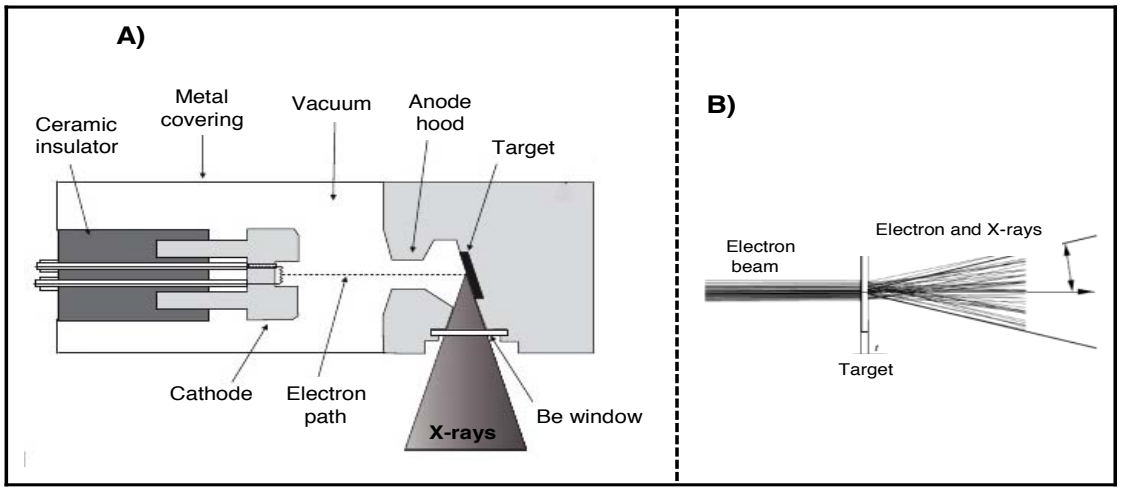

Figure 1.17. *A) Scheme of the main components of a kilovoltage irradiator's head. B) Bremsstrahlung irradiation, where photons are created from an electrons beam.*

This anode is formed by a copper hood, containing a target of gold, where incoming electrons will release large amounts of photons corresponding to the Bremsstrahlung radiation when collide it (Figure 1.17-B). Either water or oil can be use to cool the anode. The target angle should be 30º in order to: i) increase the focal spot, and ii) reduce the self-attenuation of the beam in the target. A beryllium (Be) window set on the anode (see Figure 1.17-A**)** allows the desired X-rays exit while the lowest-energy X-ray photons are removed. This window thus allows an extra filtration of the beam (Cherry & Duxbury 1998).

2) The control console:

The control panel is switched on with a key. All parameters that could affect the dose delivery and radiation quality must be displayed on the console (Figure 1.18). Paussing the treatment is possible, and in the case of power failure, an internal battery will maintain details of the treatment recorded up to that point.

Figure 1.18. *Control console placed out of the irradiator's room.*

3) Applicators:

The way to collimate the kV-photon beam is by using removable applicators such as those depicted in Figure 1.19. They also allow to define the treatment distance. Applicators can have field sizes from 10 (such as those used in experimental irradiations and showed in section 2.2.2) to 50 cm.

Figure 1.19. *Applicators of different diameter-sizes that can be used in the kV irradiators.*

The applicator consists of a rigid circular base plate which enables to attach it to the unit. Within the lead, it is found an apperture that collimates the beam to the desired field size (Cherry & Duxbury 1998).

The machine can not switch on without a filter present. Filters are usually made of aluminium (Al), copper (Cu) or zinc (Zn). The higher the atomic number (Z) of the filter, the higher the proportion of filtered photons at higher energies. In that way, the absorption edges for Zn = 29.2 keV, Cu = 9 keV and Al = 1.6 keV (Cherry & Duxbury 1998).

In order to compare the effects on F98 cells of both clinical-like and synchrotron sources, *in vitro* irradiations were performed at the *Hospital Clínic de Barcelona*. In Figure 1.20, the normalized energy spectrum for Gulmay D3100 is depicted. Note that the energy ranges approximately from 20 to 100 keV with a mean energy of around 35 keV. The dose rate of this clinical-like source was of about 0.02 Gy s^{-1}.

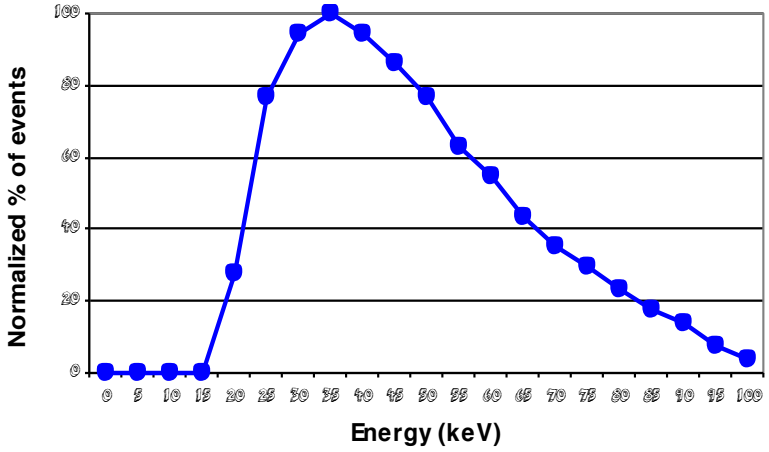

Figure 1.20. *Normalized energy spectrum of Gulmay D3100 irradiator. The mean energy is around 35 keV due to very low penetration rate of photons is needed.*

As it was explained in section 1.2.1, both the dose rate and the mean energy influence the RBE of a radiation treatment. The dose-rate effect is crucial in radiotherapy due to it is correlated to the sublethal repair damage during a long γ-or X-rays radiation exposure. Hence, by using a lower dose-rate orthovoltage source, a higher cell recover ability during and after irradiations will be expected (Hall & Giaccia 2006, Tomita *et al.* 2008).

At kilovoltage (kV) energy the interaction between incident photons and biological samples principally leads to photoelectric effect, and in a significant lower proportion to Compton scattering (see section 1.2.1). Hence, the emission of many secondary particles enhance the direct and indirect effects of radiation, i.e., ROS production, within the cells. Another way of enhancing the radiation effects would be the combination of RT with chemotherapy agents.

1.3 Chemotherapy concomitant to radiotherapy

The combination of chemo- and radiotherapy leads to a significant increase of treatment effectiveness for several tumor types like cervical cancer, head and neck cancer and others (Wang & Lippard 2005). Because of that, several unsuccessful clinical trials in which it was expected to enhance the life span of GBM patients took place by combining chemotherapy with radiation:

- Evaluation of the effectiveness of brachyterapy alone or combined with carmustine (BCNU), which is a nitrosurea drug based on DNA alkylation. In brachytherapy, the radiation source is located inside the patient in direct contact with the tumor. These sources are usually found in rods or in radiactive seeds. A randomized study showed however no benefit from the brachytherapy boost based on ^{125}I and ^{192}Ir seeds added to external-beam radiation therapy (Sneed *et al.* 1997) or combined with BCNU (Nishikawa 2010).

- Investigation of BCNU polymer wafers introduced into the resection cavity before RT. Since they are lipid soluble, they are also able to cross the BBB and to interfer with DNA synthesis in tumor cells. But the short distance of penetration of BCNU led to a marginal median survival improvement in patients compared with RT alone (Nishikawa 2010, Stupp *et al.* 2010*a*).

Those studies showed therefore no benefit from the addition of chemotherapy. The administration of temozolomide (TMZ) prior irradiations was the only combination that provided an enhancement in life span of patients with glioma (Friedman *et al.* 2000, Stupp *et al.* 2005). Nowadays it is considered the gold standard. Gold standard therapy refers to the treatment more appropiate according to the experts, and thus widely used. The gold standard therapy for GB consists of a first resection of tumor (when possible), followed by TMZ administration and RT sessions of 1.8-2 Gy each one up to reach the total dose amount of 60 Gy into the gross tumor volume (Stupp *et al.* 2005).

TMZ is an antitumor agent with broad-spectrum antitumor activity such as melanoma, leukemia, lymphoma, glioma etc. (Friedman *et al.* 2000). In clinical studies, TMZ demonstrated relatively rapid absorption within 1-2 h after administration, being able to penetrate into the CNS (Friedman *et al.* 2000, Stupp *et al.* 2010*a*).

TMZ is an oral alkylating drug (Figure 1.21), derived from the imidazotetrazine's familiy. It undergoes spontaneous reaction in the C^4 position under physiological conditions, which leads to the reactive methylating agent 5-(3-methyltriazen-1-yl)imidazole-4-carboximide (MTIC) (Friedman *et al.* 2000). This active form of TMZ produces lesions in DNA by methylation at O^6 position of guanine, as it is depicted in Figure 1.21.

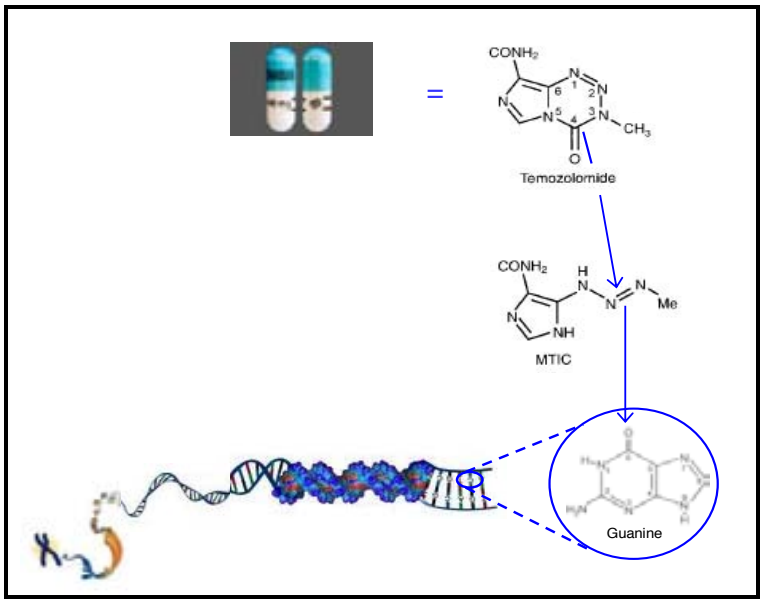

Figure 1.21. *Spontaneous reaction of oral temozolomide (TMZ) to its active form MTIC, and subsequent reaction between it and O^6 position of guanine, which is a nitrogen base of DNA.*

Since those adducts can be removed by DNA repair protein O^6-methylguanine-DNA-methyltransferase (MGMT) (Beier *et al.* 2008), administration of relatively low doses of TMZ depletes the MGMT of tumor cells. Consequently, this lack of MGMT enables high unrepaired TMZ- and/or radiation-induced damage on DNA of tumor cells. This slightly increases the survival of GB patients (Stupp *et al.* 2005, Beier *et al.* 2008). In addition, the active metabolite of TMZ is able to cross the BBB and penetrate into the CNS, even in pediatric patients (Friedman *et al.* 2010), through the cerebrospinal fluid (Stupp *et al.* 2010*a*).

In particular, 573 patients underwent randomized clinical trials of standard radiation versus radiation plus chemotherapy with TMZ. The median survival for that group receiving TMZ and radiation was of 14.6 months as opposed to 12.1 months for the group treated with radiation alone. TMZ seemed thus to work by sensitizing the tumor cells to radiation (Stupp *et al.* 2005) despite the poor increase in life span.

Absence of better alternatives led to the approval of TMZ for the treatment of glioblastomas more than a decade ago. Indeed, TMZ is considered as the first drug specifically developed for that purpose (Stupp *et al.* 2010*a*). TMZ is routinely used against malignant gliomas, either as a concomitant or an adjuvanted agent:

- **Concomitant TMZ chemotherapy** refers to the daily administration of low doses of TMZ in this case, with the aim of enhancing the tumoricidal effects of RT. For that, 75 mg of TMZ per square meter of body-surface area must be administered 7 days/week during 7 weeks, 1 to 1.5 hours before every day of radiotherapy treatment (Stupp *et al.* 2005, 2010*b*).

- On the other hand, **adjuvant chemotherapy** is based on administration of TMZ alone after concomitant treatments as a maintenance. In that way, after a 4-week break, patients receive around 6 cycles of TMZ every 28 days, 5 days/week with doses from 150 to 200 mg/m^2 (Stupp *et al.* 2005).

Despite the combination of TMZ and RT have enabled a survival benefit on patients with glioblastoma of 2.5 months compared with RT alone (Stupp *et al.* 2005), gliomas, and specially those high-grade gliomas, still have a very bad prognosis.

However, the continuous daily administration of TMZ has been demonstrated to induce important side-effects such as lymphocytopenia, responsible of later oportunistic infections, acute fatigue, cerebral hemorrhage, among others (Stupp *et al.* 2005). Some studies have also suggested that the benefit of TMZ could be restricted to patients presenting a MGMT gene promotor (Nishikawa 2010).

Investigations on the possible gain by using some other radiotherapy-enhancer compounds such as cisplatin and AuNPs were warranted.

1.3.1 Drugs based on platinated compounds: Cisplatin (cisPt)

Cis-diamminedichloroplatinum(II) or cisPt is an alkylating neutral complex of Pt(II), as it is represented in Figure 1.22. The atom of Pt is coordinated to two chloride ligands in *cis*-geometry, and two ammonia groups. Whereas the ammonia groups are strongly linked to Pt(II), the chloride ligands are labile, and hence, easily substituted by another nucleophiles such as water molecules or hydroxide ions.

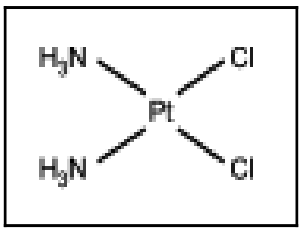

Figure 1.22. *Cisplatin (cisPt) molecule, where the two chloride ligands are in "cis"-configuration.*

CisPt enters the cell by passive diffusion, where the lower concentration of chloride ions leads to an aquated form (Figure 1.23). Those cisPt derivates present a higher reactivity with cellular compounds, being the DNA their principal target (Jamieson & Lippard 1999, Kartalou & Essigmann 2001, Yongwon & Lippard 2007).

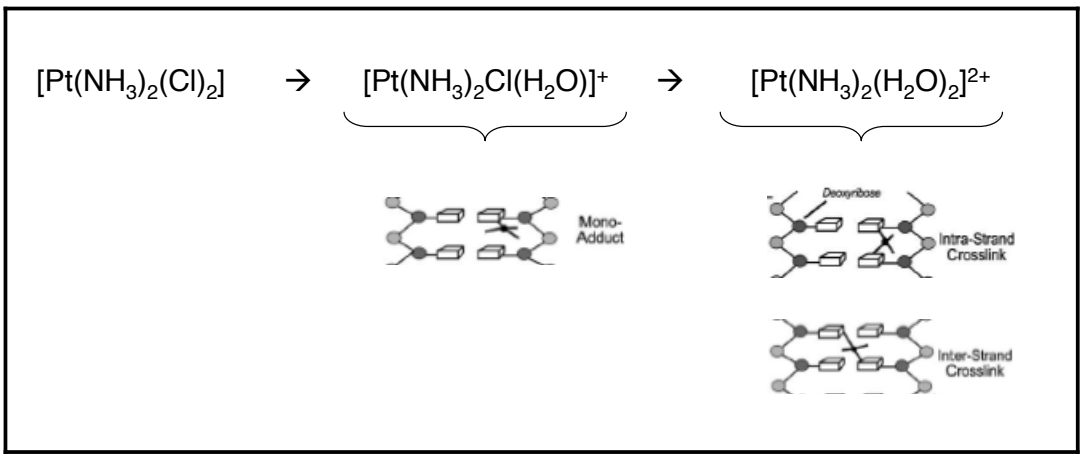

Figure 1.23. *Reaction of cisPt aquation once inside the cell to form monoadducts or the most common intra- and inter-strand crosslinked adducts between Pt and and N^7 positions of purine bases.*

The formation of cisPt-DNA crosslinks, through the covalent bonds between Pt and N^7 positions of purine bases, structurally distorts the DNA, leading to an helix instability. *In vitro* experiments provided evidence that intrastrand crosslinks are dominant with respect to the interstrand, and specially 1,2-intrastrand DNA crosslinks are the major adducts formed by cisPt (Kartalou & Essigmann 2001, Wang & Lippard 2005, Yongwon & Lippard 2007). This distortion of the structure of the DNA duplex, converts cisPt in a highly toxic agent *per* se due to its consequences on:

a) DNA replication: cisPt blocks the access to binding site of the DNA polymerase, which is the enzyme requested for DNA replication process (Jamieson & Lippard 1999). Moreover, cells treated with cisPt have been observed to progress through the S phase, being arrested in G_2 phase (see Figure 1.28 of section 1.4). Once there, cells may either remain arrested temporary at low cisPt concentrations, or until cell death occurred for high drug concentrations. Thus, they die before to enter mitosis. This prevents DNA damage from being transferred to the descendents (Jamieson & Lippard 1999, Wang & Lippard 2005).

b) Apoptotic death: which will be explained in section 1.4.2, it is known to be the main death pathway of cells after cisPt exposures as a consequence of the caspases (family of proteins) activation (Jamieson & Lippard 1999, Wang & Lippard 2005). Nevertheless, the mode of cell death is concentration-dependent. For instance, it has been detected that 8 μM of cisPt over several days can induce apoptosis, whereas 800 μM induces necrosis only after few hours (Wang & Lippard 2005).

c) Repair of CisPt-DNA adducts: the major pathway for the removal of cisPt-DNA adducts *in vivo* and *in vitro* is the nuclear excission repair (NER). It is known to generate single- and double-strand breaks for further rejoining (Jamieson & Lippard 1999, Huang *et al.* 2004, Wang & Lippard 2005). CisPt-DNA adducts also inhibit DNA-PK activity by preventing a subunit of this protein (protein Ku) and inhibiting NHEJ (Jamieson & Lippard 1999, Corde *et al.* 2003).

Up to date, cisPt has not been routinely used in treatments against gliomas. However, experiments performed at the ESRF, pointed at cisPt as a promising concomitant agent. In particular, 3 μg of cisPt administered via intracerebral injections concomitantly with 15 Gy of synchrotron radiation tuned at 78.8 keV resulted in ~ 700 % of increased life span in rats bearing F98 glioma cell line. One year after this treatment, around 34% of treated rats were still alive. It represents in fact the most protracted survival of rats bearing this type of tumor (Biston *et al.* 2004).

Before performing systematic studies, some years ago it was thought that this treatment would involve the enhancement of the photoelectric effect, principally due to the emission of Auger electrons of low mean free path. However, experiments performed later seem to conclude that the effectiveness of low concentrations of cisPt concomitantly to radiation is due to a synergic effect between them (Adam *et al.* 2008, Biston *et al.* 2009), as aforementioned in section 1.2.2.3.

Therefore, a synchrotron source would be not requested for this chemo-radiotherapy approach. According to our knowledge, the first clinical assays concerning cisPt and megavoltage clinical-like irradiations are being prepared at the United States.

In parallel, cisPt could improve the outcome of other synchrotron-based radiation techniques. To that end, *in vitro* experiments with MBRT radiation were performed at the ESRF. The aim was to further increase the therapeutic ratio of MBRT by combining it with cisPt administration (see section 5).

Despite all aforementioned benefits of cisPt, the principal limitations are its nephrotoxicity, neurotoxicity and acquired cell resistance through several exposures to cisPt over time. In an attempt to overcome these inconvenients, some new platinated compounds such as transPt, carboplatin, and oxaliplatin, which are depicted in Figure 1.24**,** have been developed. They differ on recognition and processing events, and therefore contributing to differences in cell cytotoxicity (Wang & Lippard 2005).

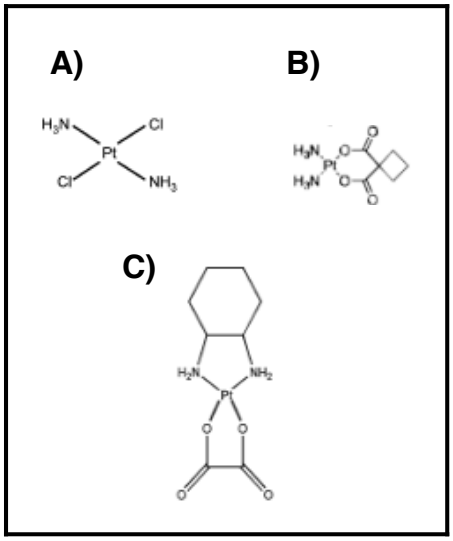

Figure 1.24. *Other platinated molecules. A) Trans-diamminedichloroplatinum(II) or transplatin (transPt), B) Carboplatin, C) Oxaliplatin, potentially less toxic.*

They have shown however a lower effectiveness in tumor control compared to cisPt (Jamieson & Lippard 1999, Kartalou & Essigmann 2001). Other strategies should be explored in order to limit the impact of drug toxicity on the healthy tissues. The first option was the administration of cisPt via direct intracerebral injections which enable its distribution in a more local way. Because of the low dispersion of cisPt in regions outern to the CNS, this cisPt delivery system is widely used in preclinical studies. Despite that, the low specificity of cisPt between healthy and tumoral glial cells would result in larger CNS toxicities.

In order to reduce the cisPt toxicity, two different alternatives were investigated:

i) <u>To decrease the concentration of cisPt by combining it with other less toxic photoactivable compound, such as metallic nanoparticles:</u>

CisPt concentration was reduced on cells by combining it with a less toxic solution of AuNP, as explained in section 6. The final concentration of high-Z atoms was equal to those used when cisPt was administered alone.

ii) <u>To associate cisPt to some biological carriers which would help increasing the drug concentration in the tumor while protecting healthy cells:</u>

In particular, cisPt was delivered in association to liposomes to increase not only the concentration of Pt inside tumor cells, but also the amount of Pt near or into the nucleus of treated cells. This was indeed demonstrated by analyzing *in vitro* the fluorescence emission of intracellular Pt measured at ID22NI (ESRF) and at the CENBG (Gradignan, Bordeaux) as it will be explained later in section 7.

In an attempt to facilitate the incorporation of such drug into the tumor cells, minimizing the dispersion of cisPt through the healthy tissues, drug delivery systems based on lipidic membranes are investigated.

1.3.2 Delivery drug systems: Liposomes

Liposomes are spherical vesicles composed of lipid bilayers, which are made basically from amphiphilic phospholipids, i.e., containing a hydrophilic (water-soluble) head and a hydrophobic (water-insoluble) tail, forming from one to several concentric membranes of around 4 nm of thickness each one (Figure 1.25). In addition, in some cases liposomes may contain other lipidic molecules like cholesterol.

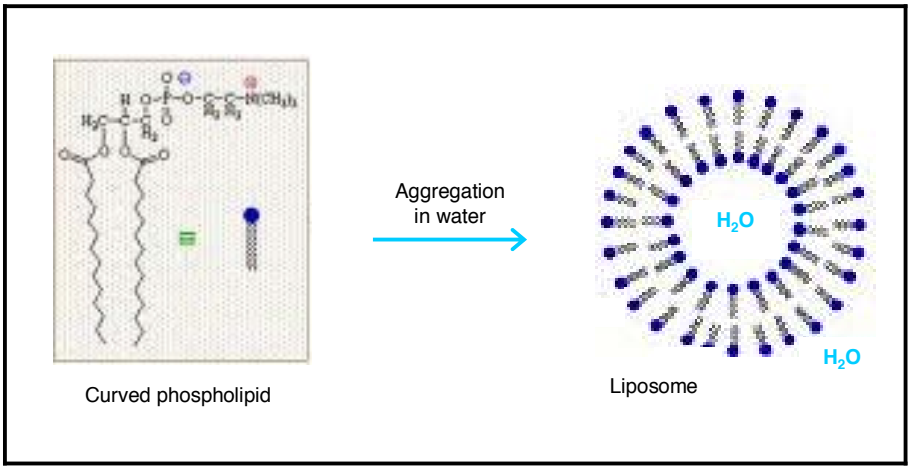

Figure 1.25. *Scheme of liposomes formation from curved phospholipids. They adopt this curved shape in water because of its hydrophobic tail, leaving a hydrophilic inner space.*

The most widely used glycerophospholipids in the liposomes formation are phosphatidylcholines (PC) or also called lecithins. The major sources of lecithins are eggs and soy beans.

Their synthesis is resumed in Figure 1.26. It is based on a first rotavaporation of solvent (chloroform). The resulting thin PC film arising on the bottom of the receipt should be rehydratated in a second step. The media used to carry out this process will determine part of the chemical properties of final liposomes. For instance, rehydratation of film by using cisPt solution will result in liposomes carrying cisPt molecules inside them and/or bound to its lipidic membranes (Duzgunes *et al.* 2003).

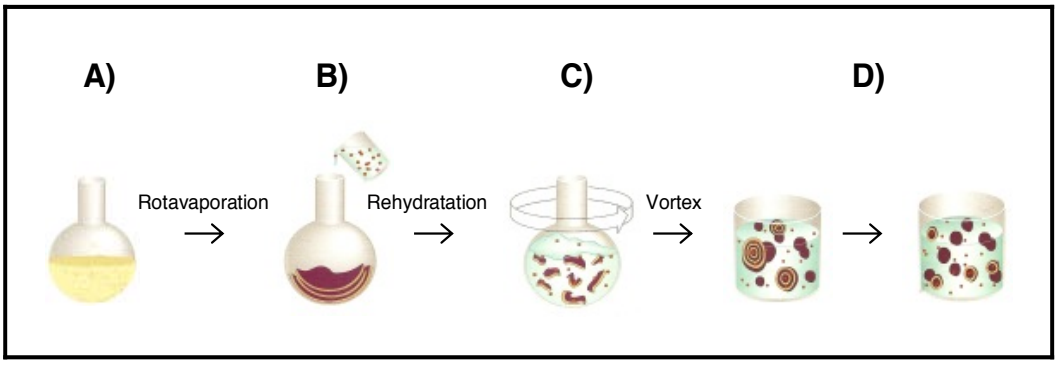

Figure 1.26. *Process of liposomes preparation. A) Rotavaporation of the chloroform, B) rehydratation of the lipidic film with cisPt solution, C) vortexing the mixture to assure the association between cisPt and vesicles. D) Different sizes and structures of liposomes can be obtained depending on the vortexing intensity.*

According to the protocol followed by its synthesis (explained in section 2.1.2), the size and structure of liposomes will be given by the vortexing intensity at the end of the process. In function of its structure and size, liposomes can be classified in the three different groups (Duzgunes *et al.* 2003) reported in Table 1.1:

Types of liposomes	*Number of lipidic bilayers*	*Diameter*
LUV (Large unilamellar vesicles)	**1**	**> 100 nm**
SUV (Small unilamellar vesicles)	**1**	**< 100 nm**
MLV (Large multilamellar vesicles)	**> 1 (concentric)**	**100-5000 nm**

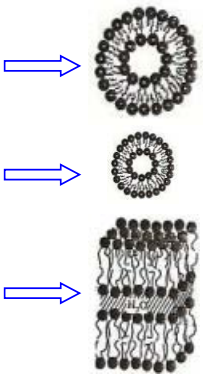

Table 1.1. *Different groups of liposomes according to its structure and size.*

All these vesicles depicted in Table 1.1 may have many biological applications. For instance, its external structure similar to a cellular membrane makes liposomes good carriers of drugs, enhancing in this way its penetration ratio into the cells. Tumor cells need to undergo endocytotic processes more often than normal cells. This may result in an increased number of interactions between tumor cells and liposomes.

In the case of gliomas treatments, liposomes should be administered by intracerebral injections. This is due to the fact that their size ranging from tens to thousands of nm is several orders of magnitude higher than the 1-nm vascular pore cut-off of BBB.

In a next step, this selectivity to interact with the adequate cells could be also achieved by recovering liposomes with specific receptors typically present on tumor cells, or driving liposomes directly to the tumor by developing new strategies such as magneto-liposomes sensitive to magnetic fields (Fortin-Ripoche *et al.* 2006).

In this Ph.D. work, liposomes were employed to transport cisPt inside the glioma cells. The concentration and distribution of Pt were investigated, as well as the comparison of effectiveness between treatments based on cisPt administered alone and cisPt associated to liposomes. Further experiments are warranted in order to better characterize the vesicles, and to improve both the targeting to the glioma cells and the encapsulation ratio.

1.3.3 New radiation-enhancer agents: Gold nanoparticles (AuNPs)

NPs for medical applications can be defined as submicron colloidal particles having at least one size dimension in the order of 100 nm or less (De Jong *et al.* 2008, Bosselmann & Williams 2012).

The use of NPs in medicine is rapidly increasing in the last years (Paciotti *et al.* 2006, Bosselmann & Williams 2012). Several clinical trials demonstrated that NPs generally improve therapy outcome when compared with standard protocols (Bosselmann & Williams 2012).

NPs are known to enter cells by endocytosis. Tumoral cells present higher rates of endocytosis due to the large energy requested by them with respect to healthy cells. Thus, this fact allows NPs to present some tumor specificity.

Among all possible metallic compounds available to develop NPs, Au has some advantages in synchroton RT. It is a high-Z element (Z = 79) and therefore it allows to enhance the photoelectric cross-section within the tumor, with very low toxicity in healthy tissues. In fact, a single intravenous injection of 1.9 nm diameter AuNPs delivering 7 mg Au/g in mice bearing EMT-6 mammary carcinoma tumors allowed one-year survival of 86% versus 20% obtained with X-rays alone (Hainfeld *et al.* 2004). Moreover, AuNPs at concentrations of 7 mg/g were assumed to be also achievable in humans (Hainfeld *et al.* 2004).

AuNPs as dose enhancers seem more promising than the earlier attempts based upon the use of other high-Z contrast media, such as I and Gd due to:

1 - Au has shown little cytotoxicity compared to I or Gd. Thus, it might be possible to increase the concentration of Au (by increasing the number of gold atoms in the particles), and consequently the dose enhancement. On the other hand, even at the same concentration of contrast agent in the tumor the photoelectric cross-section, which depends on Z^4, is higher with Au-loaded tumor.

2 - Since Au and Pt have a very similar atomic numbers (Z_{Au} = 79, Z_{Pt} = 78), photoactivation of both elements might be performed at the same energy. That fact may favor the use of lower concentrations of both chemical compounds whilst maintaining the higher effectiveness of treatments.

Intracerebral injections of AuNPs in combination with cisPt molecules would facilitate the delivery of high-Z atoms within the tumor. The reason is that after NP's administration, the surrounding molecules of sodium citrate are replaced by proteins present in bloodstream or in the medium such as serum albumin. This leads to increase the initial diameter of NPs of 7 nm (see Figure 1.27) up to the diameter similar in size to the great majority of cellular proteins, i.e., 10 - 40 nm.

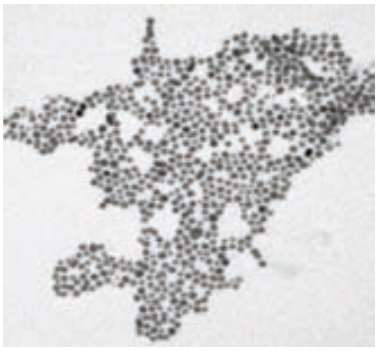

Figure 1.27. *Transmission electronic microscopy (TEM) image of those 7 nm AuNPs used in the experiments described in this thesis. Image provided by the "Institut Català de Nanotecnologia (ICN)".*

These proteins covering the colloidal AuNP not only stabilize it but also facilitate the uptake mainly by phagocytosis (De Jong *et al.* 2008, Casals *et al.* 2010), through the reticular endothelial system of tumor cells. It is indeed responsible for the removal of foreign particles from the blood, targeting easily large particles above the size of typical proteins. Thus, the NPs dimensions play a crucial role in serum albumin's surrounding region, leading to different grades of stabilized colloidal particles (Casals *et al.* 2010).

AuNPs of around 10 nm diameter present an optimal size for easiness of detection, quantification and purification. Thus, they offer a good compromise between easiness of synthesis and effectiveness in tumors, where the leaky junctions between the epithelial cells range from 100 to 600 nm depending on the tumor (Bosselmann & Williams 2012). In this way, relatively large AuNPs (~ 7 nm diameter) were investigated in an attempt to extend the protocol proposed by Biston *et al.* (2004) based on the combination of synchrotron radiation and cisPt injected intratumorally. Although first investigations of those NPs were carried out with *in vitro* glioma models, AuNPs should be administered intracerebrally in further preclinical trials in order to skip the limitations of BBB vessels diameter.

Therefore, the aim of all these aforementioned chemotherapy agents, as well as of RT techniques is to produce the maximum damage on tumor cells, whilst protecting healthy tissues. The different types of cellular damage are described in the next section.

1.4 Cellular damage resulting from chemo- and/or radiotherapeutic treatments and its assessment

When radiation interacts with a biological target, the damage might be direct or indirect.

- Direct damage is caused by photons that deposit their energy via secondary charged particles directly on cellular organules (membrane, mitochondrias, nucleus etc.) whose atoms may be ionized or excited. As a consequence of this, a chain of events leading to biological changes can be initiated (Hall & Giaccia 2006).

- Indirect damage is dominant for low LET radiation like γ- or X-rays. It involves hydrolisis reactions based on the splitting of water molecules which lead to the production of the next reactive oxygen species (ROS). They can diffuse far enough from the place where they have been originated, damaging cellular structures (Hall & Giaccia 2006):

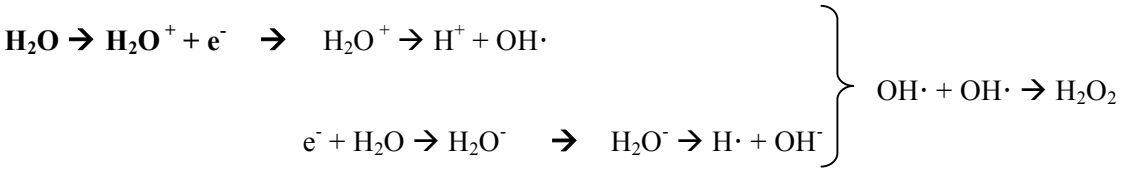

The period between the breakage of chemical bonds by these ROS and the expression of the biological effect ranges from hours to years. In particular, if cell dead is the consequence, it can be expressed in hours (Hall & Giaccia 2006). Moreover, this damage can be enhanced by administration of chemotherapeutic drugs prior irradiations.

Nuclear damage is the principal target for photons, ROS and secondary electrons, inducing mainly single-strand breaks (SSBs) and/or double-strand breaks (DSBs) on DNA. In addition to this target, the damage of other structures such plasma membrane or mitochondrias can also contribute to cell division delay, cell cycle arrest, reproductive failure and finally to death, either by apoptosis or necrosis depending on the cell line and on the radiation's features.

The amount of general damage is directly linked to the effectiveness of treatments (Hall & Giaccia 2006). A reliable assessment of damage is therefore highly important.

1.4.1 Nuclear damage: DNA double-strand breaks (DSBs)

Exposure of cells to ionizing X-rays radiation induces the formation of DNA SSBs and DSBs as a consequence of the energy deposited either by incident photons or by generation of ROS, such as those depicted above, from water molecules within cells.

In both cases, DSBs appear as a consequence of two simultaneous breaks in opposite strands of the DNA, which makes this kind of lesions to be more difficult to repair in comparison to others such as single-strand breaks (SSBs) or base damage. In fact, studies strongly suggest that neither SSBs nor base damage activate damage response signalling since their reparation is easier (Löbrich *et al.* 2010).

In few minutes after the DSBs generation, many DNA-protein kinases (PK) have been reported to phosphorylate from hundreds to thousands H2AX subfamily histones, which package and organize eukaryotic DNA into chromatin, covering large regions (foci) in the vecinity of the DSB (Rogakou *et al.* 1999). The phosphorylation takes place at the serine at the position 139 (Ser139) of H2AX, and this form has been named γH2AX. SSBs, base damages and nucleotide excisions do not seem to activate this reaction of phosphorylation (Löbrich *et al.* 2010).

Although the function of this phosphorylation still remains under investigation, the current evidences point γH2AX to be essential not only as a visual indicator of DNA repair regions but also for the co-localization of enzymes essential in the cell-cycle arrest, and changing the structure around the break facilitating the entrance of the repair molecules (Paull *et al.* 2000).

Thus, the number of DSBs caused by radiation exposures can be correlated to that γH2AX foci (Rogakou *et al.* 1999), whilst dephosphorylation might coincidence with DNA repair (Kataoka *et al.* 2006). In particular, the repair ratio has been observed to depend on i) the complexity and number of DSBs, ii) on the nature of the cell line, which will determine the activation of some repair pathways, and finally iii) on the time at which the measure is performed. The remaining foci appears to be correlated with the lethal lesions, and thus, with those cells more prone to dead by apoptosis (Roos & Kaina 2006, Marková *et al.* 2007, Belyaev 2010, Olive 2011).

In general, after radiation-induced DNA damage (with the presence of DSBs), tumor cells may activate principally two repair pathways:

i) The non-homogenous end joining (**NHEJ**) by which the two DNA breaks are simply joined.

ii) The homologous recombination (**HR**), which uses the sister homologous chromatide as a template for repair.

NHEJ occurs rapidly through any phase of the cell cycle (error-prone due to the low repair-efficiency), whilst the HR requires more time and takes place only in S and G_2 (error-free) (Löbrich *et al.* 2010, Yuan *et al.* 2010).

Whereas radiation induces directly DNA DSBs on cells, treatment with crosslinking agents such as cisPt is known to generate DNA intrastrand, and to a lesser degree interstrand crosslinks, but in any case DSBs as primary lesions (Huang *et al.* 2004, Revet *et al.* 2011). In fact, the major pathway for the removal of cisPt-DNA adducts *in vivo* and *in vitro* is nucleotide excision repair (**NER**), known to generate single- and double-strand breaks for the further rejoining (Jamieson & Lippard 1999, Huang *et al.* 2004, Wang & Lippard 2005).

CisPt-DNA adducts were also shown to inhibit DNA-PK activity by preventing a subunit of this protein (protein Ku) and inhibiting NHEJ (Jamieson & Lippard 1999, Corde *et al.* 2003).

Thus, since cells treated with cisPt develop into DSBs during DNA repair (Olive 2011), analysis of γH2AX foci at different times after this kind of treatments allows to investigate the cellular reparation in function of both, time of cisPt incubations and drug concentrations.

In that way, the assessment of DSBs on glioma rat cells at different times after treatments either of chemo- and/or radiotherapy were performed measuring the γH2AX immunofluorescence (IF) signal by using a flow cytometer. Further details can be found in section 2.3.1 of Chapter II.

The misrepaired or unrepaired damaged cells remain arrested through the cell cycle (Figure 1.28) in order to prevent damage propagation to the daughter cells.

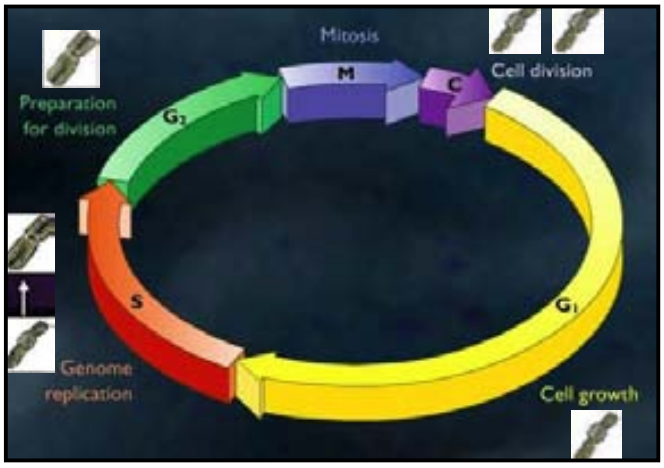

Figure 1.28. *All phases of the cell cycle: G_1, S, G_2 and mitosis (M). Note that G_1 is the longest phase of the cell cycle, whereas M is practically the shorter one.*

Finally, they will die principally by apoptosis (Marková *et al.* 2007, Yuan *et al.* 2010, Olive 2011), which is a type of cell death explained in the next section, demonstrating the effectiveness of that treatment.

1.4.2 Cell death by apoptotis or necrosis

Exposures of cells either to chemotherapeutic agents or to X-rays may lead to arise three kinds of cell populations: i) remaining alive cells, ii) cells dying by apoptosis, and finally, iii) cells undergoing a necrotic death.

Although it has been accepted that apoptosis and necrosis are two distinct modes of cell death, both culminate with the cessation of any biological activity.

- **Apoptosis** does it by an active (energy-consuming via adenosine-5'-triphosphate) pathway, where the plasma membranes and mitochondrias maintain their integrity and functions inaltered (Figure 1.29). In addition, cells dying by apoptosis i) are quietly removed by phagocytic cells with minimal interference in normal organisms activities (Zong & Thompson 2006), ii) exhibit phosphatidylserine on the cell surface which ensures the efficient removal of such cells from the medium (Zong & Thompson 2006), with a lower toxicity to the patient (Darzynkiewicz *et al.* 1997), iii) do not involve any inflammatory response (Darzynkiewicz *et al.* 1997, Zong & Thompson 2006), iv) do not result in scar formation (Darzynkiewicz *et al.* 1997).

Apoptosis appears to be regulated by some tumor supressor genes such as p53 and bcl-2, by activation of mitochondria-dependent caspases proteins pathway (Gorczyca 1999). This kind of death is a consequence, among other factors, of the production of ROS (Gorczyca 1999, Chen *et al.* 2009), the accumulation of low amounts of damage over time (Verheij & Bartelink 2000), and the activation of Ca^{2+}-dependent proteases and/or mitochondrial Ca^{2+} overload. This last fact arises as a consequence of an excess of Ca ions (0.2 - 0.4 μM) in the cytoplasm due to the inability of cells to exclude them (Zhong & Thompson 2006).

Thus, by measuring the proportion of cytosolic Ca^{2+} within those cells treated with cisPt associated or not to liposomes, it could be possible to assess which of those both treatments leads to larger ratios of apoptotic cells. With that aim, measurements of fluorescence X-rays emission were performed either at the CENBG or at the ID22 beamline at the ESRF, as it will be presented in section 7.

- **Necrosis** is a passive death mode, which causes the lysis of cells, and thus, its complete degradation (Figure 1.29) (Darzynkiewicz *et al.* 1997, Gorczyca 1999, Amirlak & Couldwell 2003). Moreover, necrosis is associated with acute cell damage, occurring generally after a gross injury such as an overdose of cytotoxic agents or X-rays exposures (Darzynkiewicz *et al.* 1997).

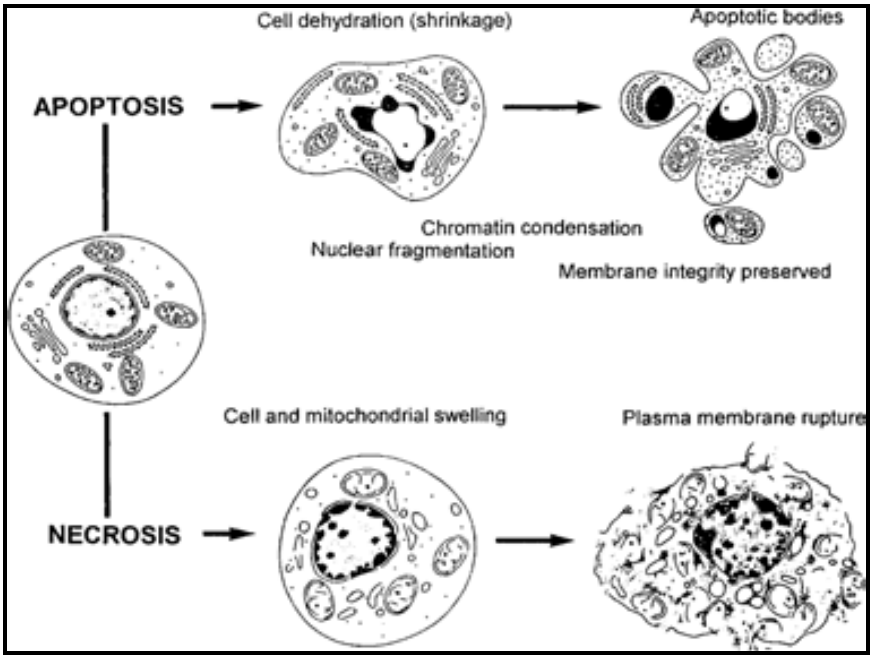

Figure 1.29. *Scheme of the two main cell death pathways (apoptosis and necrosis). In apoptosis, which is an active death, the membranes remain preserved. Necrosis is featured by the lysis of cells, and thus its complete degradation (from Darzynkiewicz et al. 1997).*

Detection of the two types of cell death was carried out by using a flow cytometry technique. In particular, apoptosis was analyzed by detection of changes in distribution of an inner plasmatic membrane phospholipid called phosphatidylserine (PS). The reason is that early in apoptosis PS undergoes translocation to the external surface of the plasmatic membrane, and by using the anticoagulant protein annexin V, which has a high affinity for the negatively charged PS, conjugated with a fluorochrome such as fluorescein isothiocyanate (FITC), it was possible to identify apoptosis in post-treated glioma cells (Gorczyca 1999, Amirlak & Couldwell 2003). In order to detect also late apoptotic and necrotic cells, FITC-conjugated annexin V was used in combination with a DNA staining such as propidium iodide (PI).

1.4.3 Metabolic activity

Since remaining living cells are responsible of tumor regrowth, its recovery ability must be analyzed after treatments. For this purpose, a complementary technique called Resazurin or QBlue cell viability test was used. It is based on the conversion of a non-fluorescent blue reagent (resazurin) into a high fluorescent pink product (resorufin), upon reduction by the remaining living cells (Figure 1.30).

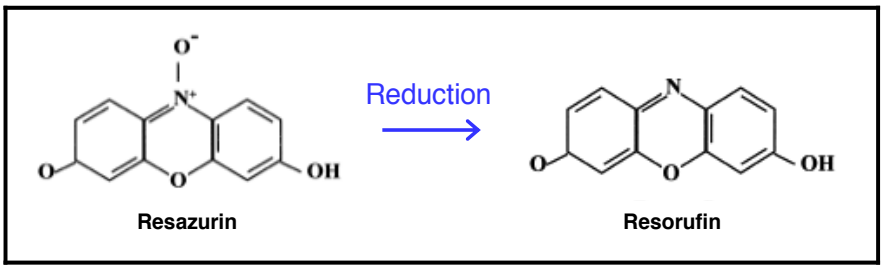

Figure 1.30. *QBlue reaction based on the reduction of resazurin (non-fluorescent) into resorufin (fluorescent) product by the metabolically active cells.*

Resorufin can be also reduced to a non-fluorescent product called hydroresorufin when incubations are extensive (> 5 h according to the manofacturer). As a consequence, aberrant results may be obtained since living cells are producing a weak signal.

In addition, this reaction of reduction has been hypothesized to take place either in the medium or intracellularly (O'Brien *et al.* 2000) due to the fact that some fluorescent product was found in the cytoplasm and nucleus of cells. Oppositely, no presence of dye was observed in the mitochondrias.

Nevertheless, in spite of the place where the reaction occurs, for that it seems indispensable the presence of living cells, which will keep alive after each measurement. Another advantatge of QBlue is to provide an adequate estimation of cell proliferation with larger sensitivity. Further details concerning the protocol followed to perform this technique on cells can be found in section 2.3.3 of the next chapter.

CHAPTER II. Materials and methods

2 *In vitro* experiments

Through this section the materials, methods and protocols concerning all the experiments carried out in this thesis will be given.

2.1 Cell lines and culture conditions

2.1.1 Cell cultures incubated without any chemotherapy compound

The F98 rat glioma cell line was obtained from the ID17 biomedical beamline's collection. This kind of tumor cells has an infiltrative pattern of growth, and also a weakly immunogenic response. For those characteristics the F98 cell model resembles human GBM (Barth 1998).

For the experiments, F98 cells were cultured in flasks of 25 cm^2 with Dulbecco's Modified Eagle's Medium (DMEM) supplemented with 1% penicillin/streptomycin, and with 10% fetal calf serum. Two hundred thousand F98 cells were seeded per well in 24-well plates, and incubated for 48 hours at 37ºC up to reach confluence.

The supernatant of all wells was removed every 24 h and replaced by fresh medium. Despite that step was also performed after each irradiation, orthovoltage-irradiated cells had to stay from 1.5 h to 2 h with that irradiated medium due to the distance between the hospital and the laboratory. The unirradiated controls, however, were exposed to the same conditions.

2.1.2 Cell cultures incubated with cisPt, cisPt-liposomes and cisPt-AuNPs

In this kind of experiments, F98 cells were seeded according to the protocol aforementioned in 2.1.1, and incubated for 24 hours at 37ºC. After that time, all supernatants were removed and replaced by 500 µl of one of the following chemotherapeutic conditions:

- CisPt (Ferrer Farma 1 mg/ml) diluted in medium to reach a final concentration of 7 µM.

- CisPt-liposomes: CisPt 7 µM associated to liposomes of concentrations of 0.75, 2.5 or 5 mg/ml, according to the experiment series.

For that, a first rotavaporation of solvent (chloroform), in which the lipidic compounds are diluted, is needed (see Figure 1.26). The resulting thin PC film generated on the bottom of the receipt must be then rehydratated with the cisPt solution of desired concentration (7 or 15 μM). The size and structure of liposomes will be given by the vortexing intensity at the end of the process, being the MLV liposomes (see Table 1.1) those ones used in the experiments of this thesis.

- AuNPs that were synthesized by the *Institut Català de Nanotecnologia* (ICN) located in Bellaterra (UAB). Those colloidal AuNPs of 7.3 ± 1.2 nm of diameter were stabilized with sodium citrate 2.2 mM. The initial concentration of AuNPs was known to be 8.35 x 10^{11} NP/mL, corresponding to a concentration of Au atoms of around 17 μM. A later dilution with cisPt 7 μM in cell medium was performed in order to reach a final concentration of 3.5 μM of Au atoms and cisPt molecules.

Under those conditions, molecules of sodium citrate surrounding AuNPs were replaced by bigger molecules of BSA present in the cell medium, being responsible of the colloidal AuNPs stabilization as mentioned in section 1.3.3.

CisPt, cisPt-liposomes and cisPt-AuNPs solutions, were all incubated on cells for 24 h. After that time, the wells were re-filled again with fresh medium before exposures with any kind of radiation.

2.2 Radiation exposures and dosimetry

The experimental set-up for *in vitro* irradiations carried out at the ESRF biomedical beamline and those ones taking place at the hospital will be described in the following sections.

2.2.1 Synchrotron radiation techniques

Three different synchrotron radiation configurations were used: i) Monochromatic broad beam radiations at a beam energy of 81 keV performed in the satellite building depicted in Figure 1.13, ii) MBRT, and iii) white beam seamless (BB) irradiations, carried out both in the hutch placed at 40 m from the source (see Figure 1.13).

All irradiations were carried out at the ESRF ID17 biomedical beamline in the 7/8 + 1 filling mode, with 200 mA of intensity approximately.

2.2.1.1 Monochromatic broad beam irradiation

For that kind of experiments, once all supernatants containing metallic solutions were removed and each well was refilled with fresh medium, monochromatic X-rays irradiations tuned at 81 keV were carried out.

- Radiation exposure:

Plates were irradiated vertically (by using a thin colorless sealing tapes) in front of the beam at different doses covering a field of 8 x 4 cm^2 (Figure 2.1) to assure irradiation with the almost the most homogeneous part of the beam. Moreover, to avoid the beam's edge inhomogeneities, the plate-seeding configuration was like those depicted in Figure 2.1.

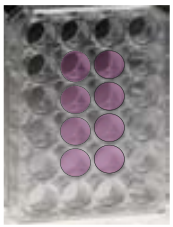

Figure 2.1. *Plate-seeding configuration for monochromatic PAT irradiations. Different plates were used for both treatments, AuNP-cisPt and cisPt alone.*

- Dosimetry:

The dose rate for those irradiations was about 0.5 Gy s^{-1}. The dose calibrations were performed experimentally with a cylindrical ion chamber (PTW 31002 [www.ptw.de]) in water. Those measurements were checked with a high-purity detector set behind the plates.

2.2.1.2 White MBRT and BB radiations

Both white MBRT and seamless irradiations were carried out in the hutch placed at 40 m from the wiggler magnet (Figure 1.13). That white beam passes through several attenuators (C (1.42 mm), Al (1.52 mm), Cu (2.28 mm)) resulting in a beam energy spectrum such as those described in section 1.2.2.4, and with a dose rate of $\sim 5 \cdot 10^3$ Gy s^{-1} (Prezado *et al.* 2009*d*).

- Radiation exposure:

Minibeams were generated by synchronizing the vertical motion of the plate placed on a goniometer with the rotation of the white-beam chopper (Prezado *et al.* 2009*d*). In contrast, the white BB field could be obtained moving the chopper away from the beam path (see Figure 2.2).

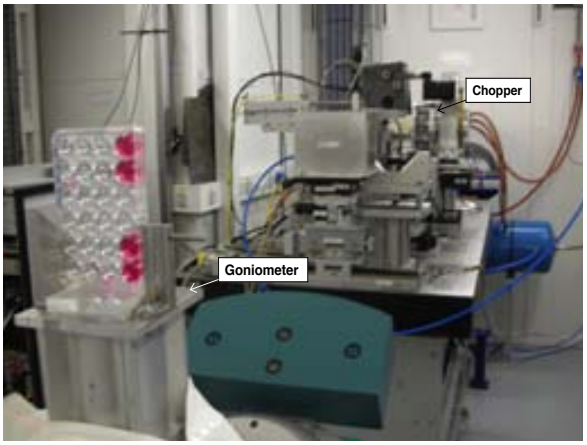

Figure 2.2. *Picture of the white MBRT and BB irradiation set-up, where the chopper, as well as the plate set on the goniometer are highlighted.*

One half of the previously seeded plates were irradiated vertically in front of the beam at different doses with one array of minibeams of 600 μm-width, with a center-to-center (c-t-c) distance of 1200 μm, and covering a field of 2 x 2 cm^2. The other half of plates were irradiated with a white seamless beam mode. For each dose and for each beam configuration (minibeam and white BB irradiation), one different 24-well plate like that shown in Figure 2.3 was used.

Figure 2.3. *Well-seeding distribution. Each plate was covered with an extra-thin and colorless sealing tape enabling the irradiation of the plate vertically*.

In order to avoid an extra dose deposition on cells from the scattering of filled wells contigously, the seeding well configuration for each plate was the same than that showed in Figure 2.3.

Moreover, to have similar valley doses than the ones expected in the further *in vivo* experiments with rats, the wells were filled up with medium, remaining the cells on the bottom, at 1.7 cm depth. If the cell layer had been irradiated directly, in the absence of medium, the peak-to-valley dose ratio (PVDR) would have been much higher than the one calculated for the *in vivo* experiments with rats, due to the reduced scattering filling the valleys (Siegbahn *et al.* 2006).

- Dosimetry:

The dose deposited was assessed by i) Monte Carlo simulations and ii) experimental measurements as it will be explained hereafter, following the protocol described by Prezado *et al.* (2011).

i) Monte Carlo simulations:

PENELOPE 2006 code (Salvat *et al.* 2003) was used for dose calculations. It is widely used in the medical physics field. The program was developed at the *Universitat de Barcelona* (UB).

PENELOPE is the acronym of PENetration and Energy Loss of Positrons and Electrons in matter and is coded in FORTRAN. The program is based on a Monte Carlo simulation package that describes the coupled transport of photons, electrons and positrons in an energy range from 50 eV to 1 GeV in any material system. Hard electron and positron interactions are simulated individually, whereas a condensed simulation is applied for soft interactions (Salvat *et al.* 2003). This classification is based on certain user-defined parameters, such as those described in the simulation of Appendice 1.

The plate geometry was modeled using the geometry package in PENELOPE. Monte Carlo simulations for peak and valley doses assessment were performed. Experimental validation of the calculations were carried out by using radiochromic films placed at different depths in a water-equivalent RW3 material phantom (Prezado *et al.* 2011).

ii) Experimental measurements:

Absolute dose at 1.7 cm depth was measured with an ionization chamber (PTW 31002 [www.ptw.de]) in a water-equivalent RW3 material (Goettingen White Water) with a seamless field of 2 x 2 cm^2. The dose measured in that broad field configuration was converted to peak doses at 1.7 cm by using the phantom scatter factor (Prezado *et al.* 2011). That factor was assessed by using Monte Carlo simulations with PENELOPE 2006 (Salvat *et al.* 2003) and verified experimentally with radiochromic films such those showed in Figure 2.4 (International Specialty Products, http://online1.ispcorp.com).

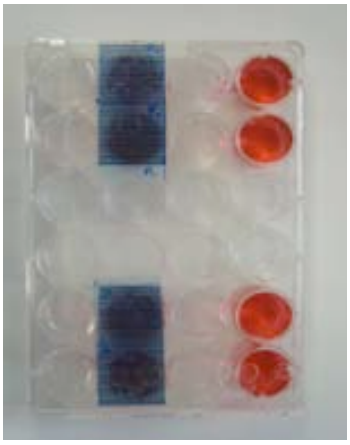

Figure 2.4. *Picture of one 24-well plate with two radiochromic films covering each one a well. These films led us to verify experimentally the dose deposited on cells, specially with MBRT.*

A dose escalation study was performed with both white beams radiation, i.e., MBRT and BB. Moreover, each valley dose for MBRT irradiations (Table 4.1 in Results section) -which becomes critical for the tumor cell recovery after irradiations-, was compared to its identical integrated dose in a seamless field (Table 4.2) in order to perform a further study of the effectiveness of both irradiation modes. The integrated dose was directly calculated as an average of each peak and valley doses.

2.2.2 Clinical Orthovoltage Equipment (COE)

Orthovoltage irradiations were performed at *Hospital Clínic de Barcelona*, with a Gulmay D3100 equipment, with the parameters depicted in Table 2.1:

Potential of electrons	100 kV
Intensity of electrons	10 mA
Filters	0.90 mm Al + 0.05 mm Cu
Half value layer (HVL)	3.3 mm Al

Table 2.1. *Beam quality for an hospital orthovoltage Gulmay D3100 irradiator.*

As explained in section 1.2.3, the spectrum of energy for Gulmay D3100 ranges from 20 to 100 keV approximately, with a mean energy of around 35 keV (see Figure 1.20).

- Set-up and dosimetry:

In order to achieve electronic equilibrium (as in the ionization chamber calibration), a phantom of 10 cm of PMMA was placed under each plate. The plates were placed perpendicularly to the incident beam and a conical applicator was needed in order to focus the photons on the plate as it is shown in Figure 2.5. As a result, the field of irradiation was 10 cm of diameter, and the source-surface distance (SSD) of 25 cm. The bottom of the filled-up plate, where cells were seeded, was taken as a reference point for the dose calculations.

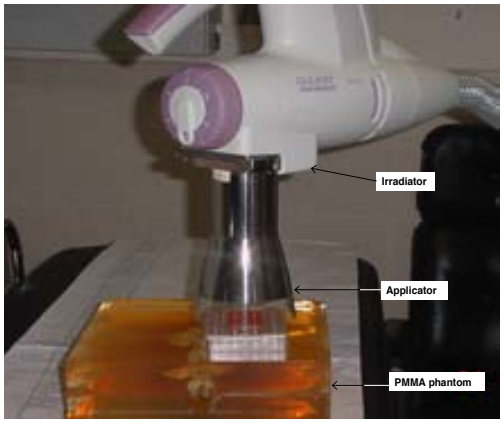

Figure 2.5. *Picture of irradiations with a Gulmay D3100. Plates were placed horizontally under the applicator, and only one dose (three plates) per day was performed.*

The COE provides a dose rate in this point of ~$2 \cdot 10^{-2}$ Gy s^{-1}, which is about 5 orders of magnitude lower than that in white MBRT and BB exposures. It is for this reason that this kind of irradiations took minutes instead of seconds as it happened at the ESRF.

2.3 Techniques to assess the cellular damage

The nuclear damage analyzed in terms of proportion of cells with DSBs, the percentage of different cell populations (alive, apoptotic and dead cells), as well as the metabolic cell recovery over time were analyzed after treatments on F98 glioma rat cells.

2.3.1 Assessment of γH2AX IF by bivariant flow cytometry

As mentioned in the Introduction, the number of DSBs caused by radiation exposures can be correlated to that of γH2AX foci (Rogakou *et al.* 1999), whilst dephosphorylation might coincidence with DNA repair (Kataoka *et al.* 2006). The detection of γH2AX by flow cytometry is based upon the measurement of (immunofluorescence) IF by using a secondary antibody conjugated to a fluorescent dye such as Alexa. The advantages of those kinds of analysis in comparison with other methods such as Western blot, gel electrophoresis and comet assay (Huang & Darzynkiewicz 2006) are i) its several times higher sensitivity, ii) lower-time consuming, and iii) it allows to analyze larger number of cells with an extra information about their position within the cell cycle.

This tecnhique is based on the three steps represented in Figure 2.6, which are further explained below:

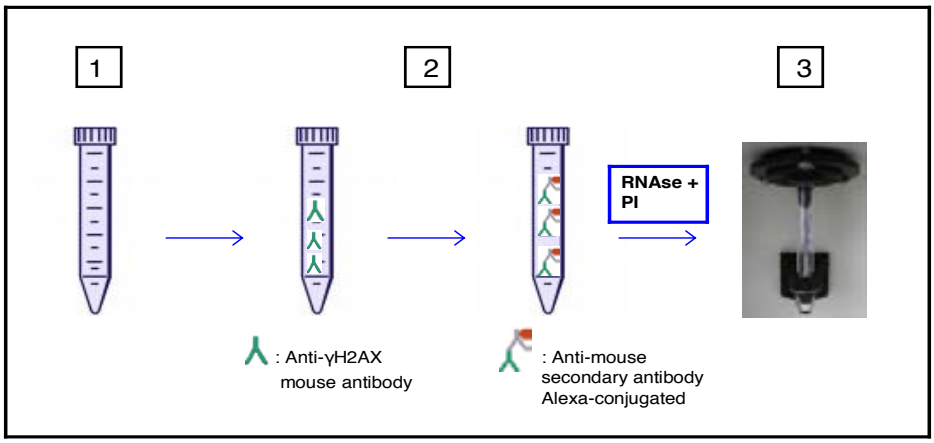

Figure 2.6. *Scheme of the three steps requested for the assessment of γH2AX immunofluorescence: 1) fixation of the cells, 2) staining with the primary and secondary antibodies, and 3) assessment of the immunofluorescence by flow cytometry.*

1st) Fixation of F98 glioma rat cells

Cells were trypsinized at the chosen times after treatments (chemotherapy or radiotherapy). In particular, analyses were performed:

- **2 h after irradiations**, corresponding to the time at which the nuclear damage (DSBs) was almost at its maximum, and

- **17 h after RT**, when cells have already completed their cell cycle, and therefore, they had enough time to repair their nuclear damage.

After trypsinization, pellets were resuspended in 500 µl of phosphate-buffered saline (PBS), and then transferred into 15 ml tubes containing around 4 ml ice-cold 2% methanol-free formaldehyde (FA, Sigma) in PBS. Cells were kept in this fixative (via proteins crosslinking) solution for 15 minutes, and then immediately centrifuged and permeabilized with 5 ml of 70% ethanol. Samples were finally kept at -20ºC until further antibody staining.

2nd) Staining of F98 glioma cells with γH2AX antibody for their analysis by bivariant flow cytometry

Cells were centrifuged at room temperature in order to remove the previous fixative solution. Cell pellets were washed twice in 2 ml 1% bovine serum albumin (BSA, Sigma)-PBS, permeabilized with 0.2% Triton-X-100, and finally resuspended in mouse monoclonal anti-phospho-histone H2AX antibody (1:800 dilution in BSA-T-PBS, Upstate Biotechnology) overnight at 4ºC. This antibody showed however cross reactivity in most common vertebrate cells. After that time, cells were washed with 2 ml BSA-T-PBS and incubated for 1 h at room temperature in the dark, with the secondary antibody, Alexa-488 nm conjugated goat anti-mouse (1:800 dilution, Invitrogen). In order to measure the γH2AX IF intensity as a function of DNA content, after incubation process, cells were immediately washed with 5 ml BSA-T-PBS and counterstained with 5 µl/ml propidium iodide (PI, Roche) and 100 µl/ml DNase-free RNase A (Sigma) in PBS 30 min in darkness (Huang & Darzynkiewicz 2006).

3rd) Assessment of γH2AX immunofluorescence of treated F98 glioma rat cells by bivariant flow cytometry

A number of (1-2) × 10^6 cells were analyzed with a FACSCanto (Becton Dickinson, BD) flow cytometer, with blue-light excitation Argon laser at 488 nm (see Figure 2.7).

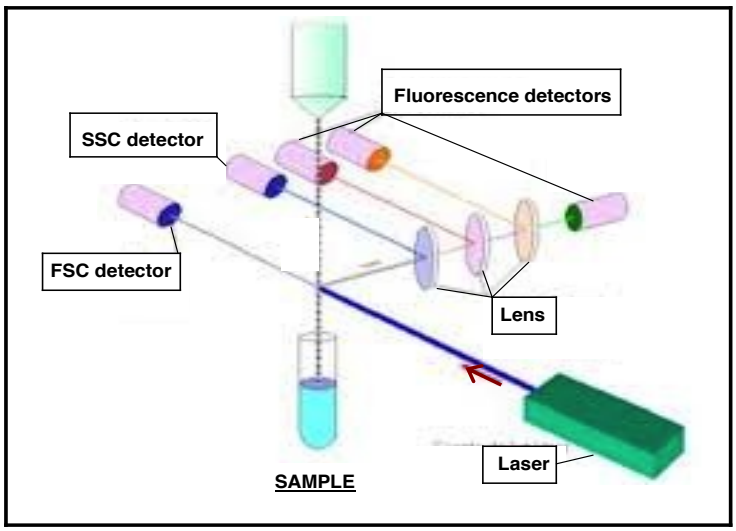

Figure 2.7. *Flow cytometer layout. The laser beam passes through each single cell of the sample. The fluorescence signals emitted by the cells arrive finally to the correspondent detector set at 90º from the incident beam.*

The fluidics of flow cytometer system enables cells pass individually through the laser beam. Light emitted from fluorochromes is focused on the different lens before arriving to the corresponding detector. Laser not only excites the fluorescent dyes within cells, but also allows the determination of the forward light scattered (FSC, associated with cell size) and the side light scattered at 90º (SSC, correlated with the complexity of internal cell organules).

Obtained populations were gated in order to eliminate aggregates. Data were analyzed with WinMDI 2.9 free software (Scripps Research Instituteville, La Jolla CA, USA).

By means of bivariant flow cytometric analysis it is possible to obtain information regarding the percentage of cells emitting this signal due to the presence of DSBs on their DNA, as well as the mean γH2AX IF intensity per cell. Both analyses are explained hereafter:

1) It is feasible to assess the number of cells within the R3 region (depicted in Figure 2.8) by using unirradiated control cells as threshold. Cells in R3 show radiation-induced DNA DSBs. Cells presenting intrinsec γH2AX signal from unirradiated controls were subtracted from the rest of the irradiated samples, remaining only the percentage of phosphorylated histone due to irradiation effects.

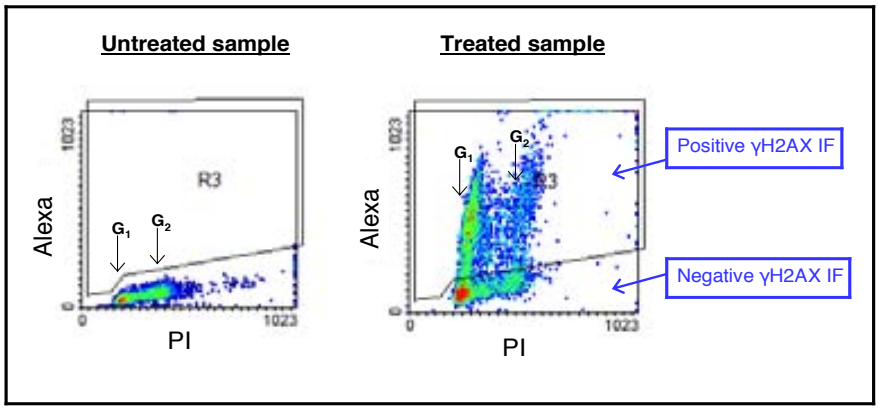

Figure 2.8. *Alexa emission respect to PI signal for untreated and treated samples. Note the positive (presence of DSB) and negative γH2AX IF regions in each one, as well as the G_1 and G_2 cell cycle positions.*

2) In addition, the mean Alexa-488 nm intensity (excitation wavelength at 488 nm and emission at 530 nm) emitted per nucleus was also measured versus linear PI fluorescence (excitation wavelength at 488 nm and emission at 585 nm) obtaining the correlation of γH2AX IF intensity versus cell position in the cell cycle (Figure 2.9).

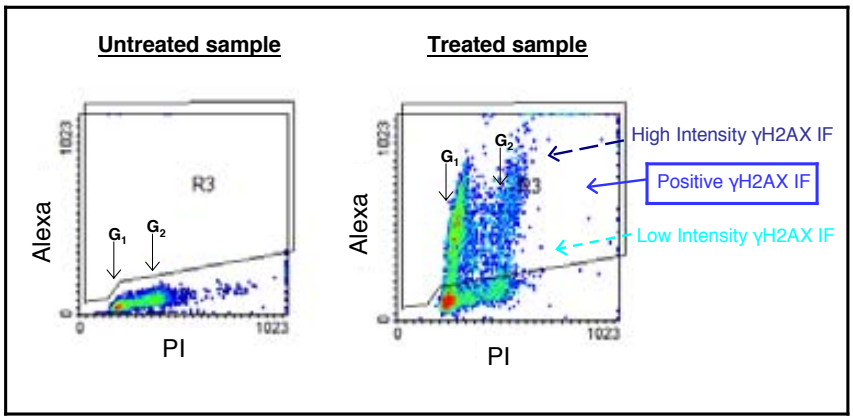

Figure 2.9. *Alexa emission respect to PI for untreated and treated samples. Within the positive γH2AX IF region there is a high fluorescence intensity region corresponding to cells with high number of DSB per nucleus, and low fluorescence intensity region corresponding to cells with low number of DNA DSB.*

Some of cells exhibiting the highest Alexa staining intensity are set at the upper axis in Figure 2.9. Nevertheless, since those cells are englobed by the gated region (R3), they are also included in the analysis.

The assessment of γH2AX IF signal on glioma rat cells was performed at different times (2 and 17 h) after treating cells either with chemo- and/or radiotherapeutic techniques, as mentioned at the beginning of this section. Therefore, the DSBs evoultion could be investigated, as well as the correlation between remaining foci and final cell death.

In particular, the determination and quantification of cellular death were both also assessed by flow cytometry, according to the protocol described in the next section.

2.3.2 Quantification of the different populations (alive, early apoptotic and dead cells) by flow cytometry

The detection of those several cell populations by flow cytometry is based on the two steps represented in Figure 2.10, which are explained below:

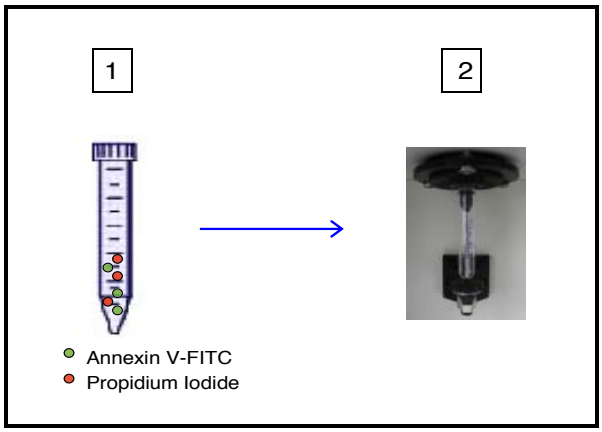

Figure 2.10. *Two steps requested for the detection and quantification of alive, early apoptotic and dead cells: 1) staining cells with annexin-FITC and propidium iodide, and 2) assessment of the fluorescence by flow cytometry.*

1st) Staining of F98 glioma rat cells with annexin and propidium iodide to detect the different cell populations after treatments

Analyses were performed 48 h after irradiations giving cells enough time to undergo necrosis or apoptosis (see Appendice 2). In order to obtain the correct percentage of each cell population it is essential to add the floating cells to the trypsinized ones and analyze all together (10^5 cells at least). Those pellets containing all dead cells were washed twice with PBS, and finally incubated for 30 min with both fluorochromes, annexin and PI 1:300, diluted in a specific binding buffer provided by the Annexin-V-FLUOS staining kit (Roche).

Incubations must be performed in darkness and at 0ºC, by using the anticoagulant protein annexin V (Annexin-V-FLUOS staining kit, Roche), which has a high affinity for the negatively charged PS, conjugated with a fluorochrome such as fluorescein isothiocyanate (FITC). With this method it was possible to identify apoptosis in post-treated glioma cells (Gorczyca 1999, Amirlak & Couldwell 2003).

To detect also late apoptotic and necrotic cells, FITC-conjugated annexin V was used in combination with a DNA staining such as propidium iodide (PI) (Annexin-V-FLUOS staining kit, Roche).

2nd) Cell acquisition by flow cytometry to assess the fluorescence emitted by every single cell

Cell acquisitions were performed by a FACSCalibur (Becton Dickinson) whose layout is depicted in Figure 2.7. It should be highlighted that the main difference between FACSCanto (used for DSBs measurements) and FACSCalibur is the number of detectors in each one: 6 in the first one, and 4 in the other. Despite that, acquisitions could be performed indistinctly with any of them, since both equipments have the detectors required for the fluorochromes used; excitation wavelength at 488 nm and emission at 530 nm for Annexin-FITC (identical to Alexa-488 nm), and excitation wavelength at 488 nm and emission at 585 nm for PI.

After acquisition, the population was gated within the region R1 (see Figure 2.11) in order to eliminate debris, i.e., small fragments. Afterwards, it was represented according to its PI versus annexin signals (Figure 2.11), leading to four different regions.

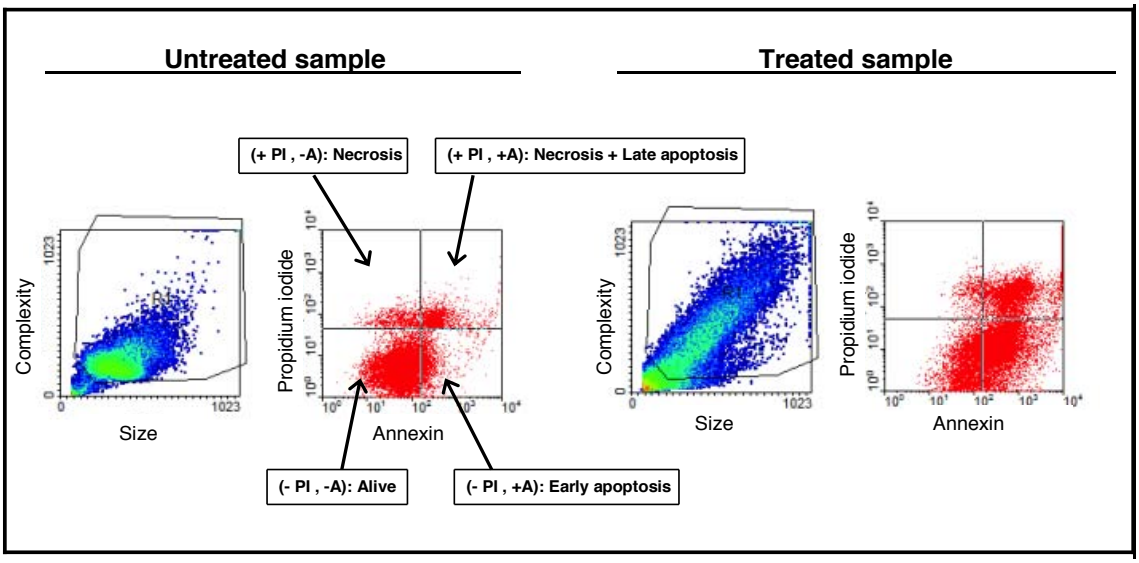

Figure 2.11. *Flow cytometry analyses for controls (left) and treated cells, in this case with cisPt 7 μM for 24 h (right). Firstly, the region of interest was gated on a "complexity-size" plot. Both cell distributions differed clearly in complexity and size due to the high percentage of apoptosis in the treated cells sample. The population gated in R1 is afterwards represented according to its PI (propidium iodide) - A (annexin) signal.*

Quadrants separating those populations were established by using the control sample as reference. Data were analyzed with the WinMDI 2.9 free software (Scripps Research Instituteville, La Jolla CA, USA) as it is depicted in Figure 2.11. Four regions were obtained: 1) living cells (FITC-negative, PI-negative), 2) early apoptotic cells (FITC-positive, PI-negative), 3) late apoptotic cells and 4) necrotic (3 and 4, both FITC-positive, PI-positive). Note that most of the flow cytometric methods do not allow for a clear distinction between late apoptotic and necrotic cells, since in the two cases the dead cells are double-stained with annexin-V-FITC and PI.

Moreover, cells in both upper quadrants are considered completely dead in contrast to early apoptotic ones (lower right). Therefore, they were counted together and defined as necrotic or late apoptotic cells.

2.3.3 Resazurin cell metabolic evaluation assay (QBlue test)

To perform the resazurin or QBlue cell viability test (Qblue Cell Viability Assay kits, BioChain, USA), the remaining living cells just after each irradiation must be trypsinized and counted. After that, ten thousand cells were seeded per well in a 96-well plate, and incubated at 37ºC in order to check the cell recovery of living cells at different days. In particular, QBlue analyses were performed at days three, four or six, and nine after irradiations.

QBlue 10% diluted in cellular medium must be prepared *in situ*, some minutes prior the analysis, adding 20 µl of QBlue per well. The 96-well plates were set into the incubator for 35 min, up to the almost complete resazurin reduction by active cells. In order to avoid a supra-additive fluorescence emission from neighboring cells, 10 µl of each supernatant were transferred into a single well of a dark 96-well plate.

Finally, fluorescence measurements were carried out with a Wallac Fluorometry plate reader (excitation wavelength at 550 nm and emission at 615 nm) at room temperature.

2.4 Study of concentration and distribution of Pt and other trace metals within cells

Several techniques were used to obtain information about the Pt concentration and distribution in different populations of cells, i.e., dead and alive, as a function of the use or not of liposomes for cisPt delivery. The techniques used to assess the metal concentration were:

- Inductively coupled plasma mass spectrometry (**ICP-MS**) and
- Particle induce X-ray emission (**PIXE**) combined with backscattering spectrometry (**BS**).

The first experiment was performed with ICP-MS, and it was very useful in confirming the importance of an adequate cisPt-liposomes ratio in order to obtain an efficient cisPt delivery into the cells. Fortunately, some time later it was possible to carry out some extra experiments with PIXE and BS by using an optimized cisPt concentration. In addition, PIXE/BS allowed to quantify not only the Pt atoms, but also all the trace elements present inside the cells.

On the other hand, the analysis for the metal distribution was done by means of nano-imaging at **ID22NI** (ESRF).

For that purpose, a careful sample preparation and specific experimental set-up such as those ones explained hereafter were requested to carry out each one of the three techniques.

2.4.1 Inductively coupled plasma mass spectrometry (ICP-MS)

ICP-MS is a useful technique to determine and quantify the elements present in a sample.

In this Ph.D. work, the use of ICP-MS allowed to perform a first analysis of the intracellular Pt content as a function of the delivery system, as it will explained in section 7.1.1. For that purpose, a specific preparation of samples was needed previously to the sample's acquisition.

2.4.1.1 Preparation of samples

Preparation of samples for ICP-MS required 3 different steps:

1) Cell culture and posterior chemical treatments
2) The breakage of the samples with Triton-X-100 0.1%
3) Preparation of calibration curves

Firstly, 2 x 10^5 cells/ml were seeded into 24-well plates as previously described in section 2.1.1. After that, cells were incubated for 24 h at 37ºC with 500 µl of each chemical solution by triplicate, prepared *in situ* according to the protocols described in section 2.1.2. The different chemical conditions used were the following:

- Medium for the control group
- CisPt 15 µM in cellular medium
- CisPt 15 µM in cellular medium associated to liposomes of PC 2.5 mg/ml.
- CisPt 15 µM in cellular medium associated to liposomes of PC 5 mg/ml.

After 24 h, due to the lost of adherence of dead cells, they desattached from the plate enabling their separation from remaining living cells. All samples were then centrifuged, and pellets were washed at least three times with PBS 1X. After that, cells were treated with Triton-X-100 0.1% to break its cellular membranes, and allowing the release of intracellular Pt to the liquid solution.

Before the measurements, 200 µl of sample solution were diluted with nitric acid (HNO_3) 1% (diluted in deionised water) up to a final volume of 2 ml. This step was required to destroy the organic matrix (including liposomes), as well as to avoid any contamination. Since the purpose was to determine the concentration of Pt inside cells, a standard calibration curve was needed in order to get a linear trend of "intensity" respect to "concentration of Pt" in parts per billion (ppb). Indeed, one different calibration curve was obtained for the two isotopes of Pt with a higher natural abundace.

To create those standard calibration curves, five different dilutions of well-known concentrations (0, 2, 4, 10 and 20 ppb) were made from the same cisPt solution 1 mg/ml used to prepare the chemical conditions. Like samples, these standard dilutions also contained Triton-X-100 0.1% and HNO_3 1%.

Finally, thallium (^{205}Tl, 70.48% of natural abundance) was added to all samples and standards (for the calibration curves) in a concentration of 1 ppb to act as an internal reference in order to: i) enable monitoring of the instrument performance, ii) correct possible variations due to the matrix effects, and iii) notice variations in the rate of sample entry into the plasma torch.

2.4.1.2 Experimental set-up

The instrument used was an inductively coupled plasma mass spectrometer PerkinElmer Elan 6000 from "*Serveis Cientificotècnics de la Universitat de Barcelona (UB)*", in Barcelona. A model of the equipment is depicted in Figure 2.12, whereas Figure 2.13 corresponds to a real picture of the equipment.

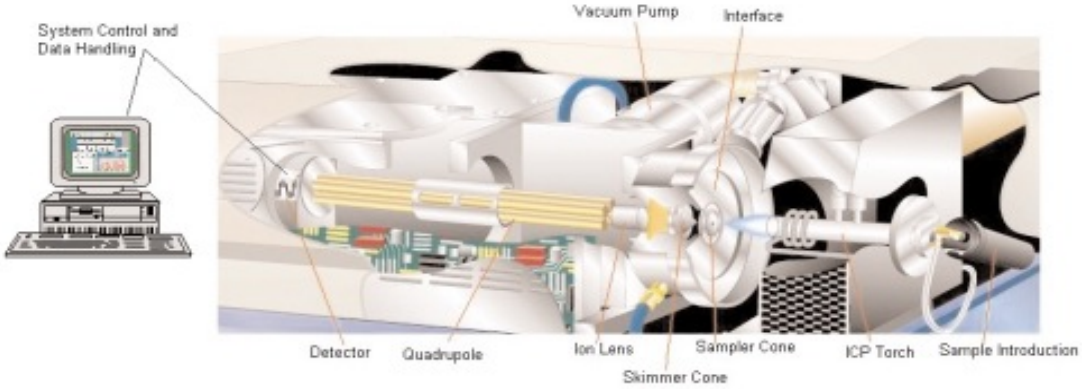

Figure 2.12. *Components of an ICP-MS equipment. Liquid samples are introduced by a peristatic pump and converted into small drops which pass through the ICP torch in order to convert all the atoms of the sample into ions. These charged particles pass through the quadrupole until reaching the detector.*

All the system was under high vacuum to avoid reactions between sample ions and air molecules. The sample was injected by a peristatic pump. At the entrance, a nebulizer converted the liquid to be analyzed into small droplets by mixing the sample with a flow of Ar gas. Those droplets passed through a torch, which reaches temperatures of around 6000ºC, in order to obtain ions from the inicial analyte atoms.

Figure 2.13. *Picture of the ICP-MS placed at "Seveis Cientificotècnics UB" used for the analyses.*

Since ions generated in the torch were almost all positively charged, they tended to repeal each other. In this way, charged metal cylinders were warranted to focus the charged particles by an electric field.

Those focalized positive-charged particles passed through a quadrupole magnet to be separated according to their mass-to-charge ratio (m/z) (Figure 2.14). According to the voltage and radiofrequency of the quadrupole, only the ions of the selected m/z get to pass between the four cylinders.

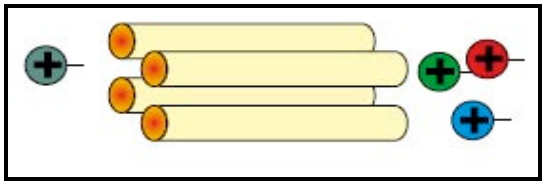

Figure 2.14. *Scheme of a quadrupole magnet of an ICP-MS equipment. Its function is to separate the ions passing through it according to their m/z ratio.*

Thus, at that point, the different isotopes of the element of interest are separated between them. In the experiments described in this Ph.D. dissertation, that element was Pt (Z = 78), which presents the most stable abundant isotopes reported in Table 2.2.

Isotopes	***% of natural abundancy***	***Number of neutrons***
^{194}Pt	32.97	116
^{195}Pt	33.83	117
^{196}Pt	25.24	118
^{198}Pt	7.16	120

Table 2.2. *Summary of the most abundant stable isotopes of Pt.*

In the experiments, however, only the two most abundant isotopes were monitorized, i.e., ^{194}Pt and ^{195}Pt, in order to evaluate possible interferences in the measurements. In that way, since the natural abundances were very similar among them, the concentration of each isotope in the samples must be almost identical. All the calculations concerning those analyses are described in detail prior results, in section 7.1.1.

2.4.2 Particle induce X-ray emission (PIXE) and backscattering spectrometry (BS)

The experiment was carried out at the nanoprobe beamline of AIFIRA facility (*Applications Interdisciplinaires des Faisceaux d'Ions en Région Aquitaine*) with the help of the *Centre d'Etudes Nucléaires de Bordeaux Gradignan* (CENBG, France).

PIXE is a technique based on the measurement of fluorescence X-rays emitted by different elements present in a sample previously excited (Carmona *et al.* 2008). On the other hand, the measurement of backscattered particles, which provide information about the charge and the thickness of the sample, is named BS technique. PIXE and BS must be performed complementary.

Appart from detecting all the elements at the same time within cells, PIXE offers some more advantages over ICP-MS, like those explained hereafter:

- PIXE is a non-destructive technique.

- The use of protons as incoming particles leads to higher ionization cross-sections compared with heavier ions, and to higher sensitivities in comparison with electrons.

- Protons allow to obtain lower background signal, specially from backscattered particles. Thus, it is feasible to obtain fully quantitative results, i.e., results of the concentration of trace elements and the local mass of the sample (Ortega *et al.* 2009).

2.4.2.1 Preparation of samples and cryofixation

Preparation of samples for PIXE and BS required the 3 consecutive steps explained through the following pages (Carmona *et al.* 2008):

1) Preparation of the holder
2) The culture of cells on the holders and the posterior chemical treatments
3) Cryofixation of the samples

The first step was thus the holder preparation to enable the seeding of cells on it.

The sample holder is a rectangular piece of ~2 cm lenght with a 5-mm hole in the center such as those depicted in Figure 2.15. It must be previously sterelized in an autoclave before the fixation on it of a 2 µm thickness non-toxic polycarbonate film under sterile conditions. They both must be finally washed by immersion in ultrapure ethanol for 1 h, and afterwards left to dry in sterile conditions at least for 2 h.

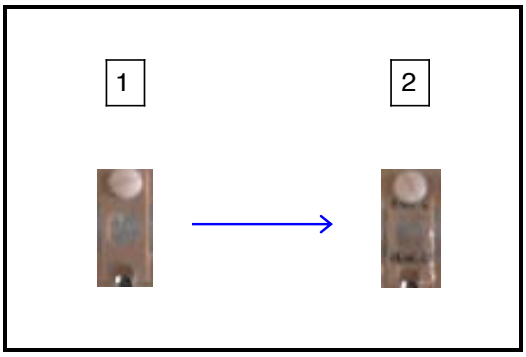

Figure 2.15. *Pictures of 1) untreated holder, and 2) holder treated with polycarbonate.*

After that time, cells were cultured directly on the sample holder. With that aim, the polycarbonate film was required to be pretreated with 2 drops of gelatin gel solution 2% v/v in sterile water for 10 min at 37ºC.

Excess of gelatin was removed carefully, and then the holder was rinsed twice with 50 µl of high purity sterile water. After that, holders were left to dry overnight under a laminar flow hood. Once dried, 10^5 cells/ml were seeded into the holders, waiting for 24 h at 37ºC before to incubate them with the different chemical treatments, which were prepared *in situ*.

For incubations, 1 ml of each solution was added into one different well of a 12-well plate. Each holder containing attached cells was submerged into one different well, with a different treatment condition. Incubations were left for about 24 h and at 37ºC. All treatments, which are briefly described hereafter, were performed at least by triplicate:

- Medium for the control group
- CisPt 7 µM in cellular medium
- CisPt 7 µM in cellular medium associated to liposomes of PC 0.75 mg/ml.

24 h after those treatments, only dead cells desattached from the polycarbonate, and those supernatants were picked up and centrifuged. Pellets for each condition must be fixed on the polycarbonate film, as it was described before. However, an extra µl of gelatin were needed on each holder since dead cells had lost its adherence. According to our knowledge, this was the first time that dead cells were dried frozen for their subsequent fluorescence analysis.

At the end, holders containing either survival or dead cells must be dried-frozen by using a cryofixation technique which ensured the prevention of biological structures, as well as chemical composition and distribution within cells. For that, the removal of all molecules of water from cells was required. The protocol used for the cryofixation of samples was those briefly exposed hereafter:

1st) Each holder must be rinsed with a PBS solution.

2nd) A second rinse with high-purity water was needed in order to eliminate all ions present in the PBS. The excess of water was carefully dried (avoiding the contact with the polycarbonate) by using filter paper.

3rd) Each sample was submerged into nitrogen-chilled isopentane at -160ºC for 20 seconds.

4th) Finally, holders were placed into a cryostat at -35ºC during several weeks in order to eliminate the small-size ice crystals within samples by sublimation at low temperature.

Samples were set some days in an oven, and finally kept into a diseccator until their analysis.

All the steps concerning the analysis of these data can be found in section 7.1.2, as an introduction to the PIXE results.

2.4.2.2 Experimental set-up

The experimental set-up for the two complementary techniques described before, PIXE and BS, is depicted in Figure 2.16.

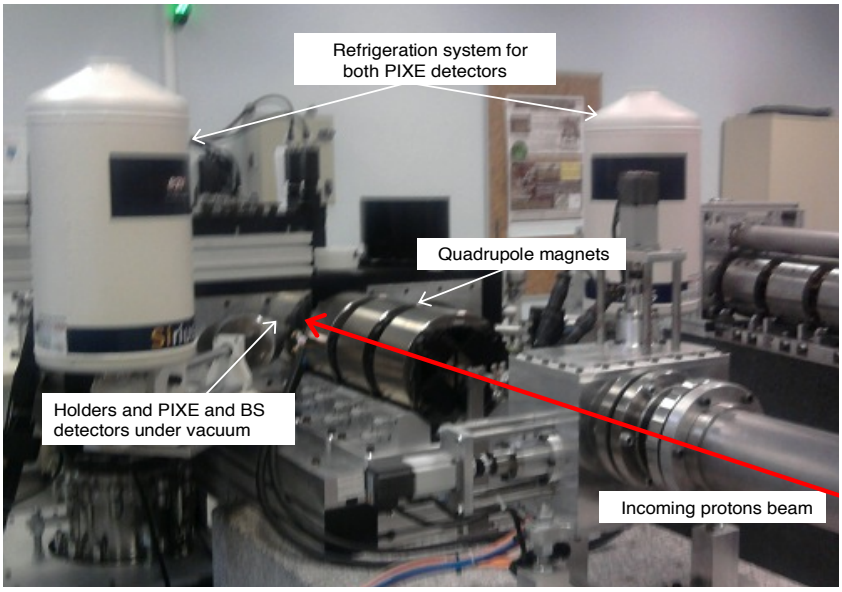

Figure 2.16. *Picture of the experimental set-up of AIFIRA for PIXE and BS. The incoming protons beam (red arrow) is focalized by several quadrupole magnets before to reach the holder placed under vacuum conditions.*

Irradiations were performed with incident H^+ particles (represented as a red arrow in Figure 2.16) with an energy of 3 MeV and 2.5 μm of beam diameter. The mean current intensity was around 0.6 nA. In all cases, the particle beams were scanned on the surface of samples by using

deflection slits. In particular, the squared scanning dimensions chosen for the analyses ranged from 12 to 200 μm according to each sample. The scanning dimensions were inversely correlated to the exposure time per sample. For instance, time exposures ranged from 2.5 h for samples with higher content of Pt (lower scanning dimensions), up to 12 h for those samples with lower metal concentration (higher scanning dimensions), such as surviving cells treated with cisPt either free or associated to liposomes. The detection limit of PIXE under those conditions was of 2 μg of element/g of sample.

All samples were irradiated under vacuum conditions, inside the metal box depicted in Figure 2.16. Detectors were also placed in vacuum, surrounding the sample (see Figure 2.17). In particular, the two 80 mm^2 PIXE Si(Li) detectors were set 22 mm from the sample and at 45º with respect to the incident protons. They were protected with 300 μm thick carbon filters in order to avoid radiation damage. Backscattered protons were simultaneously detected by a silicon detector placed at 25 mm from the sample and at 35º to the incident protons.

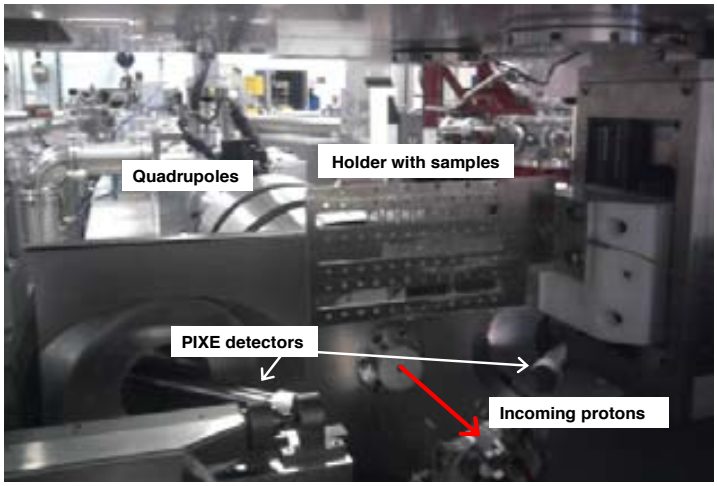

Figure 2.17. *Inner box where both holder and detectors must be set under vacuum conditions. Note that both PIXE detectors were protected by 2 carbon filters (in white).*

Three holders of well-known metal concentrations and thicknesses (reference samples), in the form of thin layers depicted in Figure 2.18, were irradiated as well in order to obtain the solid anlgle of the detectors (see section 7.1.2). Those three samples were: CsBr (superficial mass = 538 $\mu g/cm^2$), Fe (superficial mass = 564 $\mu g/cm^2$) and ZnTe (superficial mass = 467 $\mu g/cm^2$).

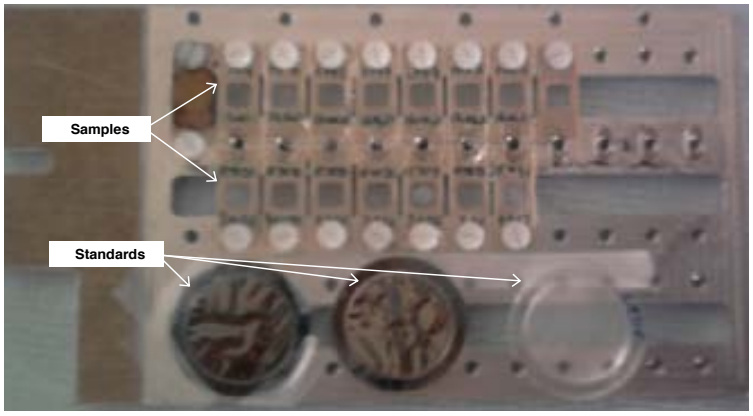

Figure 2.18. *Picture of the holder used to fix both samples and reference samples on it for irradiations. Note that it is the same that those depicted in Figure 2.17, inside the metal box.*

2.4.3 ID22 Nano-Imaging (ID22NI)

Analyses of metal distributions were performed at the Nano-Imaging station ID22NI (ESRF). The beamline's potential for simultaneous trace-element detection and mapping make it ideal for biology. The principle behind the nano-imaging station ID22NI is the detection of the X-ray fluorescence emitted from sample atoms excited with a hard X-ray nanometer beam. The energy of the emitted X-rays is characteristic of the excited element, enabling the identification of the sample's composition.

Synchrotron X-ray fluorescence emission was used only to determine the metal distribution within cells. One of the main reasons for that was the lack of enough data to obtain quantitative results, since only one or two cells per condition could be irradiated. In addition, in samples containing liposomes, the presence of these vesicles interfered in the quality of images since they appeared covering part of the cells.

Despite those inconvenients, the distribution of each element could be analyzed in ID22NI. The analysis was focused only on living cells since they offered a good preservation of their structures, keeping intact their membranes. Samples used to carry out these experiments were exactly the same that those analyzed at the CENBG, although different cells of each holder were analyzed in both techniques.

2.4.3.1 Experimental set-up

The ID22NI beamline uses the synchrotron beam provided by an undulator placed into the straight section of the storage ring, and which is at 64 m far from the experimental hutch.

Before reaching the sample, the white beam was energetically filtered with a flat horizontally deflected Si mirror that produces a pink beam. Finally, a pair of Si mirrors in Kirkpatrick-Baez configuration focused the pink beam (Figure 2.19) (Martinez-Criado *et al.* 2012).

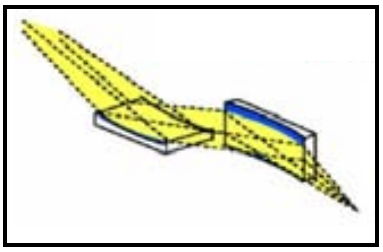

Figure 2.19. *Scheme of a Kirkpatrick-Baez mirror optics used to create a nanometer-size hard X-ray beam..*

Based upon two elliptical multilayer coated Si mirrors in cross geometry, the focusing device provides around 10^{12} photons/s with an energetic resolution ($\Delta E/E$) of 10^{-2} (Martinez-Criado *et al.* 2012). At 17 keV the resulting beam dimensions were about 65 x 60 nm^2 (H x V) on the focal plane. That hard X-ray nanoprobe allows X-ray fluorescence emission the determination of the intracellular distribution of the trace and major elements at nanometer length scale.

The sample was raster-scanned using an XY translation piezostage, while collecting the X-ray fluorescence signals by using energy-dispersive Si drift detectors (Martinez-Criado *et al.* 2012) located side-to-side at 15 degrees with respect to the sample surface (see Figure 2.20).

The posterior analysis of samples was performed according to the protocol described in section 7.2.

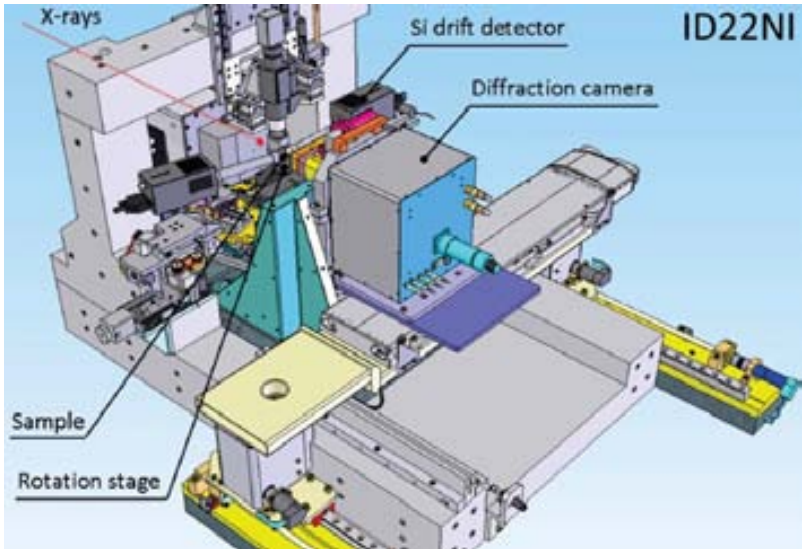

Figure 2.20. *Layout of the main part of ID22NI end station, extracted from Martinez-Criado et al. 2012. In the picture, as the sample as the Si detector are denoted. The incomimg X-rays are represented as a red arrow.*

2.5 Statistical study of analyzed data

All experiments were performed at least by triplicate, whereas the QBlue test was done up to eight times per dose and radiation mode. For the several experimental conditions, dose-response data were evaluated using a standard two-factors analysis of variance (ANOVA) test in order to determine how the response varies depending on dose, drug concentration, time of incubation or radiation mode, as well as the interaction between each couple of them. Further comparisons among doses, concentrations or incubation times were Bonferroni-corrected using GraphPad Prism. Probability (P) values less than 0.05 were considered significant, whereas asterisks denote the following cut-off differences between them: $*p < 0.05$, $**p < 0.01$, $*** p < 0.001$.

Results for control cells (cells without any radiation treatment) obtained from the flow cytometries were considered as having 100% of survival and 0% of both, death and early apoptotic indexes. The values for the rest of the cellular populations obtained from flow cytometric analyses were normalized to the control group.

3 *In vivo* experiments

A dose escalation study was performed in order to determine the tolerance doses on healthy brains. Male Fisher 344 rats (provided by Charles River, France) were used for this experiment, following strictly all procedures related to animal care conformed to the Guidelines of the French Government, and by the review of the Internal Evaluation Committee for Animal Welfare and Rights of the ESRF.

3.1 Radiation exposure

MBRT irradiations were carried out in the hutch placed at 40 m from the wiggler magnet as it was depicted previously in Figure 1.13 in section 1.2.2.2. For irradiations, animals were anesthetized *in situ* with 2.5% isofluorane inhalation. Rats were layed on a home-made holder, where they were fixed by the mouth, as it is depicted in Figure 3.1. The holder was set on high precision goniometer. As in the case of cell irradiations, a radiochromic film HD 810 was placed in front of the rat head to ensure the quality of each exposure.

Figure 3.1. *Positioning of a rat on the goniometer for MBRT irradiations. Rats were anesthetized in situ with isofluorane inhalation.*

A total of 46 rats were irradiated laterally by an array of horizontal minibeams of 600 μm width and 1200 μm c-t-c distance, which covered the whole brain. Note that these values for MBRT irradiations were identical to the previously used for *in vitro* experiments.

- Dosimetry:

Like in *in vitro* experiments, the dose deposited on the rat brain was assessed both theoretically (by Monte Carlo simulations) and experimentally, following the protocol described by Prezado *et al.* (2011).

Absolute dose at 1.0 cm depth was measured with an ionization chamber (PTW 31002 [www.ptw.de]) in a water-equivalent RW3 material (Goettingen White Water) with a seamless field of 2 x 2 cm^2. The dose measured in that broad field configuration was converted to peak doses at 1.0 cm by using the phantom scatter factors calculated by Monte Carlo with PENELOPE 2006 (Salvat *et al.* 2003), which was briefly described in section 2.2.1.2. Experimental validation of the calculations was carried out by using radiochromic films placed at different depths in the water-equivalent RW3 material phantom.

Monte Carlo simulations were also used to assess the PVDR and valley doses from the peak. At that point, minibeams were generated by combining the vertical motion of the plate placed on a goniometer with the rotation of the white-beam chopper (Prezado *et al.* 2009*d*). The maximum field dimension achievable was 3 mm height. Because of the very thin beam height, rats should be scanned vertically through the beam to cover an area of 8 x 8 mm^2.

Rats were separated in six groups according to the prescribed dose at 1 cm depth of brain. Both the doses and the number of rats per group are reported in the following Table 3.1:

Series	*Number of rats*	*Peak Dose (Gy)*	*Valley Dose (Gy)*
1	5	50	3.3
2	9	100	6.6
3	9	150	10.0
4	9	200	13.3
5	9	250	16.6
6	5	400	26.3

Table 3.1. *Peak and valley doses prescribed at 1-cm depth in the brain, as well as the number of animals used in each series.*

3.2 Follow up of the animals and survival analysis

Three rats were kept alive in series from 2-6, and two rats in series 1 to assess the survival plots and the consequent follow up analysis. The follow up of the animal was performed by members of the collaboration up to 18 months after irradiations, when all the surviving rats were euthanized. The rest were euthanized few hours after irradiations to perform histopathological studies, which are still in progress. Magnetic ressonance images of the rat brains were also been obtained. Signs such as weakness, difficulty to feed, excitability etc. were recorded regularly. Rats were weighted twice per week from the third day after irradiations. Indeed, the weight at day three could be considered as approximately the same one that rats had the day of irradiation.

The lapse of time between irradiation and death was considered survival time, which was calculated for each series. A subsequent Kaplan-Meier graph was plotted showing the percentage of survival versus days after irradiation, up to 100 days. The survival curves were compared between the irradiated groups by using a log-rank test. Rats showing visible clinical symptoms of radiation-induced damage (Laissue *et al.* 1998) were euthanized by intracardiac injection of sodium pentobarbital at less than 1 day before their anticipated death.

CHAPTER III. Results: *In vitro* experiments I

4 Comparison of effectiveness of white MBRT and BB synchrotron radiations

One of the main aims of this thesis was to find the endpoint for MBRT for the treatment of radioresistant glioma cells. The **endpoint** is the threshold dose from which a significant enhancement in the effectiveness of a treatment is achieved. This enhancement was evaluated by ANOVA test described in section 2.5, and it can be analyzed either i) in terms of nuclear damage (DSBs) induced on cells, or according to ii) the percentage of surviving cells and iii) its recovery ability. Comparisons of effectiveness of MBRT with seamless irradiations were performed. In addition, new ways based on the concomitance of chemotherapy and RT were also explored since they might allow to decrease the endpoint of radiation treatments.

A dose escalation study was performed in order to delimit the range of doses where a therapeutic effect for MBRT and white broad beam (BB) could be expected for F98 cell line. The effectiveness of MBRT and BB irradiations was compared by taking MBRT valley doses as a reference. The valley dose plays a crucial role in determining the MBRT effects, since it delimits the survival of the cells between the high peak doses (Dilmanian *et al.* 2002). The higher the valley doses are, the higher the density of lesions in the tumor is. Therefore, a higher tumor control probability may be expected, to be confirmed in future animal studies. Hence, an escalation taking as a reference the valley dose seemed justified.

Tables 4.1 and 4.2 report the doses in MBRT and BB respectively, evaluated in this work. Note that valley doses represent the 10% of the peak doses. The integrated dose has been directly calculated as an average of each peak and valley doses (Table 4.1) since the width is equal to the space between beams.

Peak dose (Gy)	63	126	189	252	315	420
Valley dose (Gy)	6	12	18	24	30	40
Integrated dose (Gy)	34.5	69.0	103.5	138.0	172.5	230.0

Table 4.1 *Peak and valley doses (standard error, SE = ± 5%) delivered with MBRT. The integrated dose represents the mean dose deposited between the peak and the valley regions*.

Dose (Gy)	6	12	18	24	30	40

Table 4.2. *Doses (SE = ± 5%) delivered with a seamless irradiation. Note that these doses are the same than the valley doses in the case of MBRT.*

4.1 Assessment of γH2AX IF on the cellular DNA: 2 and 17 h after irradiations

Results concerning the nuclear cell damage after MBRT and BB irradiations are presented hereafter.

- Assessment of γH2AX IF in F98 glioma rat cells analyzed by bivariant flow cytometry 2 h after irradiations:

Irradiated F98 glioma cells, specially those at higher doses, are expected to be largely damaged around 2 h after MBRT or BB treatments. In fact, from 60% to 90% of cells exhibit γH2AX IF signal after both MBRT and BB irradiations (Figure 4.1), with a similar linear-quadratic trend as a function of dose. Moreover, in both configurations a (valley) dose of around 12 Gy is required to achieve a plateau in the percentage of cells with DSBs (around 90%). This suggests a saturation of the radiation-induced damage in this high-dose range.

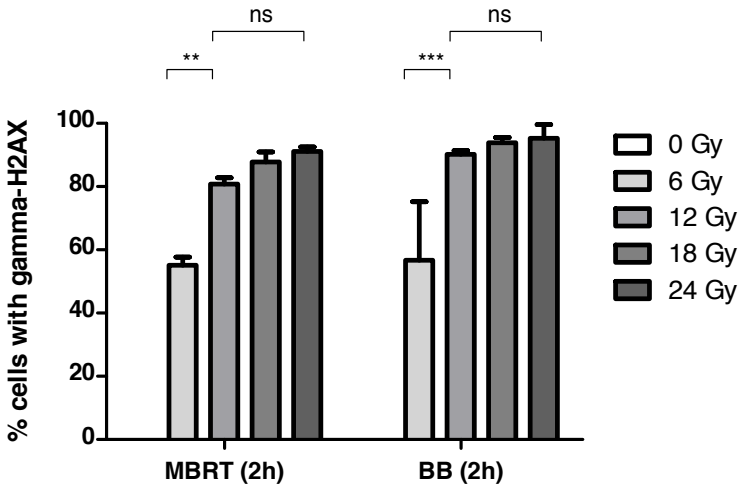

Figure 4.1. *Percentage (%) of cells with γH2AX 2 h after both synchrotron radiation modes (MBRT and BB), as a function of (valley) doses from 0 to 24 Gy. A very similar trend is observed after both synchrotron radiation modalities.*

The γH2AX IF intensity, i.e., the frequency of DNA DSBs induced on cells differs between MBRT and BB (Figure 4.2).

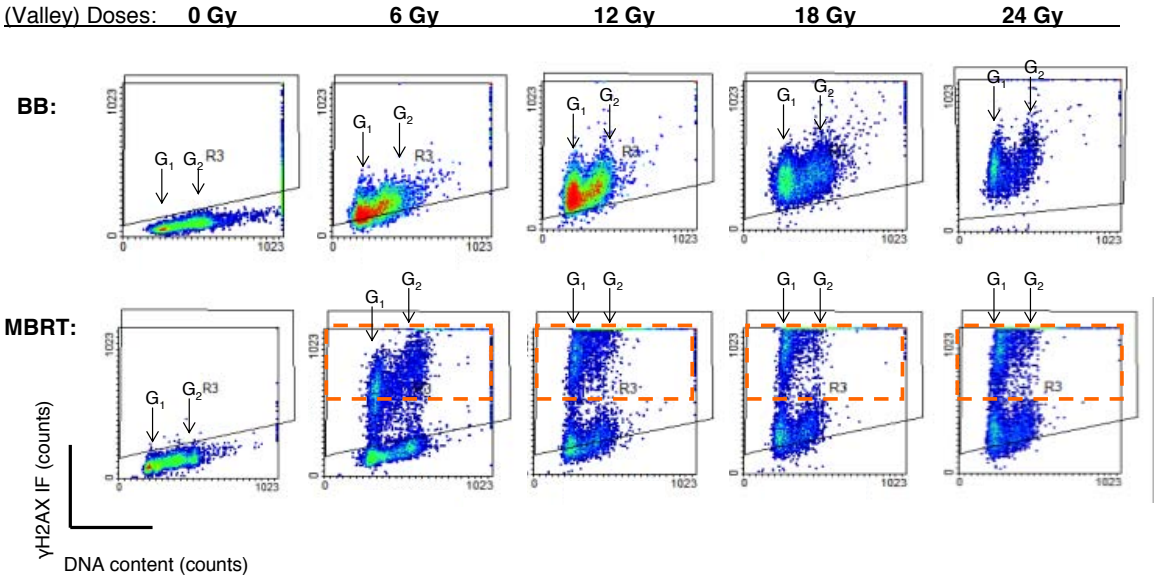

Figure 4.2. *γH2AX IF versus cellular DNA content stained with PI of F98 glioma rat cells 2 h after irradiation with BB and MBRT. Different (valley) doses (0, 6, 12, 18, 24 Gy) were investigated. Cells in G_1- or G_2-phase are indicated in the plots. Dashed squares of the MBRT plots denoted the cell populations with a dose-dependent high intensity of γH2AX. Although the experiment was performed at least by triplicate, only the result of one series is shown.*

It should be highlighted that cells exhibiting the highest Alexa staining intensity, like those irradiated with MBRT at higher doses, are included in the analysis despite to be set at the upper axis. This is due to the fact that those cells are englobed by the gated region, as explained in section 2.3.1 of Materials and methods.

MBRT generates a greater amount of DSBs per cell nucleus compared with BB (Figure 4.2). Moreover, at doses up to 24 Gy, two well-separated populations can be detected 2 h after MBRT exposure as a function of the γH2AX IF intensity. The population highlighted in each plot by a dashed square might correspond to those glioma cells containing the highest proportion of DSBs per nucleus. This may be a consequence of those higher doses deposited by each minibeam path, i.e., the peak region, as well as those more moderate doses within the penumbras regions of minibeams (see Figure 4.3).

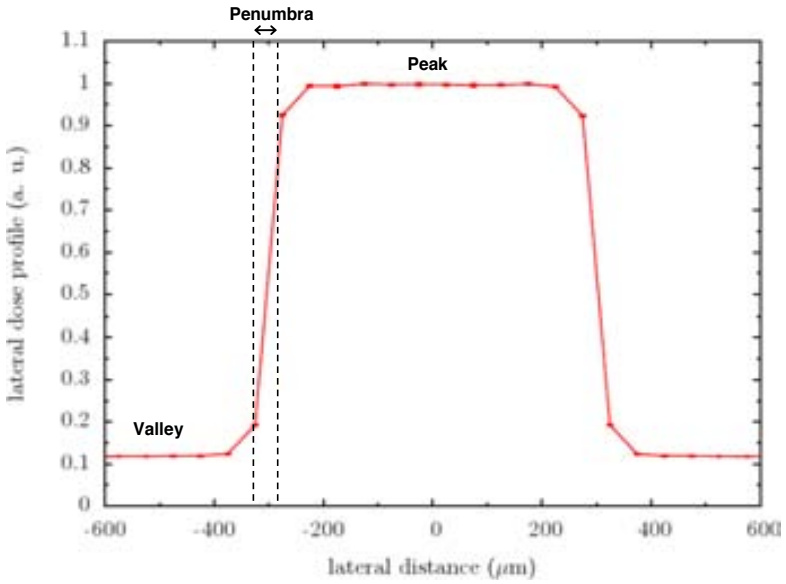

Figure 4.3. *Dose profile courtesy of Dra. Immaculada Martínez including one peak and a half valley region. The penumbra is the lateral distance, (40 μm in this case) in which the dose falls down from 80% to 20% of the central peak dose.*

On the other hand, the lower population could be correlated to those γH2AX IF positive cells irradiated at the valley region. This population with a lower γH2AX intensity resembles that detected in the BB mode when both valley and seamless dose are equal.

- Analysis of γH2AX IF intensity according to the DNA content of F98 glioma rat cells 2 h after irradiations:

Regarding the DNA content, measured by nuclear labeling with PI (Figure 4.2), the induction of DSBs became higher in G_1 rather than in S and G_2 phases, despite the fact that MBRT- and BB-induced DSBs occurred in all phases of the cell cycle.

- Assessment of γH2AX IF in F98 glioma rat cells analyzed by bivariant flow cytometry 17 h after irradiations:

After 17 h cells are able to complete their progression through the cell cycle, and thus, to decide whether remaining arrested in the different phases of the cell cycle delaying the cellular dead process, or to undergo apoptosis or necrosis. Hence, since remaining foci after the doubling time

of F98 glioma rat cells could be correlated with lethal lesions, extra analysis has been performed 17 h after MBRT and BB exposures.

According to Figure 4.4, a greater decrease in the number of γH2AX positive cells is observed for glioma cells 17 h after BB irradiations in comparison with MBRT exposures.

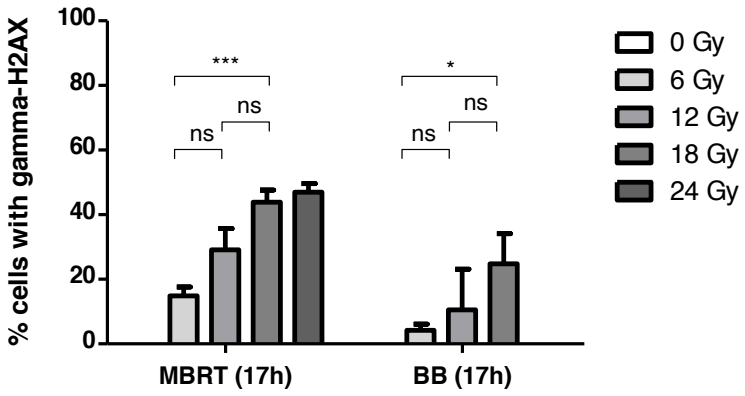

Figure 4.4. *Percentage (%) of cells with γH2AX 17 h after MBRT and BB as a function of (valley) dose from 0 to 24 Gy. Regardless of the dose, a larger proportion of cells exhibited DSBs 17 h after MBRT exposures in comparison with white BB irradiations.*

After 17 h the decrease in the percentage of damaged cells for the seamless mode is ≈ 67%, whilst for minibeams is ≈ 45%. This seems to be associated to a higher DSBs repair efficiency with BB rather than with MBRT. However, for both radiation techniques the endpoint, understood as the threshold dose to detect the larger % of cells with γH2AX, can be established at around 12 Gy.

The γH2AX IF intensity seems to increase inside the cells irradiated with MBRT and BB at doses ≥ 12 Gy, pointing again at this dose as the endpoint for both techniques (Figure 4.5).

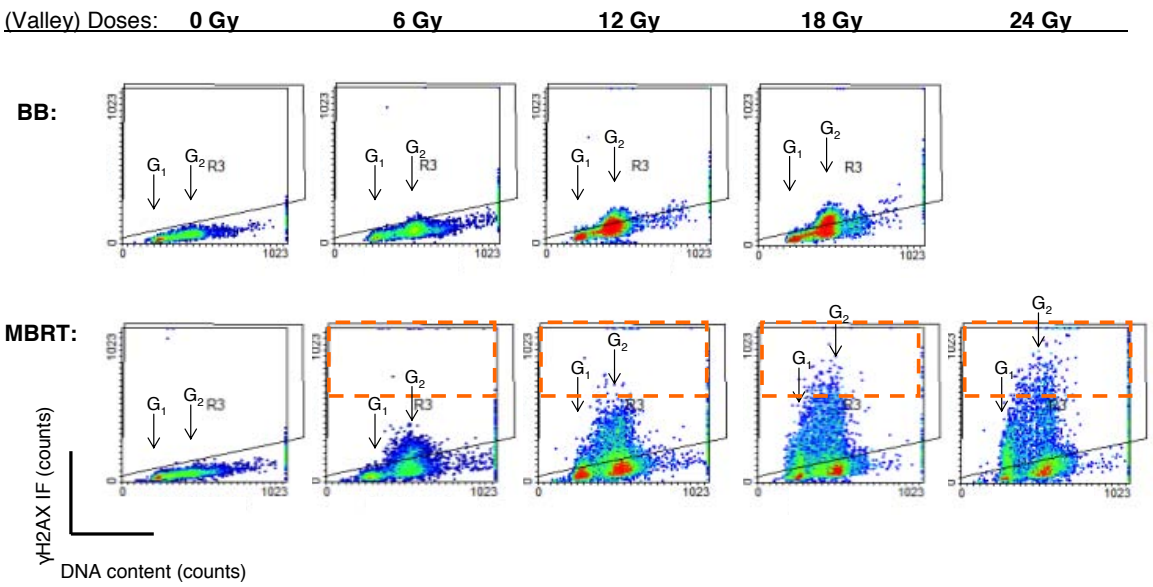

Figure 4.5. *γH2AX IF versus cellular DNA content stained with PI of F98 glioma rat cells 17 after irradiation with BB and MBRT with 0, 6, 12, 18, 24 Gy (valley) doses. Note that in this case, analysis with BB at 24 Gy were not performed. Cells arrested in G_1- and G_2-phase appear indicated in the plots. Dashed squares denoted the cell populations with a dose-dependent high intensity of γH2AX that has been detected 2 h after MBRT. Although the experiment was performed at least by triplicate, only the result of one experiment is shown.*

There is a substantial decrease of γH2AX IF cellular intensity at 17 h after both MBRT and BB irradiations. The intensity depends on the dose, and a more intense γH2AX signal within the cell nucleus can still be detected after MBRT compared with BB irradiations. This fact could explain the higher percentage of cells repaired after BB radiations rather than with MBRT as depicted in Figure 4.4.

In particular, in the minibeam-induced damaged cells gated in R3 region, only one large population can be detected at 17 h (see Figure 4.5), instead of two as observed at 2 h (Figure 4.2).

- Analysis of γH2AX IF intensity according to the DNA content of F98 glioma rat cells 17 h after irradiations:

Analysis of γH2AX IF intensity as a function of DNA cell content 17 h after irradiations (Figure 4.5) reveales that both γH2AX positive, as well as undamaged cells are arrested mainly in G_2 phase after their progression through the cell cycle for both white MBRT and BB exposures.

As it can be observed in Figure 4.5, the higher the dose, the higher the proportion of cells arrested in G_2 phase for both MBRT and BB. In addition, MBRT also induces a dose-dependent accumulation of glioma cells in G_1 phase.

4.2 Survival analysis assessed by flow cytometry

Flow cytometric analyses were performed 48 h hours after treatments in order to elucidate whether the higher proportion of unrepaired or misrepaired γ H2AX foci 17 h after MBRT, would lead to a larger proportion of dead cells.

For this analysis, cell irradiations were performed up to (valley) doses of 40 Gy for both MBRT and BB exposures in order to investigate the possible cell survival at those higher doses.

Normalized data for unstained surviving cells (Table 4.3), and plotted in histograms in Figure 4.6-A indicate the same dose-response for both types of irradiations. Other common observations for MBRT and BB are: i) a significant decrease in survival for cells irradiated up to 12 Gy, from which a saturation on the cell survival seems to exist, and ii) the same percentage of living cells for doses higher than 12 Gy. Thus, according to these data, the endpoint can be established around 12 Gy for both irradiation modes, as it is depicted in Table 4.3.

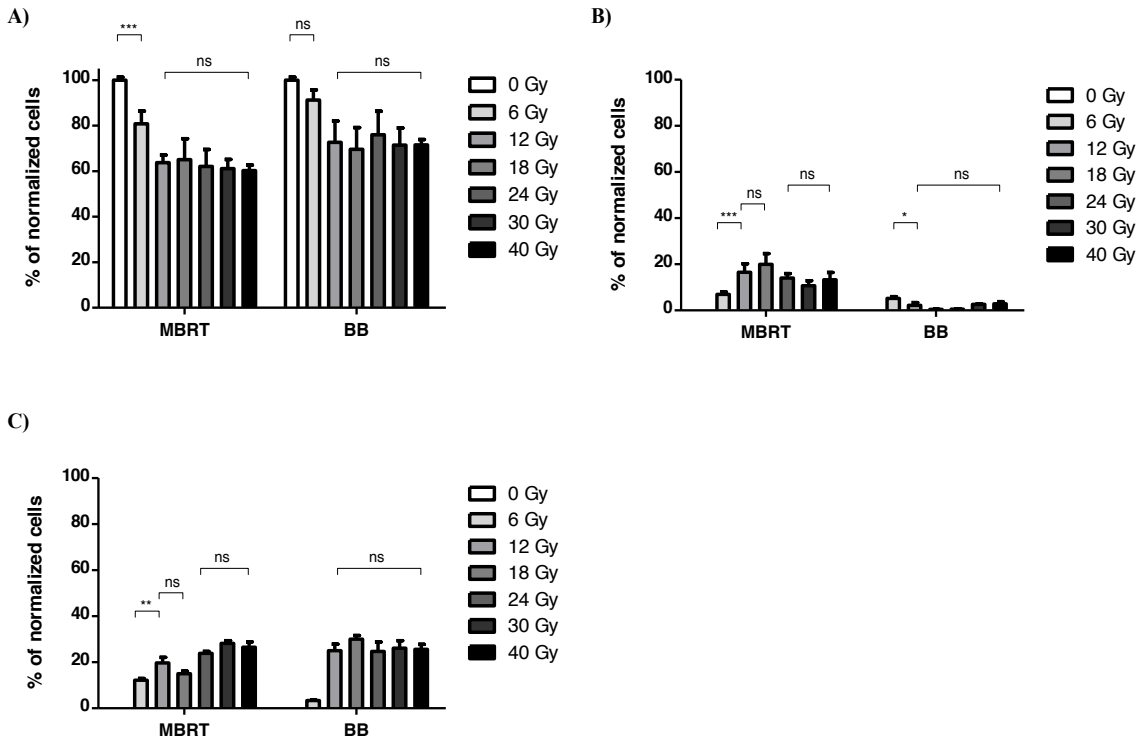

Figure 4.6. *Percentage of normalized A) living, B) early apoptotic and C) dead cells after MBRT and BB irradiations. The doses employed range from 0 to 40 Gy.*

Seamless and valley doses (Gy)	*% of normalized surviving cells after MBRT (Mean % ± SE)*	*% of normalized surviving cells after BB (Mean % ± SE)*
0	100	100
6	81 ± 6	91 ± 5
12	64 ± 3	73 ± 9
18	65 ± 9	70 ± 10
24	62 ± 8	76 ± 10
30	61 ± 4	71 ± 8
40	60 ± 2	72 ± 2

Table 4.3. *Percentages of normalized values for surviving cells analyzed by flow cytometry 2 days after MBRT (valley doses) and BB. These data are graphically represented in histograms in Figure 4.6-A.*

Despite this common endpoint analyzed by flow cytometry, and which is coherent with the previous data obtained by γH2AX IF detection, approximately a 10% decrease in living cells are observed 48 h after MBRT irradiation (see Table 4.3). In addition, the process of cell death clearly differed as a function of dose, as well as of the synchrotron radiation mode. Indeed, one of the most interesting findings is the significant increase of cells undergoing early apoptosis 48 h after MBRT compared to BB exposures (Figure 4.6-B and Table 4.4).

Seamless and valley doses (Gy)	*% of normalized early apoptotic cells after MBRT (Mean % ± SE)*	*% of normalized early apoptotic cells after BB (Mean % ± SE)*
0	0	0
6	7.0 ± 1.0	5.2 ± 0.8
12	17 ± 4	2.2 ± 1.1
18	20 ± 5	0.4 ± 0.1
24	14.1 ± 1.9	0.6 ± 0.2
30	11 ± 2	2.6 ± 0.3
40	13 ± 3	2.9 ± 0.9

Table 4.4. *Percentages of normalized values for early apoptotic cells analyzed by flow cytometry 2 days after MBRT (valley doses) and BB. These data are graphically represented in histograms in Figure 4.6-B.*

MBRT leads to a clear increase in the amount of pre-apoptotic cells up to a maximum reached at 12 Gy, remaining unchanged until 18 Gy. Only at higher valley doses (≥ 24 Gy) the percentage of pre-apoptotic cells decreased (Table 4.4), showing the preference of F98 cells of dying by necrosis (or late apoptosis) at those valley doses. Thus, the majority of MBRT-irradiated cells seem to die by a more slow death pathway, consuming energy, as a consequence of a better-tolerance of dose deposition, specially at valley doses ≤ than the endpoint. This preferential death mode would lead to an increased efficiency of RT, with a minimal interference in normal organisms activities (Darzynkiewicz *et al.* 1997, Zong & Thompson 2006).

Figure 4.6-C and Table 4.5 depict both the normalized percentage of cells undergoing late apoptosis and necrosis 48 h after treatments. In the case of minibeams, a stepwise increase in the number of dead cells is observed up to a valley dose of 18 Gy. Note that in this case the percentage of dead cells at 12 Gy is almost the same ($p > 0.05$) than at 18 Gy (Table 4.5).

No significant differences ($p > 0.05$) are observed for doses ranged from 24 Gy to 40 Gy, neither among them nor in comparison with dead cells irradiated between 12 Gy and 40 Gy with BB. Hence, the percentages of cell death at higher doses seem not to significantly differ according to the radiation feature. It seems that at high doses cells would die by necrosis as a consequence of an acute damage irrespective to the prior irradiation.

Seamless and valley doses (Gy)	*% of normalized dead cells after MBRT (Mean % ± SE)*	*% of normalized dead cells after BB (Mean % ± SE)*
0	0	0
6	12.2 ± 0.8	3.4 ± 0.2
12	20 ± 2	25 ± 3
18	15.1 ± 1.0	30.0 ± 1.7
24	23.8 ± 0.8	25 ± 4
30	28.2 ± 1.2	26 ± 3
40	27 ± 2	26 ± 2

Table. 4.5. *Percentages of normalized values for dead cells, including late apoptotic and necrotic cells analyzed by flow cytometry 2 days after MBRT (valley doses) and BB. These data are graphically represented in histograms in Figure 4.6-C.*

4.3 Metabolic recovery analyzed by QBlue test

Cellular recovery, analyzed as metabolic activity of living cells, was measured following a kinetic assay by using the non-toxic QBlue test.

The first measurement was performed at the third day after treatments, when the non-irradiated cells already showed a clear higher recovery than those irradiated either with minibeams or with seamless configuration (Figure 4.7-D). Among the irradiated cells, the only significant increase ($p < 0.001$) of the metabolic activity was observed in cells irradiated with BB at 6 Gy as it is depicted in Figure 4.7-D. This larger cell recovery observed at the third day after BB irradiation was in agreement with the also higher percentage of surviving cells obtained by flow cytometry one day before.

The QBlue assay performed at the fourth day showed once more that the largest recovery ability was for those cells irradiated with BB at doses ≤ 12 Gy (Figure 4.7-E).

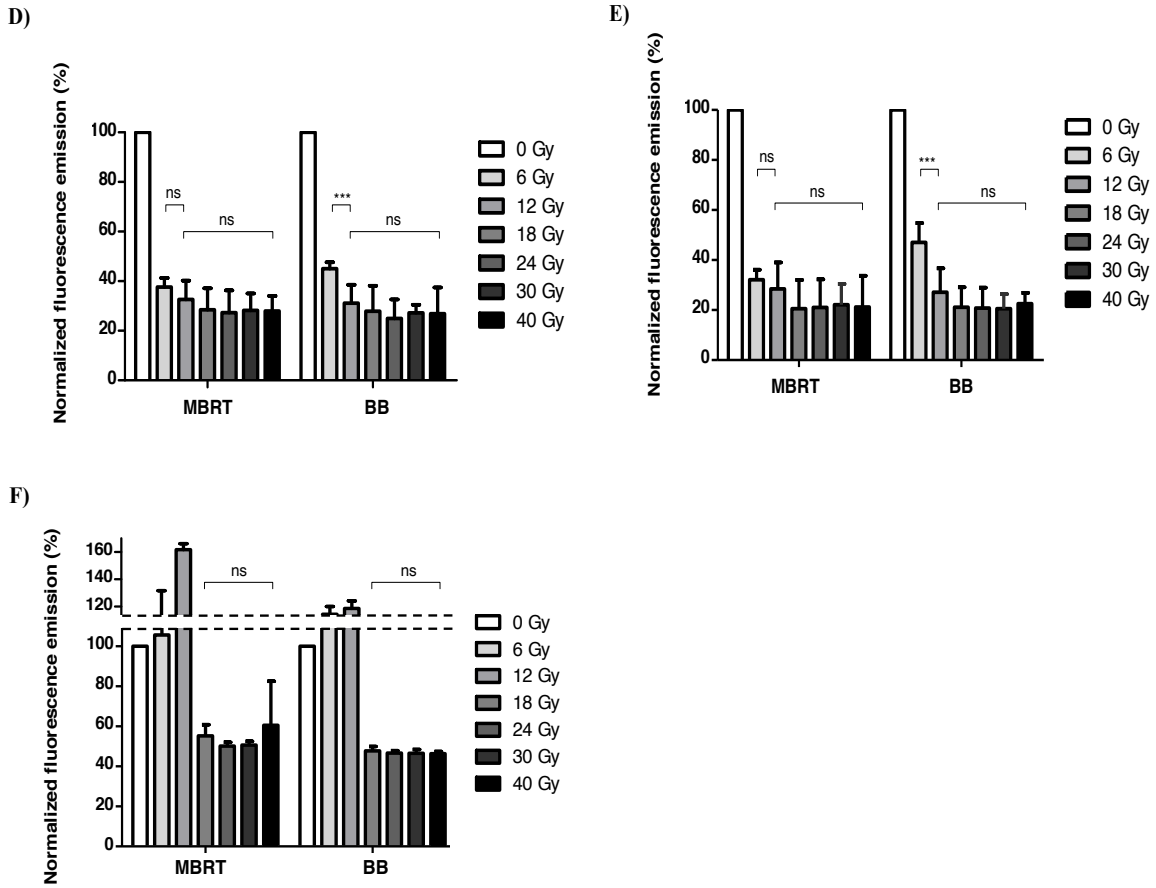

Figure 4.7. *Percentage of normalized cellular fluorescence emitted at 615 nm on D) day 3, E) day 4, and F) day 9 after MBRT and BB irradiations. Doses range from 0 to 40 Gy.*

According to Figure 4.7-E, cell recovery is larger 4 days after white BB irradiation than those observed after MBRT. Despite that, the lack of metabolic activity for doses ≥ 18 Gy for both white MBRT and BB irradiations indicates a common endpoint at around 18 Gy (see Figure 4.7-E).

This result was corroborated by the last QBlue measurement carried out on day nine, and which it is depicted in Figure 4.7-F. Moreover, in this last test, a complete cell recovery is observed for cells irradiated at doses equal or lower than 12 Gy. Under these conditions, viable cells took profit of free space between them to reach confluence, leading to arbitrary variations in the measurement of their metabolic activity.

Hence, thanks to this additional method of measuring viability, it was possible to check that for both MBRT and BB synchrotron irradiations, (valley) doses between 12 (by flow cytometry) and 18 Gy (by QBlue test) should be deposited on F98 cells to avoid their recovery with time.

Discussion

One of the main objectives of this Ph.D. work was to assess the range of effective doses for the treatment of gliomas by using an innovative RT synchrotron-based technique such as MBRT. This was one of the first times that a study concerning the biological effects of MBRT was performed *in vitro.* Therefore, it was crucial to understand the different biological responses that this new dose-deposition schedule may involve. With that aim three different aspects were investigated on F98 glioma cells: i) the nuclear damage induced on cells in terms of DSBs, ii) the percentage of different cell populations (alive, early apoptotic and late apoptotic/necrotic cells) present after irradiations, as well as iii) the recovery ability of surviving cells with time.

With the aim to better understand the effects of this spatially fractionation dose delivery, comparisons on the cellular effects were established between MBRT and white seamless SR RT.

Intensity of the γH2AX histone IF has been shown to be correlated with the radiation-induced DNA DSBs (Rogakou *et al.* 1999), reaching the maximum nuclear damage few minutes after cell exposures. Despite that, the γH2AX IF intensity had to be analyzed on F98 glioma rat cells 2 h after MBRT and BB irradiations. The reason was that all irradiations were performed before beginning the analyses to investigate the production of DSBs in function of the synchrotron technique. However, at 2 h, up to a 90% of cells exhibited γH2AX IF signal after both MBRT and BB irradiations.

The assessment of DSBs by means of γH2AX IF signal on glioma rat cells was performed by flow cytometry due to its several times higher sensitivity, lower-time consuming, and its advantages in the analysis of larger number of cells compared with other methods such as Western blot, gel electrophoresis and comet assay (Huang *et al.* 2005).

Almost the same number of damaged cells was observed after both irradiation modes. This fact seems justified since in both cases all seeded cells resulted irradiated, although the dose distribution differs according to the kind of exposure. Indeed, a greater amount of DSBs within cells could be detected 2 h after MBRT as expected. This large number of DNA DSBs analyzed in minibeam-irradiated cells may be a consequence of both the high dose deposited along the minibeam's paths and the presence of those more moderate doses in the beam penumbras. In addition, since 2 h is an insufficient time for cells to complete their cell cycle, the majority of damaged cells were accumulated in G_1 phase rather than in G_2 phase.

After irradiations, the maximum damage was expected to decrease with time (Van Veelen *et al.* 2005, Kataoka *et al.* 2006), and the percentage of remaining cellular foci analyzed after irradiations can be associated with those unrepaired lethal lesions. This correlation, however, seems to be valid only under the following conditions:

i) At low level of damage, i.e., when there is a lack of saturation of the enzymes involved in histone dephosphorylation (Zhou *et al.* 1998, Banáth *et al.* 2004, Costes *et al.* 2006, Marková *et al.* 2007).

ii) When the analysis is peformed at the time corresponding approximately to the cell-doubling time (Marková *et al.* 2007, Mah *et al.* 2011).

Since F98 cell-doubling time has been reported to be less that 20 h (Menichetti *et al.* 2009, Olivier *et al.* 2009), γH2AX IF was analyzed 17 h after irradiations up to doses as high as 24 Gy. At around cell-doubling time after MBRT and BB, a pronounced G_2-phase arrest was detected in many cells, but only after MBRT an increasing number of damaged cells was observed to be arrested in G_1 phase. The higher the valley dose, the higher the proportion of cells arrested. This effect, explained by the larger damage induced by MBRT compared to BB, was also observed by Jane & Pollack (2010) in experiments with human glioma cells.

In addition, a higher number of remaining foci was detected on cells irradiated with MBRT compared with BB at this time. Some of these unrepaired or misrepaired arrested cells which contain a gross injury will be inactivated probably via necrosis just after the completion of the cell cycle (Darzynkiewicz *et al.* 1997, Olive & Durand 1997). On the other hand, those low and moderate-damaged cells containing misrepaired foci will undergo a delayed apoptotic death (Olive & Durand 1997). These kind of damaged cells more prone for apoptosis could only be found after MBRT irradiations. The spatially fractionated dose of MBRT may favor that those cells placed both at valley and at penumbra regions die by apoptosis. The reason would be the moderate doses that they received there, specially at or slightly above the endpoint. In fact, in line with this, Dilmanian *et al.* (2007) observed that cells died mainly by apoptosis 6 h after MRT irradiations at 24 Gy peak doses. The experiment was performed with a non-tumoral cell line, and apoptotic cells, even in the peak regions, at moderate dose irradiations were detected.

The high percentage of cells undergoing apoptosis after MBRT in comparison with white BB would be thus a consequence of the moderate- and long-term maintenance of damage, and therefore, a higher defective DNA-repair can be observed 17 h after MBRT. This mainly occurred when the valley dose was equal or sensibly higher than the endpoint. The endpoint is

considered as the threshold dose from which a significant enhancement in the effectiveness of both radiation treatments is achieved. This enhancement can be analyzed either in terms of percentage of surviving cells, or according to the nuclear damage induced on cells. Regardless of the analysis, the endpoint was established at around 12 Gy for both irradiation modalities. The common endpoint found for MBRT and BB confirm the significance of using the valley dose as reference. Oppositely, cells placed at the beam paths in MBRT were expected to die by necrosis due to the excess of damage.

The increased proportion of apoptotic cells after MBRT irradiations would have some biological implications such as:

- Cells dying by apoptosis are quietly removed by phagocytic cells with minimal interference in normal organisms activities (Zong & Thompson 2006). In addition, apoptotic dying cells exhibit PS on the cell surface which ensures the efficient removal of such cells from the medium (Zong & Thompson 2006), with a lower toxicity to the patient (Darzynkiewicz *et al.* 1997).

- Unlikely necrosis, apoptosis does not involve any inflammatory response to alert the organism of the need to defend itself against the insult (Darzynkiewicz *et al.* 1997, Zong & Thompson 2006).

- Apoptotic death pathway does not result in scar formation (Darzynkiewicz *et al.* 1997).

Results based on temporarily beam fractionation seem to be coherent with the findings that moderate- and long-term maintenance damaged cells, such as those obtained after MBRT radiation are more prone for apoptosis rather than necrosis. For instance, Meyn *et al.* (1994) concluded from their results that after each fraction of radiation, an apoptosis-sensitive subpopulation of ovarian tumor model cells re-emergenced, and the percentage of apoptotic cells after a second fraction increased. Likely, Ling *et al.* (1995) observed that the split of a radiation dose into 2 equal fractions induced more apoptosis than the same dose given as a single fraction did.

In this case, these cells with misrepaired and unrepaired DSBs might either remain arrested, or be able to undergo few more times through the cell cycle before accumulating higher amount of nuclear aberrations and instabilities (Seymour *et al.* 1986, Olive & Durand 1997, Roos & Kaina 2006, Belyaev 2010). In contrast, due to the features of BB irradiations, cells would only have

two options depending on their nuclear damage 17 h after exposures: either repair it (for doses ≤ endpoint) or undergo necrosis if the damage was too large (for doses > endpoint).

In order to assess the effectiveness on tumor cells of both, MBRT and BB irradiations, other biophysical aspects such as the recovery ability with time have also to be considered. For this purpose, a complementary technique to flow cytometry was used. It allowed to measure the recovery of the remaining living cells after each irradiation. In contrast to others such as the (3-(4,5-dimethylthiazol-2-yl)-2,5-diphenyltetrazolium bromide (MTT), QBlue test provides an adequate estimation of cell proliferation, keeping the cells alive. In this way, a kinetic study can be performed. In addition, Alamar QBlue is more sensitive than MTT (O'Brien *et al.* 2000).

The results from that technique pointed at around 18 Gy as the endpoint for MBRT and BB. This endpoint corresponds to the dose from which there was not observed any cell recovery with time. This new threshold obtained by the QBlue tests is higher than those assessed before by the two flow cytometric techniques, where cell recovery was not taken into account for so long. In spite of this common endpoint, the cell recovery is larger 4 days after white BB irradiation than after MBRT. This evidence could be explained by the higher global amount of dead cells with MBRT technique, which favors a slower removal of dead cells from the medium.

Our findings are coherent with those obtained by Sarun *et al.* (paper in preparation) who encountered that the valley dose threshold to detect any cell recovery after MBRT irradiations was around 20 Gy for a more radioresistant cell line (9L). Those 20 Gy agree with that found at around 18 Gy for the more radiosensitive F98 cell line (Barth 1998).

5 Chemo-radiotherapy with concomitant cisPt

The idea of those experiments was to combine the administration of cisPt with white synchrotron radiation in order to improve the outcome of those RT techniques. This drug has not been routinely used in treatments against gliomas. However, the higher effectiveness obtained in *in vivo* experiments with cisPt and monochromatic irradiations at the ESRF (Biston *et al.* 2004) paves the way of further investigations of its effects on glioma cells. In particular, it was though that the combination of this drug with white MBRT irradiations could allow to increase the therapeutic index of gliomas.

First *in vitro* experiments performed at the ESRF showed that cisPt should be at least 1 μM for 12 h to see some effect on nuclear damage after monochromatic irradiation (Corde *et al.* 2002). Subsequent experiments performed by Biston *et al.* (2004) used cisPt at concentrations of 30 μM incubated on F98 cells for 6 h. However, the concentration of cisPt in the experiments described in this thesis was reduced with respect to those used in the aforementioned published works in order to minimize the toxicity in healthy cells. Even thought, cisPt at a concentration of 7 μM still showed a higher toxicity on cells by itself, which hid any concomitant effect with a posterior irradiation. It was for this reason, that new strategies such as its combination with AuNPs (section 6) or its association to liposomes (section 7) must be investigated in order to decrease the cytotoxicity of cisPt whilst keeping its higher effectiveness.

After optimization of all cisPt parameters, this drug was combined with white MBRT SR in an attempt of improving its outcomes (section 5.2).

5.1 Optimization of cisPt incubation time and concentration

As it was already pointed in section 1.4, treatments with crosslinking agents such as cisPt generate DNA intrastrand, and to a lesser degree interstrand crosslinks, but in any case DSBs as a primary lesions (Huang *et al.* 2004, Revet *et al.* 2011). In fact, the generation of DSBs is a consequence of the nucleotide excision repair (NER) process, which is the major pathway for the removal of cisPt-DNA adducts in cells (Jamieson & Lippard 1999, Huang *et al.* 2004, Wang & Lippard 2005). Therefore, the measurement of γH2AX IF of cells treated with cisPt permits to assess the repair ratio of those cells, and indirectly the previous damage induced on their DNA by the drug.

5.1.1 Evaluation of the influence of cisPt incubation time on DNA damage by γH2AX IF

Evaluation of the percentage of γH2AX as a function of cisPt incubation time was assessed in cells treated with this drug at two different concentrations; 3 and 7 μM. The results show that the highest percentage of cells containing γH2AX, and thus DSBs, are obtained with treatments based on cisPt 7 μM (see Figure 5.1). As it is also depicted in Figure 5.1, this occurs regardless of the cisPt incubation time. The effectiveness of both 3 and 7 μM cisPt treatments remain low and invariable for drug incubation periods ranging from 3 to 5 h. Indeed, the first significant increase ($p < 0.01$) in the percentage of damaged cells is observed for times above 8 hours (Figure 5.1).

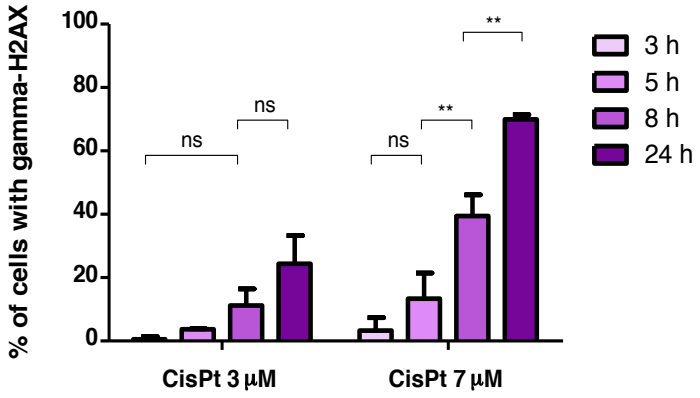

Figure 5.1. *Percentage (%) of cells with γH2AX versus cisPt concentrations (3 or 7 μM) and incubation time (3, 5, 8 or 24 h).*

From that time, whereas the effectiveness of cisPt 3 μM does not differ significantly ($p > 0.05$) between 8 h (11% ± 5) and 24 h (24% ± 9), cisPt 7 μM achieves the largest proportion of damaged cells after 24 h of incubation (69.9% ± 1.5).

Thus, a higher effectiveness related to the amount of damaged cells is achieved with a cisPt concentration of 7 μM. Moreover, this result is also justified by analyzing the amount of γH2AX per cell (see Figure 5.2), which is indeed correlated with the frequency of NER pathway.

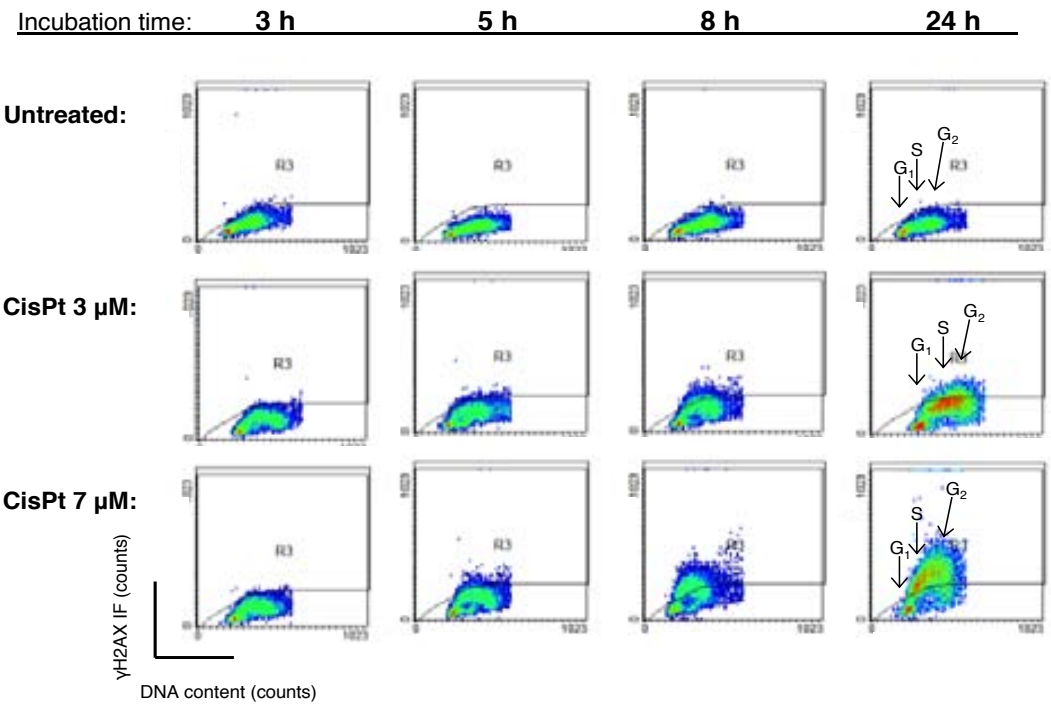

Figure 5.2. *γH2AX IF Intensity versus counts of DNA content for untreated cells, as well as for each cisPt treatment (3 or 7 µM) according to the incubation time (3, 5, 8 or 24 h). Note that the three G_1, S and G_2 phases of the cell cycle are depicted for the last samples. Although the experiment was performed by triplicate, only the result of one series is shown.*

Only for times above the 8 h the intensity of positive γH2AX IF cells is relevant as it is depicted in Figure 5.2. However, very low differences regarding the amount of nuclear damage within cells are detected when cisPt 3 µM is incubated either for 8 h or 24 h. At those times, little intensities of γH2AX IF per cell are reported. Oppositely, significant higher intensities of γH2AX IF in positive cells are measured after treatment with cisPt 7 µM incubated for 24 h (see Figure 5.2).

Moreover, that kind of analysis enables to correlate the DNA DSBs with cell cycle phase. By increasing the incubation time from 3 to 24 h for both cisPt concentrations, the amount of cells arrested in both S and G_2 phases also increases (Figure 5.2). This is due to the fact that an increasing proportion of cells are resulting damaged at increasing times.

In particular, the treatment based on cisPt 7 µM for 24 h exhibits the maximum proportion of damaged cells arrested mainly in G_2 phase. This fact is a consequence of their damage-related unability to progress through the cell cycle, which avoids its entrance to the mitotic phase.

Thus, this chemotherapeutic protocol based on cisPt 7 μM incubated for 24 h seems to be the most effective due to: i) the increase in the percentage of damaged cells, arrested mainly in G_2, which are trying to repair their DNA adducts, and ii) the largest amount of γH2AX IF intensity per cell, as a consequence of a larger nuclear damage.

5.1.2 Evaluation of cell recovery after cisPt incubation by γH2AX IF and QBlue test

For this investigation, two groups of cells loaded with cisPt (3 and 7 μM) were incubated for a fixed time of 24 h. This incubation time was established to be the optimal one of those studied due to the high effectiveness of cell damaging (see section 5.1.1). After that time, cisPt was removed from the medium, and measurements of the γH2AX IF intensity were performed at 30 min, 2, 6 or 24 h in order to study the evolution of induced-damage with time.

The amount of γH2AX per cell is correlated with the proportion of cisPt-DNA adducts that are tried to be removed. The first results depicted in Figure 5.3 report the percentage of cells exhibiting DSBs after treatments, as a consequence of the repair process via NER.

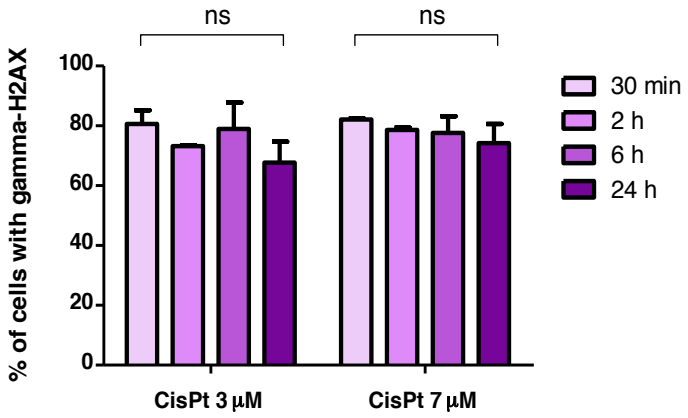

Figure 5.3. *Percentage (%) of cells with γH2AX versus cisPt concentrations (3 or 7 μM) and post-incubation time (30 min, 2 , 6 or 24 h).*

No differences ($p > 0.05$) could be detected neither in the percentage of damaged cells undergoing repair nor in the several cisPt post-incubation times between both cisPt concentrations. In fact, the mean % ± SD of cells with γH2AX from 30 min to 24 h after cisPt 3 μM incubations is 75 ± 6, whereas for cisPt 7 μM is 78 ± 3.

Different untreated cells (controls) were used now in parallel to each cisPt concentration experiment, as it can be seen in Figure 5.4.

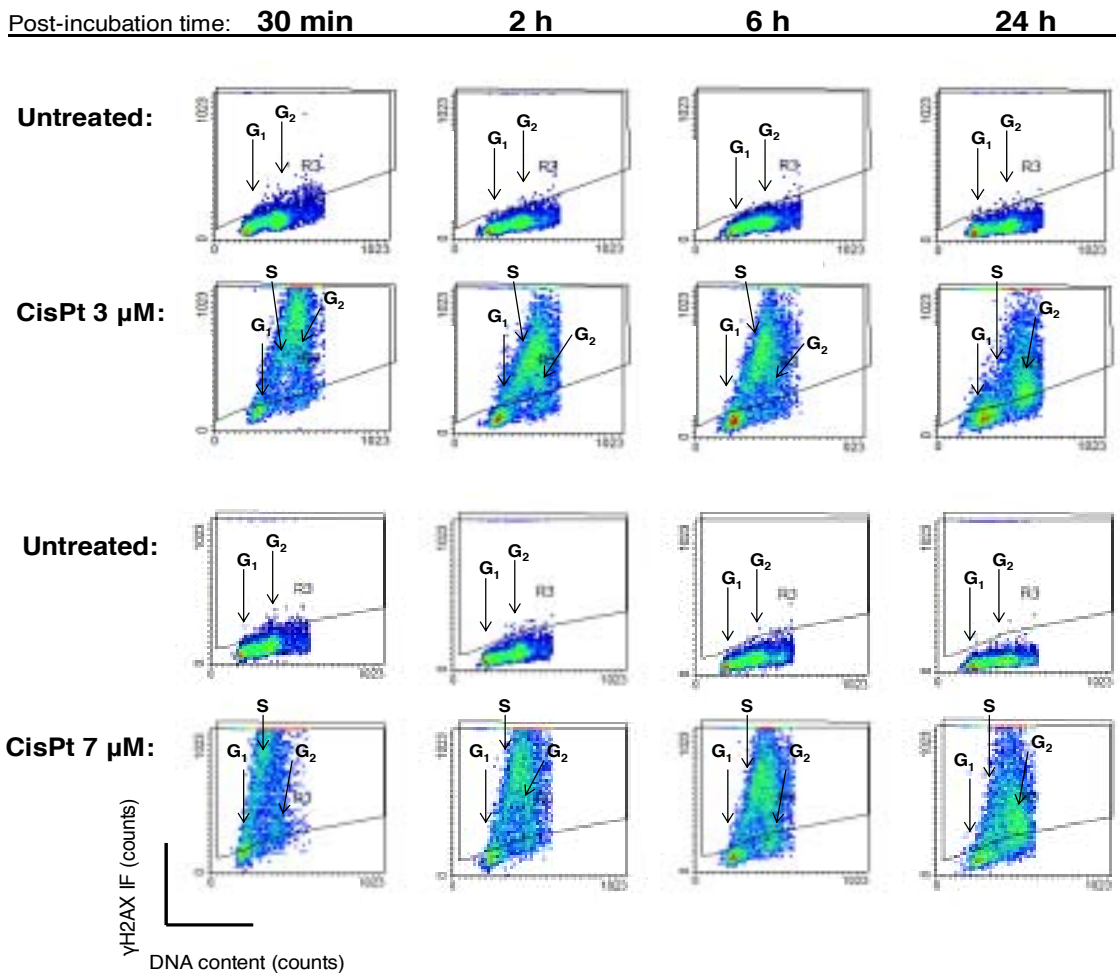

Figure 5.4. *γH2AX IF intensity versus counts of DNA content for untreated cells and its corresponent cisPt treatment (3 or 7 µM) according to the post-incubation time (30 min, 2, 6 or 24 h). Although the experiment was performed by triplicate, only the result of one series is shown for each cisPt concentration.*

Higher γH2AX IF signal intensities have been reported in this case (Figure 5.4), in comparison with results showed before (Figure 5.2) regarding the time of incubation. This fact indicates that cellular reparation really begins once cisPt has been removed from the medium, allowing NER pathway to be effective.

In the present case, much smaller differences in the cellular γH2AX IF intensity can be detected between cisPt 3 and 7 µM. For both cisPt concentrations, the γH2AX IF intensity of cells

arrested in S phase of the cell cycle decreases with increasing times after treatments up to 24 h. Moreover, 24 h after cisPt incubations almost all positive γH2AX IF cells appear arrested in G_2. However, the main difference between them relies on the slightly large frequency of DSBs in cells treated with cisPt 7 μM (see Figure 5.4 depicted above). This higher γH2AX IF intensity detected in those cells is a consequence of the larger amount of DNA adducts induced per nucleus by cisPt 7 μM.

In order to corroborate these results, measurements of the cell metabolic activity were performed by using the QBlue assay in parallel. With the purpose of leaving enough time to cells to activate its metabolism, the first measurement was performed 6 h after cisPt incubations. Extra metabolic assays were carried out 24 h and 50 h after treatments.

As it is depicted in Figure 5.5, cells pre-treated with cisPt 7 μM presented a lower metabolic activity in comparison with cisPt 3 μM. This is indeed correlated with a little recovery ability as a consequence of the larger nuclear damage induced by cisPt 7 μM.

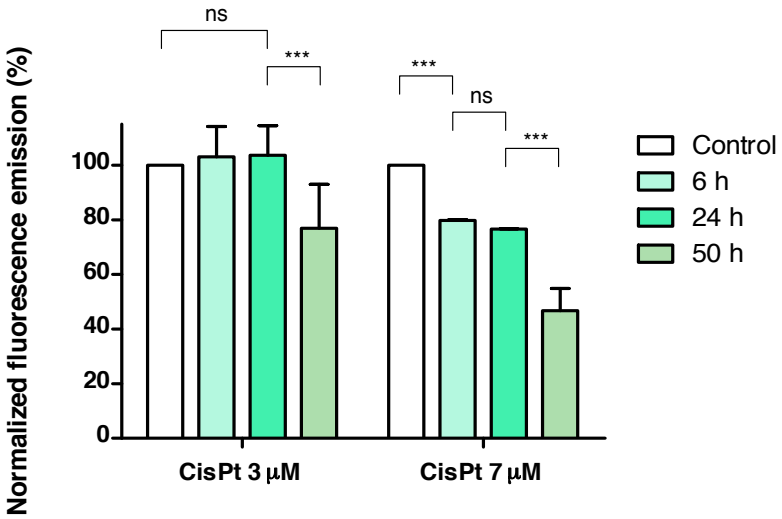

Figure 5.5. *Normalized QBlue fluorescence emission (%) at 615 nm in function of both cisPt concentration (3 or 7 μM) and post-incubation time (6, 24 or 50 h).*

A 100% of cell recovery is feasible up to 24 h after cisPt 3 μM. In the case of cisPt 7 μM, the maximal cell recovery is detected during the first 24 h as well, although the normalized percentage of fluorescence emission is lower (76.6% ± 0.1) than for cisPt 3 μM. In particular, the lowest metabolic activity is measured 50 h after cell treatment with cisPt 7 μM (47% ± 8).

Therefore, the protocol of chemotherapy based on cisPt 7 μM for 24 h seems to be again the most effective treatment in two ways: i) by leading to a slightly larger γH2AX IF intensity per cell up to 24 h after treatment (see Figure 5.4), as a consequence of a larger damage (adducts) in cells, and consequently ii) inducing the lowest cell recovery with time, according to the QBlue test.

5.2 Comparison of effectiveness of white MBRT and BB synchrotron radiations combined with concomitant cisPt administration

To further enhance the effectiveness of white MBRT and BB, new combinations of chemo- and radiotherapy were investigated. To that end, cells were pre-treated with cisPt 7 μM for 24 h before to expose them to MBRT and BB irradiations.

Cells irradiated with MBRT and BB exhibited a common endpoint at (valley) doses ≤ 12 Gy, as aforementioned in section 4. Since the use of concomitant cisPt 7 μM is expected to decrease the endpoint of both white beam radiations, only (valley) doses ≤ 12 Gy were considered.

The doses in MBRT and BB are reported in Tables 4.1 and 4.2 respectively. The results are presented hereafter.

5.2.1 Assessment of γH2AX IF on the cellular DNA 2 h after irradiations

In the presence of cisPt, yields of RT-induced DSBs analyzed on cells are expected to be larger due to the concomitant effects of cisPt molecules bound to DNA (Biston *et al.* 2004).

- Assessment of γH2AX IF in F98 glioma rat cells pre-treated with cisPt 7 μM, 2 h after MBRT and BB irradiations:

Figures 5.6 and 5.7 show both that treatment with cisPt 7 μM incubated for 24 h prior irradiations leads to a larger percentage of cells exhibiting γH2AX IF signal in comparison with radiation alone.

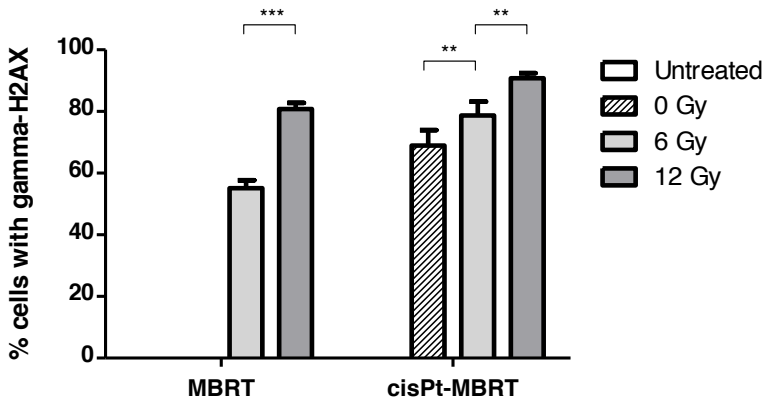

Figure 5.6. *Percentage (%) of cells with γH2AX 2 h after MBRT and cisPt-MBRT, up to 12 Gy of valley dose.*

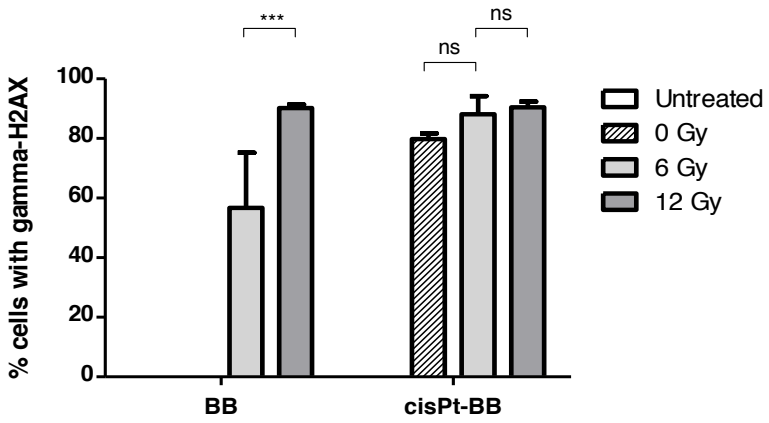

Figure 5.7. *Percentage (%) of cells with γH2AX 2 h after BB and cisPt-BB, up to 12 Gy.*

In particular, 6 Gy offers the largest difference between treatments consisting of radiation alone or RT with cisPt administration; the percentage of γH2AX positive cells after both MBRT and BB white irradiations at 6 Gy was about 60%, while the percentage of cells with nuclear foci reaches 80% approximately (Figure 5.6 and 5.7) when cisPt 7 μM is used. Thus, the percentage of damaged cells increases a ~ 20% with a concomitant treatment of cisPt 7 μM for 24 h prior irradiations at 6 Gy of (valley) dose.

This suggests an increase of effectiveness for (valley) doses around 6 Gy for both MBRT and BB white irradiations in presence of cisPt, oppositely to 12 Gy found for treatments based on MBRT or BB exposures without cisPt (see Figures 5.6 and 5.7). Despite this fact, very little differences in the percentage of cells with DNA DSBs can be observed between cisPt alone (0 Gy) and cisPt-RT, specially at 6 Gy.

However, cisPt treatments with a posterior MBRT irradiation at 12 Gy showed an increased % of cells with DSBs.

The number of cells exhibiting γH2AX foci does not differ much between both cisPt-MBRT and cisPt-BB irradiation modes. Nevertheless, the γH2AX IF intensity induced on cells presents different features between MBRT and BB (Figure 5.8).

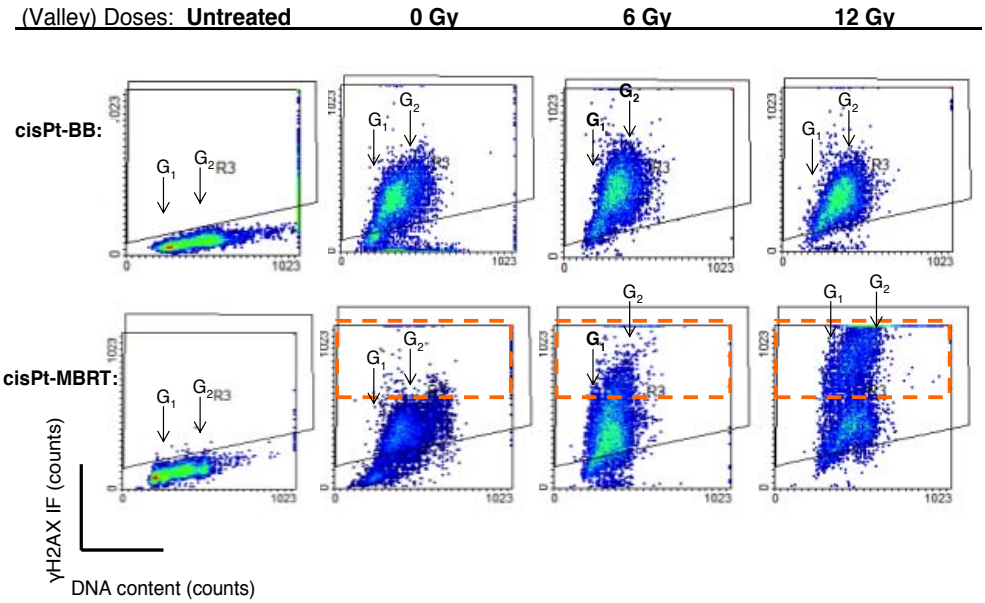

Figure 5.8. *Counts of γH2AX IF versus cellular DNA content stained with PI of F98 glioma rat cells 2 h after pre-treatment with cisPt 7 μM and irradiation with BB and MBRT at 0 (only cisPt), 6 and 12 Gy of (valley) dose respectively. The dashed squares are the same that those depicted in Figures 4.2 and 4.5.*

CisPt alone (0 Gy) shows a lower γH2AX IF intensity within cells (Figure 5.8). Moreover, note that dots in Figure 5.8 corresponding to cells treated only with cisPt 7 μM for 24 h (0 Gy) are almost identical to those depicted in section 5.1 for the same cisPt conditions (concentration and incubation time).

On the other hand, γH2AX IF intensity increases as a function of dose, being more intense in minibeam-irradiated cells (Figure 5.8). As a result, MBRT generates a higher amount of DSBs per nucleus compared with BB. Moreover, at valley doses of 6 Gy, two populations begin to be detected 2 h after MBRT exposure according to the γH2AX IF intensity. They are more clearly distinguishable at 12 Gy. The upper population, highlighted in each plot by the same dashed square that those used in Figure 4.2, corresponds to those glioma cells containing the highest proportion of DSBs per nucleus.

It is probably a consequence of those higher doses deposited by each minibeam path, i.e., the peak region, as well as by those moderate doses within the penumbras regions of minibeams (see Figure 4.3). Again, the lower population could be correlated to those γH2AX IF positive cells irradiated at the valley region. Like for MBRT and BB alone, this population with a lower γH2AX intensity resembles that detected in the BB mode when both valley and seamless doses are equal. The study of the nuclear damage according to the irradiation mode is needed since the dose deposition mode might become more relevant that the integrated dose by itself.

Both radiation modes in presence of cisPt 7 μM exhibit higher yields of DSBs frequency inside the cells nucleus (by comparing both 4.2 and 5.8 figures) than radiation alone. This increase is specially remarkable for those cells which exhibited low and moderate DSBs frequency 2 h after MBRT and BB radiations without cisPt. Moreover cisPt enables to induce DSBs by a subsequent irradiation, but in a large uniform way. This fact is demonstrated by i) the less well-defined γH2AX IF intensity regions in function of the valley and peak doses after MBRT radiations, and ii) γH2AX IF positive cells appearing as one round-shape population after BB exposures.

- Analysis of γH2AX IF intensity according to the DNA content of F98 glioma rat cells pre-treated with cisPt 7 μM, 2 h after MBRT and BB irradiations:

Regarding the DNA content, measured by nuclear labeling with PI (Figure 5.8), a larger amount of cells remain arrested in both S and G_2 phases of the cell cycle, in comparison with MBRT and BB radiation alone. This is a consequence of the prior cisPt cell incubation for 24 h. Cells arrested principally in G_2 phase are waiting for the repair of their nuclear damage before entering mitosis (Wang & Lippard 2005). Some of those cells will be repaired, whilst others will remain arrested for longer before to die mainly by apoptosis (Jamieson & Lippard 1999). However, since G_2 phase is considered as the most radiosensitive phase of the cell cycle, a subsequent irradiation of those damaged cells would lead to a clear increase of the treatment effectiveness.

5.2.2 Survival analysis assessed by flow cytometry

MBRT has shown a higher effectiveness alone and concomitanly with cisPt administration (higher γH2AX IF intensity per cell) than white BB. Therefore, flow cytometric analyses were performed 48 h hours after MBRT-based treatments in order to elucidate the proportion of surviving cells in presence or not of cisPt 7 μM.

Normalized data for unstained surviving cells (Table 5.1), and plotted in histograms in Figure 5.9-A indicate a different dose-response for both kind of MBRT treatments. A significant decrease in survival for cells pre-treated with cisPt can be detected at any valley dose.

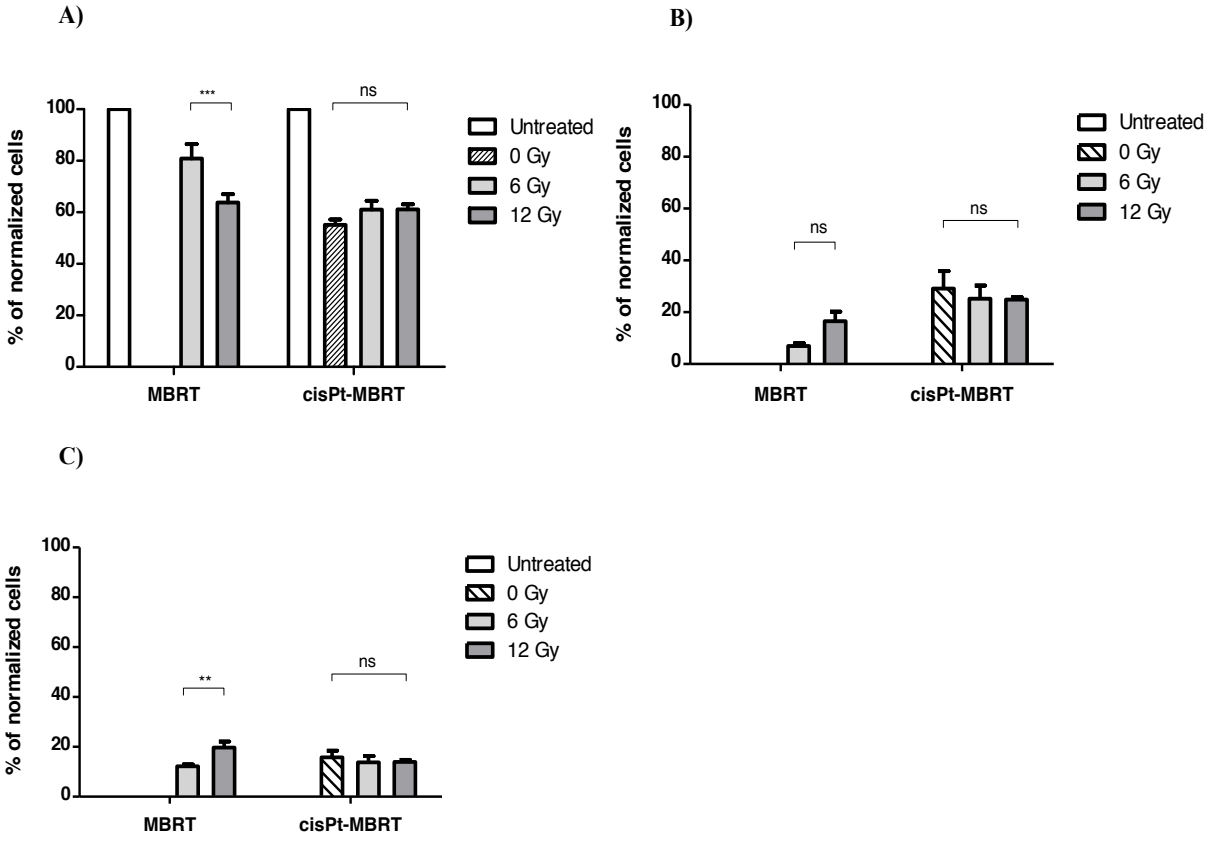

Figure 5.9. *Percentage of normalized A) living, B) early apoptotic and C) dead cells after MBRT and cisPt-MBRT treatments in a valley dose escalation ranging from 0 (only cisPt treatment) to 12 Gy. Note that the decrease of cell survival was around of 20% for valley doses above 6 Gy with MBRT, and at any dose for treatments based on cisPt-MBRT.*

In particular, the dose from which cisPt-MBRT seems to exhibit an increase of effectiveness can be established at around 6 Gy (Table 5.1), unlikely MBRT alone, which was established at 12 Gy approximately. In fact, according to the values of Table 5.1, the percentage of living cells

after cisPt 7 μM followed by MBRT exposure at 6 Gy (61%) is the same that those surviving after a direct MBRT radiation at 12 Gy (64%). This is to say that a pre-treatment of tumor cells with cisPt 7 μM allows to decrease the (valley) dose of RT from 12 to 6 Gy. Therefore, that leads to assess a higher effectiveness of concomitant treatments against F98 tumor cells, as it was also pointed out previously by the assessment of DSBs.

Nevertheless, the effectiveness of cisPt 7 μM is already high without any concomitant irradiation (about 55% of surviving cells). Indeed, the percentage of survival for cells pre-treated with cisPt does not differ significantly from those treated with cisPt and a later irradiation (Table 5.1).

Valley doses (Gy)	*% of normalized surviving cells after MBRT (Mean % ± SE)*	*% of normalized surviving cells after cisPt-MBRT (Mean % ± SE)*
Untreated	100	100
0	-	55 ± 2
6	81 ± 6	61 ± 4
12	64 ± 3	61 ± 2

Table 5.1. *Percentages of normalized values for surviving cells analyzed by flow cytometry 2 days after MBRT and cisPt-MBRT. These data are graphically represented in histograms in Figure 5.9-A.*

Irradiation of cells loaded with cisPt with MBRT allows to increase the percentage of early apoptotic cells, as it is depicted below in Table 5.2.

Valley doses (Gy)	*% of normalized early apoptotic cells after MBRT (Mean % ± SE)*	*% of normalized early apoptotic cells after cisPt-MBRT (Mean % ± SE)*
Untreated	0	0
0	-	29 ± 7
6	7.0 ± 1.0	25 ± 5
12	17 ± 4	24.9 ± 0.9

Table 5.2. *Percentages of normalized values for early apoptotic cells analyzed by flow cytometry 2 days after MBRT and cisPt-MBRT. These data are graphically represented in histograms in Figure 5.9-B.*

CisPt leads thus to a clear increase in the number of early apoptotic cells. As a consequence, those dead cells will be removed more efficiently, with none inflammatory response, and with the rest of tissue functions undisturbed (Darzynkiewicz *et al.* 1997, Zong & Thompson 2006). Nevertheless, no differences in the percentage of early apoptotic cells can be observed between cisPt alone and cisPt-MBRT, neither at 6 nor 12 Gy.

Figure 5.9-C and Table 5.3 depict both the normalized percentage of cells undergoing late apoptosis and necrosis 48 h after treatments. For the treatment based on cisPt administration concomitantly to MBRT exposures ~ 10% less of necrotic dead cells can be detected in comparison with early apoptotic cells (depicted in Table 5.2). No differences are observed in the percentage of dead cells between cisPt alone and cisPt-MBRT at any dose, showing the higher cytotoxicity of cisPt by itself.

Valley doses (Gy)	*% of normalized dead cells after MBRT (Mean % ± SE)*	*% of normalized dead cells after cisPt-MBRT (Mean % ± SE)*
Untreated	0	0
0	-	16 ± 3
6	12.2 ± 0.8	14 ± 2
12	20 ± 2	14.0 ± 0.8

Table. 5.3. *Percentages of normalized values for dead cells, including late apoptotic and necrotic cells analyzed by flow cytometry 2 days after MBRT and cisPt-MBRT. These data are graphically represented in histograms in Figure 5.9-C.*

Moreover, the percentage of dead cells is practically the same after both MBRT treatments, despite the presence or not of cisPt (Table 5.3). However, the presence of cisPt lets to increase the effectiveness of treatments by increasing the ratio of early apoptotic cells.

Discussion

First experiments *in vitro* at the ESRF showed that cisPt should be at least 1 μM for 12 h to see some effect on nuclear damage after monochromatic irradiation (Corde *et al.* 2002). Subsequent experiments performed by Biston *et al.* used cisPt at concentrations of 3 μM and 30 μM both for 6 h, in order to analyze the DSBs produced with later radiation exposures (Biston *et al.* 2004).

The concentration of cisPt of the experiments performed in this Ph.D. work was however reduced with respect to those used in the aforementioned published works in order to minimize the toxicity in healthy cells. The idea was to compensate this decrease by combining the cisPt administration with a concomitant irradiation. To that end, a prior optimization of the cisPt parameters was required. This was performed by measuring the γH2AX IF intensity emitted per cell as a consequence of DSBs generated during their NER repair process. The higher the γH2AX IF intensity is, the higher the amount of DNA adducts that are being removed by NER pathway is.

NER is in fact the major pathway for the removal of cisPt-DNA adducts *in vivo* and *in vitro*, which is known to generate SSBs and DSBs for the further rejoining (Jamieson & Lippard 1999, Huang *et al.* 2004, Wang & Lippard 2005). The kinetics of development of γH2AX foci are very different for chemicals than for ionizing radiation. For instance, for drugs such as cisPt, foci may develop only when cells with DNA crosslink enter replicative phase, i.e., S phase of the cell cycle (Olive 2011). This would explain the significant increase of cells exhibiting DSBs preferentially in S phase of the cell cycle for cisPt incubation times ≥ 8 h. In particular, this gain is larger for cisPt 7 μM, which induces to a higher amount of cisPt-DNA adducts in comparison with cisPt at 3 μM. Moreover, with cisPt 7 μM incubated for 24 h there was evidence of cell cycle-phase specificity in the increase of γH2AX IF. Cells remained arrested principally in G_2 phase, waiting for the repair of their nuclear damage before entering mitosis (Wang & Lippard 2005). Some of those cells will be repaired, whilst others will remain arrested for longer before to die mainly by apoptosis (Jamieson & Lippard 1999). However, since G_2 phase is considered as the most radiosensitive phase of the cell cycle, a subsequent irradiation of those damaged cells would lead to a clear increase of the treatment effectiveness.

Thus, according to the results, the optimal time to perform irradiations would be 24 h after incubations with cisPt 7 μM. This is because of the larger proportion of cells that remain arrested in G_2 with respect to cisPt 7 μM incubated for 8 h and cisPt 3 μM incubated for 24 h.

Moreover, the subsequent irradiation of those Pt-loaded cells may allow to the production of additional DSBs since its main repair by NHEJ would be inhibited (Corde *et al.* 2003, Biston *et al.* 2004, 2009).

Following these results, experiments concerning the cell recovery after cisPt incubation were performed. In this case, cisPt incubation time was fixed at 24 h for both concentrations. CisPt needs to be removed from the medium to obtain the largest cell repair ratios, i.e., a higher γH2AX IF signal intensity per cell in comparison with the experiment described in section 5.1.1.

Despite no differences in the percentage of positive γH2AX cells were observed between both cisPt concentrations regardless of the post-incubation time, the impact of both treatments on cells was not the same:

1) 24 h after treatment with cisPt 7 μM, cells presented a slightly large frequency of DSBs (γH2AX IF intensity) mainly in G_2 phase. This would be a consequence of the larger number of DNA adducts induced by cisPt 7 μM with respect to the 3 μM solution.

   The absence of cells arrested in G_1 phase is consequent with the fact that cisPt-DNA adducts are removed from cells late in S or G_2 phases. This leads to a larger percentage of cells arrested in G_2 to prevent them from entering mitosis (Wang & Lippard 2005, Bencokova *et al.* 2007). Moreover, like ionizing radiation, retention of DSBs is correlated with the lack of adequate repair of DNA adducts (Olive 2011). Since cisPt 7 μM has shown the highest levels of γH2AX per cell (DNA adducts) 24 h after treatments, with the consequent lowest metabolic cell recovery, it is expected to induce also the largest proportion of cell dead.

2) QBlue measurements showed that cell recovery was higher with cisPt 3 μM, as a result of the lower proportion of DNA damage.

   Oppositely, a lower metabolic activity, and thus, a lower cell recovery were detected in cells treated with cisPt 7 μM. The reason could be the largest amount of adducts induced by those treatments (see point 1).

According to those data, the proportion of cells recovered after cisPt 3 μM would be compensated by those dead cells as a consequence of cisPt 7 μM treatment. Therefore, that fact could explain the absence of differences detected on the percentage of cells with γH2AX between both cisPt treatments.

A concomitant effect could be obtained if those cells pre-treated with cisPt 7 μM for 24 h were irradiated in a second phase. In particular, loaded-cell irradiations should be performed just after removing the cisPt from the medium, when the ratio of DNA repair is still low (see Figure 5.2) in comparison with larger times (see Figure 5.4). Moreover, the arrest of cells in the most radiosensitive phase of the cell cycle, i.e., in G_2 seems to be enhanced.

Thus, these findings together with the results obtained by Biston *et al.* (2004) demonstrating the potential use of cisPt concomitantly with radiation led to arise one question: could cisPt improve the outcome of other synchrotron-based radiation techniques? To that end, *in vitro* experiments based on MBRT and BB irradiations were performed at the ESRF.

As it has been explained in section 4.2, both MBRT and BB exhibited around 64% and 73% respectively of surviving cells 48 h after irradiations, with a common endpoint established at (valley) doses ≤ 12 Gy. The idea was thus to combine both synchrotron irradiations with cisPt administration in a concomitant way to increase the effectiveness of glioma treatments.

In fact, an increase of effectiveness for both SR techniques was obtained at ~ 6 Gy. As expected, the amount of DSBs per cell was higher for cells irradiated in presence of cisPt. In particular, since the γH2AX IF intensity was higher with MBRT with respect to BB, in presence of cisPt 7 μM, a flow cytometric analysis after cisPt-MBRT was performed to better investigate its effects. The results showed a lower proportion of living cells in presence of cisPt, as well as an increase of early apoptotic cells. Since cisPt presents G_2 specificity in the increase of arrested cells, this G_2-phase cells irradiated later with doses around the endpoint are expected to be more prone for apoptosis (Löbrich *et al.* 2010).

Therefore, cisPt leads to decrease the ratio of living cells in comparison with MBRT alone. In fact, the percentage of living cells after cisPt 7 μM followed by MBRT exposure at 6 Gy is the same that those surviving after a direct MBRT radiation at 12 Gy (see Table 5.1).

Moreover, the subsequent irradiation of those Pt-loaded cells may allow to increase the number of unrepaired and misrepaired DSBs, since cisPt adducts inhibit the major cell repair pathway, i.e., NHEJ (Corde *et al.* 2003, Biston *et al.* 2004, 2009). In this frame, analysis of DSBs 17 h

after treatments would have provided a higher γH2AX IF signal intensity within cells pre-treated with cisPt prior MBRT irradiations in comparison to those cells irradiated directly.

Despite those advantages of this drug over radiation alone, cisPt shows a higher toxicity by itself. The demonstration for that, which it has already been reported by other authors such as Adam *et al.* (2008) is given by the fact that the effectiveness of cisPt alone does not differ from the effectiveness of cisPt followed by MBRT exposures. Therefore, other alternatives should be investigated in order to reduce the cytotoxicity of cisPt, like for instace decreasing its concentration, but keeping its higher effectiveness.

6 Treatments based on cisPt and cisPt combined with AuNPs followed by a concomitant monochromatic irradiation.

With the purpose of improving the outcome of cisPt-based treatments, but maintaining at the same time their higher effectiveness, cisPt was combined with AuNPs. Indeed, comparisons of the effectiveness of *in vitro* treatments based on AuNP 3.5 μM combined with cisPt 3.5 μM were performed with respect to the administration of only cisPt 7 μM. According to the previous results described in section 5.1, solutions were left incubating for 24 h.

Moreover, a possible increase in the effectiveness of cisPt-based treatments with a subsequent monochromatic irradiation of loaded cells at 81 keV was also investigated.

6.1 Comparison of cell survival assessed by flow cytometry

Results concerning the normalized percentage of living cells (Figure 6.1-A and Table 6.1) show that cisPt 7 μM without radiation leads to a lower percentage of living cells. Thus, it seems to be more effective than the combination of cisPt 3.5 μM and AuNPs 3.5 μM. This fact confirms the higher cytotoxicity of cisPt in comparison with that expected for AuNPs.

However, cells loaded with the combination of cisPt-AuNP, followed by monochromatic radiation at 81 keV show a decreased survival ($p < 0.05$) from doses of 6 Gy in comparison with those glioma cells pre-treated with cisPt alone which shows a higher effectiveness regardless of the posterior irradiation (Figure 6.1-A and Table 6.1). Therefore, the initial aim of enhancing the concomitant effects of cisPt with a subsequent irradiation is accomplished by combining lower concentrations of the drug with AuNPs.

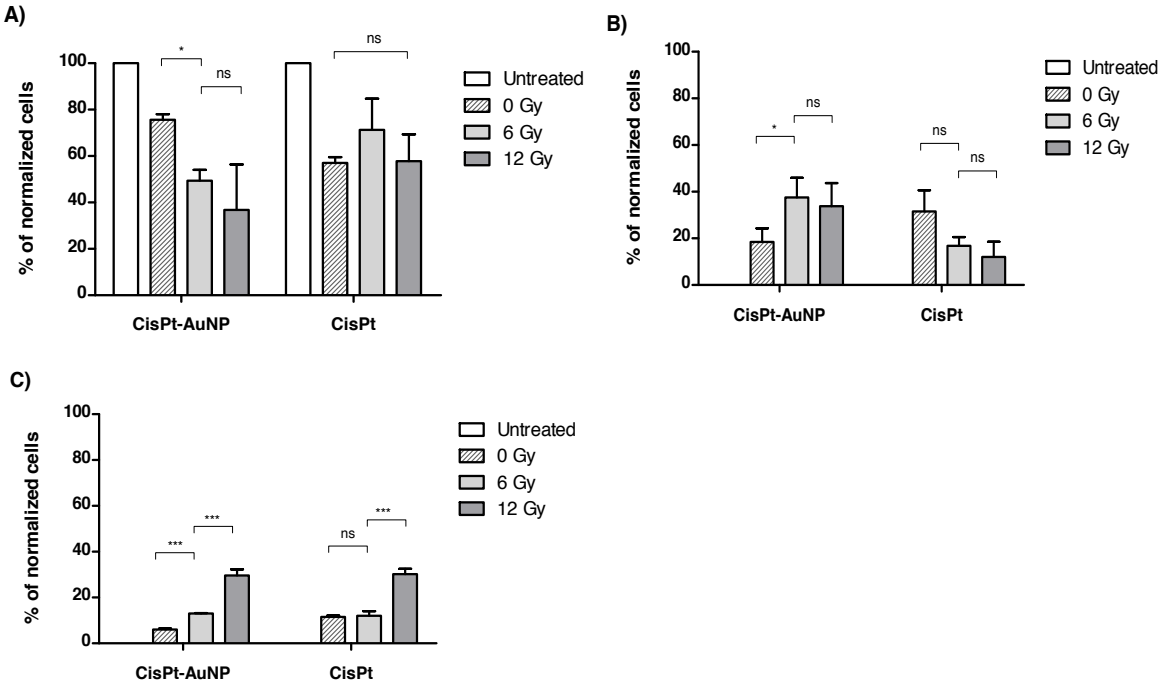

Figure 6.1. *Percentage of normalized A) living, B) early apoptotic and C) dead cells after treatment either with cisPt 3.5 µM and AuNPs 3.5 µM or cisPt 7 µM alone, concomitantly to monochromatic synchrotron radiation at 81 keV. The higher % of surviving cells after cisPt-AuNP treatment allows to confirm the lower cytotoxicity of this combination in comparison with cisPt alone.*

Doses (Gy)	*% of normalized surviving cells after AuNP-cisPt irradiations (Mean % ± SE)*	*% of normalized surviving cells after cisPt irradiations (Mean % ± SE)*
Untreated	100	100
0	76 ± 2	57 ± 2
6	49 ± 5	71 ± 14
12	37 ± 20	58 ± 12

Table 6.1. *Percentages of normalized values for surviving cells analyzed by flow cytometry 2 days after monochromatic synchrotron radiation. The % of surviving cells after AuNP-cisPt seems to be decreased. These data are graphically represented in histograms in Figure 6.1-A.*

A similar result was obtained previously from flow cytometries performed on cells treated with cisPt 7 µM and subsequently irradiated with white MBRT (see section 5.2.2).

Despite the higher toxicity of cisPt 7 μM, only the combination of both metallic compounds, i.e., cisPt-AuNP leads to a higher effectiveness after irradiations. It involves a higher percentage of cells dying, specially by apoptosis as it is reported in Table 6.2.

Doses (Gy)	*% of normalized early apoptotic cells after AuNP-cisPt irradiations (Mean % ± SE)*	*% of normalized early apoptotic cells after cisPt irradiations (Mean % ± SE)*
Untreated	0	0
0	18 ± 6	32 ± 9
6	38 ± 8	17 ± 4
12	34 ± 10	12 ± 7

Table 6.2. *Percentages of normalized values for early apoptotic cells analyzed by flow cytometry 2 days after monochromatic synchrotron radiation. These data are graphically represented in histograms in Figure 6.1-B.*

Again, cisPt 7 μM without any irradiation seems to be as effective in terms of percentage of apoptotic cells as AuNP-cisPt irradiated at 12 Gy. However, irradiation of cells treated with cisPt alone offers lower percentages of apoptosis regardless of the dose.

Incubation of cisPt alone with a later irradiation gives the same percentage of dead cells than the cisPt-AuNP-based treatment (Table 6.3). Moreover, in both cases an excess of damaged cells is achieved when drugs are incubated for 24 h and subsequently irradiated at 12 Gy.

Doses (Gy)	*% of normalized dead cells after AuNP-cisPt irradiations (Mean % ± SE)*	*% of normalized dead cells after cisPt irradiations (Mean % ± SE)*
Untreated	0	0
0	6.0 ± 0.5	11.5 ± 0.6
6	13.0 ± 0.2	12 ± 2
12	30 ± 3	30 ± 2

Table 6.3. *Percentages of normalized values for dead cells analyzed by flow cytometry 2 days after monochromatic synchrotron radiation. These data are graphically represented in histograms in Figure 6.1-C.*

Despite the same proportion of dead cells, the combination of cisPt and AuNP both at a concentration of 3.5 μM arises as the most effective treatment after a subsequent irradiation with a monochromatic beam of 81 keV at doses of 6 Gy approximately. This chemo-radiotherapeutic treatment leads to decrease the cell survival, with the consequent increase of the apoptotic cell ratio.

6.2 Study of the possible dose enhancement of cisPt alone after irradiations

In order to investigate a possible dose-enhancement effect mediated mainly by Auger electrons, the effectiveness of both cisPt-MBRT and cisPt-81 keV treatments in terms of cell killing is compared.

Despite a slightly large percentage of early apoptotic cells was detected after cisPt-MBRT in comparison with cisPt-81 keV treatment (see Figure 6.2) (perhaps as a consequence of the dose fractionation or of different dose rates between both techniques), the amount of global dead cells were practically the same regardless of the radiation mode (Figure 6.2).

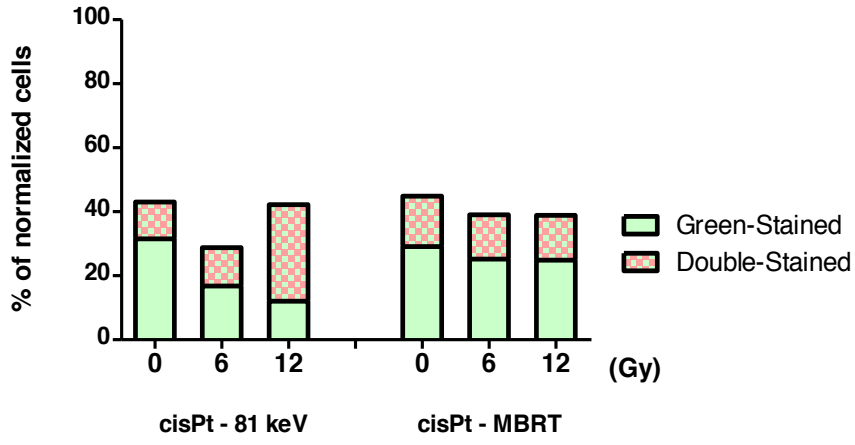

Figure 6.2. *Percentage (%) of normalized dead (double-stained) and early apoptotic (green-stained) cells according to the chemo-radiotherapeutic treatment; cisPt 7 μM for 24 h followed by 81 keV or MBRT synchrotron radiation. A dose escalation was performed from 0 (only cisPt) up to 12 Gy of (valley) dose.*

Identical effectiveness in terms of global cell death is observed for both chemo-radiotherapeutic treatments. This result could demonstrate the absence of any dose enhancement (by an extra Auger electrons deposition) at cisPt concentrations of 7 μM, since the cell lethality is the same irrespectively the energy spectrum of incident photons. These results are coherent with those ones obtained from Monte Carlo simulations and reported in Appendice 1.

Moreover, cisPt leads to reduce the dose required to obtain an improved effectiveness of treatments in terms of cell killing. Thus, the effectiveness of cisPt combined with concomitant irradiations would be explained by synergic factors.

Discussion

CisPt is one anticancer drug widely used due to its high affinity for the DNA of cells. Despite this, cisPt is expected to diffuse largely to the healthy tissues where it can lead to side effects. In the quest of a new way to improve the therapeutic ratio of cisPt-based treatments, it was thought to combine lower concentrations of this drug with lower concentrations of AuNPs. This combination has been shown a lower cytotoxicity, leading to an increased cell survival. In fact, concentrations higher than 5 mg/ml of AuNPs have been reported in preclinical trials without any toxicity effect (Hainfeld *et al.* 2004, 2006, 2010).

The decrease of cisPt concentration is expected to give a lower effectiveness of treatments, which can be compensated by adding AuNPs. The energy of 81 keV was chosen in order to optimize the cross-section of photoelectric effect for both Au (K-edge energy = 80.7 keV) and Pt (K-edge energy = 78.4 keV) atoms. Nevertheless, an increase of the effectiveness was observed only in the presence of Au atoms. Two hypothesis for that are explained hereafter:

1) The incoming energy set at 81 keV is higher than the energy corresponding to the Pt K-edge (78.4 keV). As a result, the photoelectrons emitted by Pt atoms in cisPt solutions would be released with an excess of kinetic energy, and therefore, they would deposite its energy theoretically outside the cellular nucleus.

2) AuNPs present the feature of penetrating uniformly inside the cells mainly by phagocytosis (De Jong *et al.* 2008, Casals *et al.* 2010), through the reticular endothelial system of cells. Since Au atoms are closely bound among them by forming clusters, the later irradiation of AuNPs may lead to a different dose distribution inside the cells. This would lead to a higher cell lethality.

Since in the first case, i) all those photoelectrons could have increased the amount of ROS within the medium, leading to a higher proportion of early apoptotic cells than it was really detected, and that ii) the concentratrion of both metallic compounds is too much little to produce any enhancement of cell killing by photoelectrons and Auger electrons (see Appendice 1), the increase of the effectiveness of cisPt-AuNP solution is more likely to be according to the hypothesis number 2.

The threshold dose from which a significant enhancement in terms of reduced amount of living cells was established at 6 Gy approximately for both cisPt-AuNP and cisPt chemo-radiotherapeutic treatments. However, AuNPs enabled to improve fairly the effectiveness of treatments by increasing the proportion of cells that undergo apoptosis 48 h after treatment.

The fact to observe an increased proportion of dead cells after both chemo-radiotherapeutic treatments at 12 Gy indicates that doses above the endpoint can produce an excess of cell damage that leads cells to die by other mechanisms such as necrosis. This kind of cell dead is indeed correlated with a gross cell injury because of an overdose of cytotoxic agents or X-rays exposures (Darzynkiewicz *et al.* 1997).

On the other hand, despite cisPt leads to decrease the ratio of living cells in comparison with radiation alone, in all cell populations the effectiveness of cisPt alone is equivalent to that analyzed for cisPt followed by 81 keV-irradiation. Therefore, it is difficult to differentiate between the chemotherapeutic effect of cisPt and the interaction of it with monchromatic X-rays. This result was already observed in treatments based on cisPt and MBRT exposures in section 5.2, and it is also in the frame with those obtained by Adam *et al.* (2008) and Biston *et al.* (2009) on rats bearing F98 tumors. In both experiments the mean or the median survival time (MST or MeST) of the animals did not present significant differences between treaments based on 5 µg cisPt/5 µl NaCl, and the same concentration of cisPt followed by a subsequent irradiation of 78,8 keV at doses ≤ 10 Gy (Biston *et al.* 2004, Adam *et al.* 2008). Indeed, only exposures of irrespectively 78.8 keV (Biston *et al.* 2004) or 6 MV (Rousseau *et al.* 2010) at doses of 15 Gy seem to increase *in vivo* the effects of cisPt and radiation with respect to cisPt without any posterior irradiation.

Despite all the results regarding cisPt combined with radiation point at a higher effectiveness of concomitant treatments in comparison with radiation alone, very little differences could be detected in the effectiveness of cisPt alone and cisPt-MBRT and cisPt-81 keV. Therefore, the chemotherapeutic effect of cisPt seems to be important by itself (Adam *et al.* 2008).

Moreover, since identical effectiveness in terms of global cell dead was observed for both chemo-radiotherapeutic treatments (with different energy spectra), no dose enhancement appears to significantly contribute by means of Auger electrons (see Appendice 1). Therefore, the effectiveness of cisPt concomitantly to radiation would be explained by synergic factors.

These results are coherent with previous Monte Carlo simulations and works performed (Biston *et al.* 2004, Rousseau *et al.* 2010) in which the survival of the animals treated with cisPt did not differ significantly according to the energy of the subsequent irradiation: 78,0 keV, 78.8 keV or 6 MV.

7 Study of cisPt delivery into glioma cells when liposomes are used as a drug vehicles

The aim of this section was to demonstrate whether liposomes (vesicles described in section 1.3.2) associated to cisPt would increase not only the concentration of Pt inside tumor cells, but also the amount of this metal near or into the nucleus of treated cells. Both cases would imply thus a more efficient cisPt delivery within tumor cells, allowing the decrease of cisPt concentration whilst maintaining the high effectiveness of such treatments. Moreover, a lower drug concentration potentially favored by these biological carriers would mean not only an increased concomitant effect with posterior irradiation, but also a higher protection of healthy cells.

In vitro experiments were performed to assess the (possible) advantages of using cisPt associated to liposomes. However, further experiments are warranted in order to better characterize the vesicles, and to improve both the targeting to the glioma cells and the encapsulation ratio.

As explained in section 2.4 of Materials and methods, the techniques which enabled the quantification of the trace elements inside the cells were: ICP-MS and PIXE, this last one combined with BS. Despite being ID22NI one of the most relevant techniques in the quest of trace metal quantification, their application was exclusively used for the analysis of the metal distribution, as it will be explained through the following sections.

7.1 Quantification of Pt and trace elements within cells: ICP-MS, PIXE and BS

Several techniques were used to analyze the Pt concentration inside the different populations of cells, i.e., dead and alive, in the presence or not of liposomes for the cisPt delivery:

- Inductively coupled plasma mass spectrometry (ICP-MS) and

- Particle induce X-ray emission (PIXE) combined with backscattering spectrometry (BS). These last techniques in particular allowed to quantify not only the Pt concentration but also other trace metals.

7.1.1 Results of Pt content obtained by means of ICP-MS

Inductively coupled plasma mass spectrometry (ICP-MS) is a very useful technique to determine the trace elements present in a solution. One of its advantages is to have higher detection limits in comparison with other routinately used techniques such as inductively coupled plasma optical emission spectrometry (ICP-OES) or atomic absorption. In that way, despite the fact that detection limits depend on the element to analyze and the nature of the sample, for Pt it can achieve the parts per trillion (ppt), i.e., 10^{-18} g of element/g of sample as it is depicted in Figure 7.1.

Figure 7.1. *Elements sensitive to the ICP-MS analysis and approximate detection limits for each element.*

In particular, it was wanted to know the Pt concentration within cells according to the treatment used:

i) cisPt 15 μM administered free (cellular medium solution),or
ii) cisPt 15 μM associated to liposomes at two different concentrations: 2.5 or 5 mg/ml

A standard calibration curve was requested in order to get a linear trend of "intensity" respect to "concentration of Pt" in parts per billion (ppb) (see Figure 7.2). Indeed, one different curve for both isotopes of Pt, i.e. ^{194}Pt = 32.97% and ^{195}Pt = 33.83 % of natural abundance was obtained. Comparisons between both graphs enabled to check possible artefacts during the acquisitions.

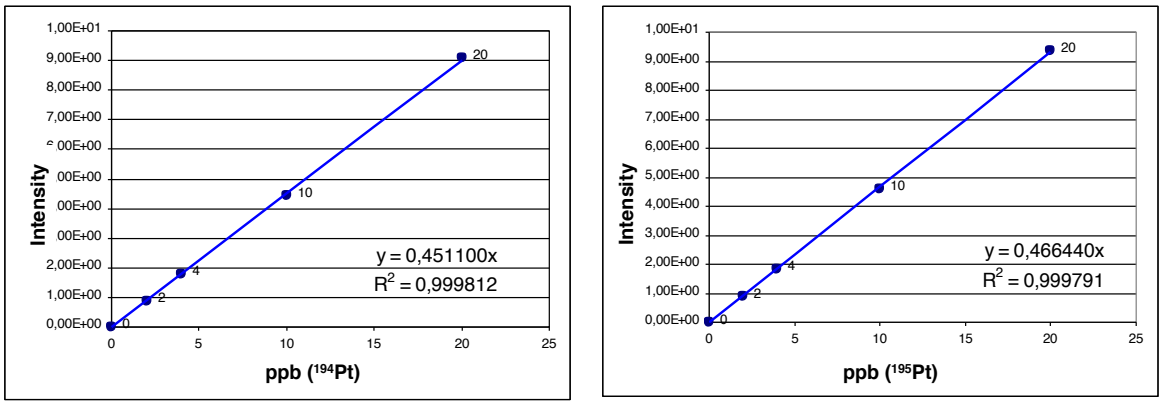

Figure 7.2. *Calibration curves for ^{194}Pt (left) and ^{195}Pt (right). Note that they were almost identical for both isotopes since their natural abundances were practically the same.*

From Figure 7.2, the slope (*s*) of each straight, i.e., of each isotope, was obtained as follows:

$$\text{Intensity} = s \cdot \text{ppb} \qquad \textit{(eq. 7)}$$

The slopes determined from the standard calibration curves were used to calculate the ppb of Pt in the analyzed samples. To that end, the intensity of each isotope of Pt given by the spectrometer (*eq. 8*) was divided by its slope (*eq. 9*):

$$(\text{Intensity}_{Pt} - \text{Intensity}_{solvent}) / \text{Intensity}_{Tl} \qquad \textit{(eq. 8)}$$

$$\text{ppb}_{Pt\text{-sample}} = \text{Intensity}_{Pt\text{-sample}} / s \qquad \textit{(eq. 9)}$$

Finally, the data resulting from ICP-MS could be analized either comparing the concentration of both isotopes or doing the mean of two measurements. In both cases, however, the values obtained must be almost identical due to the close natural abundances between the two isotopes of Pt. See Table 2.2 (section 2.4) to check the natural abundances of Pt isotopes.

Despite the feasibility of both methods, the second type of analysis was chosen, i.e., the mean values of both Pt isotopes. From those data, the final results represented in histograms in Figure 7.3 were obtained:

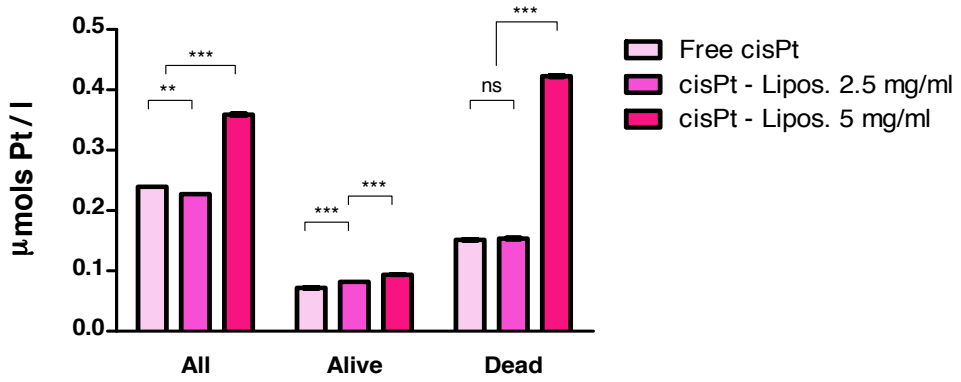

Figure 7.3. *µmols Pt/l obtained by ICP-MS for several populations: all (dead and alive cells analyzed together), alive cells and dead cells treated with several chemical conditions.*

The concentration of Pt in cells dead after treatments was higher in comparison with those that remained alive. This fact is reasonable since that higher amount of Pt could become lethal for those cells.

Differences between treatments were detected for each cell population. For instance, the concentration of Pt was found significantly higher ($p < 0.001$) in those cells previously treated with cisPt associated to liposomes 5 mg/ml. Since that result is more important for dead cells, that fact could point at a higher effectiveness of liposomes 5 mg/ml for cisPt delivery into the cells. Thus, this means a cisPt-to-liposomes concentration ratio of around 1:1000 to detect higher effectiveness on cisPt delivery into the cells, since liposomes 2.5 mg/ml do not allow to increase the concentration of Pt in dead cells with respect to cisPt delivered alone.

In addition, analyses of the remaining living cells together with dead cells were also performed. This population is named "all" in Figure 7.3, and it was included in the analysis in order to assess the trend of living and dead cells by a different way. Consequently, those samples show the same trend of Pt concentration in function of treatments than those obtained from analyzing both populations separately. Liposomes 5 mg/ml seem to increase again the concentration of Pt within cells, specially in dead cells.

For those cells that died after that treatment, the final concentration of Pt found inside them was of 0.42 µmols/l (Table 7.1). Despite to be that the maximum concentration of Pt found within cells, it is about 35 times less concentrated in comparison with the intial solution (cisPt 15 µM). Despite this finding, treatment based on cisPt 15 µM showed a higher effectiveness in terms of

cell killing (~ 30% of cell survival), indicating that this amount of cisPt is enough to become lethal.

Conditions	***All (µmol/l)***	***Alive cells (µmol/l)***	***Dead cells (µmol/l)***
Free cisPt 15 µM	$2.4 \cdot 10^{-1} \pm 1.2 \cdot 10^{-4}$	$7.2 \cdot 10^{-2} \pm 7.6 \cdot 10^{-4}$	$1.5 \cdot 10^{-1} \pm 8.5 \cdot 10^{-4}$
CisPt 15 µM - Liposomes 2.5 mg/ml	$2.3 \cdot 10^{-1} \pm 8.5 \cdot 10^{-5}$	$8.2 \cdot 10^{-2} \pm 4.2 \cdot 10^{-5}$	$1.5 \cdot 10^{-1} \pm 1.1 \cdot 10^{-3}$
CisPt 15 µM - Liposomes 5 mg/ml	$3.6 \cdot 10^{-1} \pm 1.7\ 10^{-3}$	$9.4 \cdot 10^{-2} \pm 4.2 \cdot 10^{-5}$	$4.2 \cdot 10^{-1} \pm 1.3\ 10^{-3}$

Table 7.1. *µmols Pt/l ± SD obtained by ICP-MS for several group of populations: all (dead and alive cells analyzed together), alive cells and dead cells treated with several chemical conditions. These values are represented in histograms in Figure 7.3.*

In order to obtain the quantification not only of Pt, but also of almost all elements present inside the cells, analyses of PIXE and BS were performed at the CENBG. Results are presented in detail through the next section.

7.1.2 Results of Pt and trace elements content obtained by means of PIXE and BS

As explained in section 2.4.2, PIXE is a technique based on the detection of characteristic fluorescence X-rays emitted by the elements present in a sample after being irradiated with particles, generally protons, at energies of MeV. Complementarily to PIXE arises the BS, which allows to normalize the g/cm^2 given by PIXE into µg of each element/g of sample, enabling a fully quantitative analysis unlikely any other technique (Ortega *et al.* 2009).

In order to normalize all the trace elements present in a sample, the procedure explained hereafter is requested. Firstly, the reference samples described in section 2.4.2.2 must be analyzed by using detectors without PIXE filters. Those irradiations enable to obtain the BS spectrum, from which is feasible to determine the deposited charge, by using the program called Simnra. The charge value obtained is subsequently used to determine how depends the solid angle (H) of PIXE detector from the formula below with the energy. That is feasible since the other variables, including M, and T (which is 1) are perfectly known for the reference samples.

$$Y = Y_t \; Q \; H \varepsilon \; T \; M \qquad (eq.\ 10)$$

where Y corresponds to the experimental intensity, Y_t to the theoretical intensity, Q is the charge deposited on PIXE spectra, T is the transmission factor for filters, ε represents the detector efficiency, and M is the superficial mass (g of element / cm^2 of sample).

For biological samples analyses, the use of filter in PIXE detector is necessary. Therefore, the same standards must be irradiated a second time to determine the value of T in equation 10.

Since both H and T values obtained from reference samples depend only on the detector's features and geometry, they remain invariable during the analysis of cells under the same conditions. It makes feasible to determine M, since the remaining variables of equation 10 can be known:

i) Y_t and ε were obtained by the own databases of the program (GupixWin) used to analyze the PIXE spectra.

ii) Y were indeed the "counts" found experimentally from each PIXE spectrum.

iii) Q was determined from the BS spectrum of each sample.

The analysis of each sample must be performed as explained hereafter:

1) From each PIXE spectrum, it is obtained the image corresponding to the part which has been irradiated (Figure 7.4-A).

2) Once that image has been resolved, it must be delimited on it the region of interest (Figure 7.4-B) to perform the subsequent analysis. Both PIXE and BS spectra are generated only from this selected part:

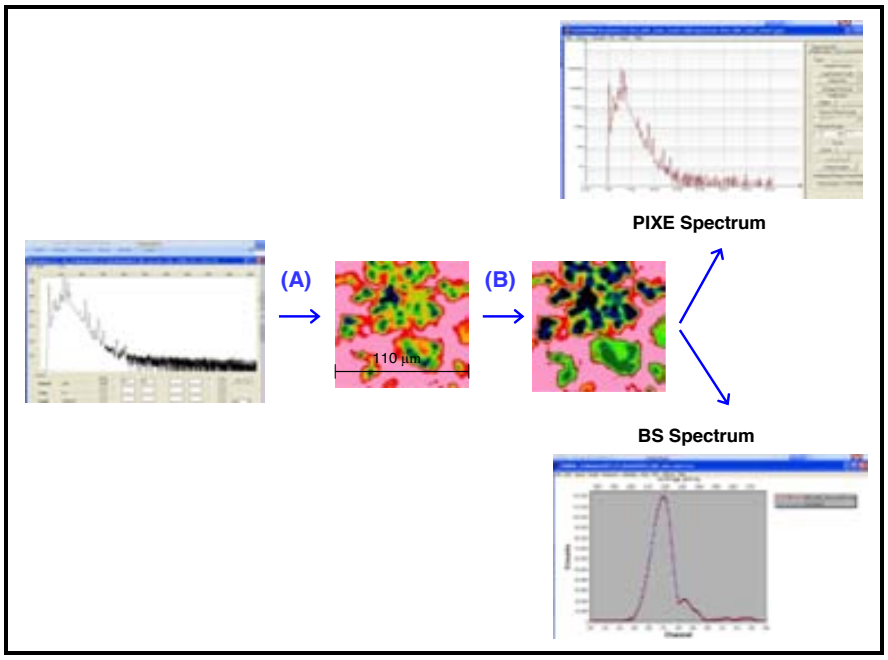

Figure 7.4. *Scheme of both PIXE and BS analyses: A) Image reconstruction, B) selection of the area of interest needed to obtain both PIXE and BS spectra for its further analysis.*

Whereas *Y* value was directly obtained from the PIXE spectrum as "counts", the determination of the deposited charge (*Q*) must be established by analyzing each BS spectrum (see Figure 7.5) in a similar way than that used before for the reference samples. It allows the simulation of different charges (band lenght) and sample thicknesses (band width) up to reach the exact fit for both simulated (blue) and real (red) spectra.

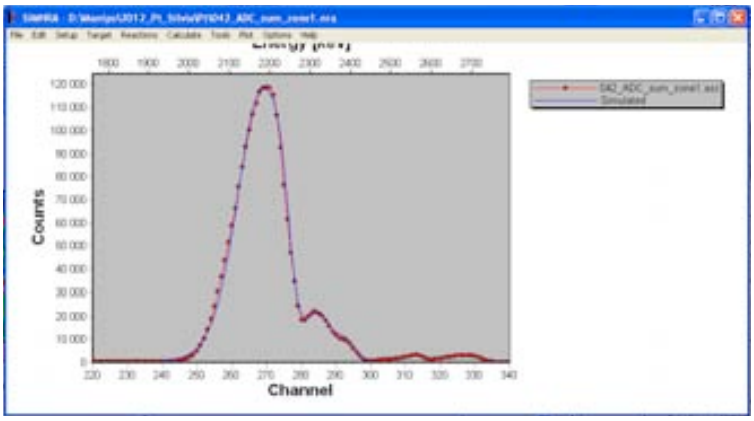

Figure 7.5. *Window of Simnra program, where it is depicted the experimental BS spectrum corresponding to the sample (red) and to the simulated (blue).*

Once the *Q* value has been established, it is feasible to determine the value of *M* since it is the unique unknown variable of equation 10. Finally, dividing the superficial mass, *M* (μg element/cm^2 sample) by the thickness, *t* of each sample (g sample/cm^2 sample), the content (μg/g) of each trace element inside the cells can be normalized.

In particular, the aim was the determination of Pt inside cells according to the way by which cisPt had been delivered:

i) cisPt 7 μM administered free (cellular medium solution), or
ii) cisPt 7 μM associated to liposomes 0.75 mg/ml

Despite lower concentrations of cisPt and liposomes were used for PIXE experiments in comparison with ICP-MS, subcellular analysis of F98 showed very similar results among both techniques. Those results are depicted in Figure 7.6 and explained hereafter.

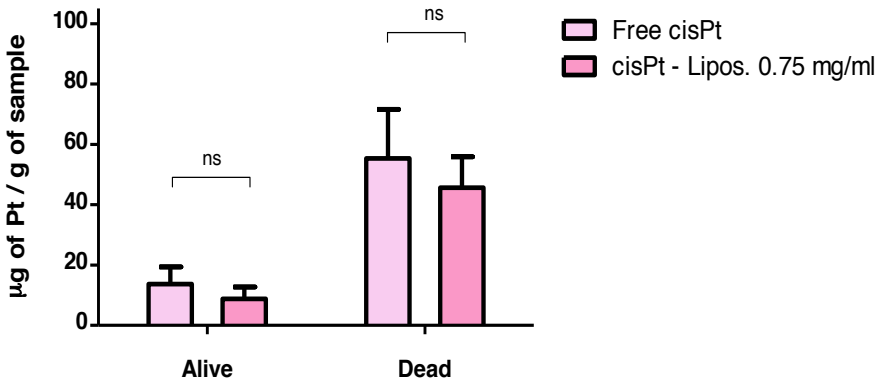

Figure 7.6. *Fully quantitative results (μg of Pt/g of sample) from PIXE and BS measurements. All the dead cells present a larger content of Pt inside, in comparison with living cells.*

All dead cells presented significantly higher amount of Pt than those surviving cells as it is reported in Table 7.2.

Conditions	***Alive cells (µg Pt/g)***	***Dead cells (µg Pt/g)***
Free cisPt 7 µM	1.4·10 ± 5.7	5.5·10 ± 1.6·10
CisPt 7 µM - Liposomes 0.75 mg/ml	8.8 ± 4.0	4.6·10 ± 1.0·10

Table 7.2. *µg of Pt/g of sample ± SD found for the different cell populations previously incubated with different cisplatin-based treatments. These values are represented in histograms in Figure 7.6.*

Again, that fact was logical, since in dead cells cisPt became lethal for cells. Moreover, the content of Pt intracellularly was practically the same in the presence or not of liposomes 0.75 mg/ml. This result is coherent with the one previously observed for liposomes at concentration of 2.5 mg/ml (Figure 7.3). In fact, the concentration of Pt was found significantly higher ($p < 0.001$) in dead cells previously treated with cisPt associated to liposomes 5 mg/ml. That fact can be understood as a higher effectiveness of liposomes 5 mg/ml for cisPt delivery into the cells. Therefore, the cisPt-to-liposomes concentration ratio should be at around of 1:1000.

Unlikely ICP-MS, tabulation of emitted X-rays energies for each element enabled the identification of other elemental components present in the samples. For instance, PIXE allowed the quantification of the Ca-to-K content ratio within cells (Figure 7.7).

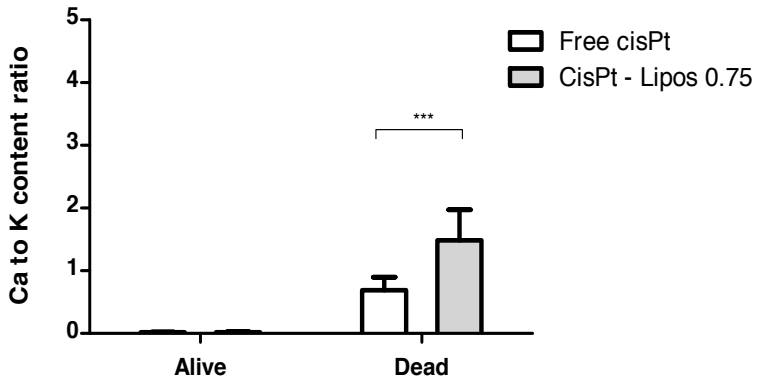

Figure 7.7. *Ca-to-K content ratio according to the treatment and cell population.*

That ratio is interesting since it is well-known that an increase in intracellular concentration of Ca leads to a subsequent decrease of K in an attempt to overcome the excess of cations inside the cells. Moreover, that effect seems to play an essencial role in triggering apoptotic cell death pathway (Verheij & Bartelink 2000, Serrano *et al.* 2011).

In order to obtain that ratio, the amount of Ca (µg/g) was divided by the amount of K (µg/g) for each analyzed sample (Table 7.3).

Conditions	***Alive cells (µg Ca/g)***	***Dead cells (µg Ca/g)***	***Alive cells (µg K/g)***	***Dead cells (µg K/g)***
Free cisPt 7 µM	$5.6 \cdot 10^2 \pm 1.2 \cdot 10^2$	$4.1 \cdot 10^3 \pm 8.0 \cdot 10^2$	$3.1 \cdot 10^4 \pm 4.1 \cdot 10^3$	$6.5 \cdot 10^3 \pm 2.4 \cdot 10^3$
CisPt 7 µM - Liposomes 0.75 mg/ml	$6.62 \cdot 10^2 \pm 4.2 \cdot 10^2$	$3.3 \cdot 10^3 \pm 1.1 \cdot 10^3$	$3.5 \cdot 10^4 \pm 6.2 \cdot 10^3$	$2.6 \cdot 10^3 \pm 1.4 \cdot 10^3$

Table 7.3. *Quantitative values (µg/g) of Ca and K found for the different cell populations previously incubated with different cisplatin-based treatments. These values were used to calculate the Figure 7.7.*

The results concerning this ratio indicate that an increase of Ca content was detected in dead cells, as it is depicted in Figure 7.7 and Table 7.3. As a consequence, the amount of K was observed to decrease in those populations, specially when dead cells were previously treated with cisPt associated to liposomes. Hence, in that case, the Ca-K content ratio was found to be higher ($1.5 \pm 4.9 \cdot 10^{-1}$) in comparison with cells dead by cisPt administration without liposomes ($6.9 \cdot 10^{-1} \pm 2.1 \cdot 10^{-1}$) (see Figure 7.7). Moreover, the increase in the Ca-K ratio of those dead cells could be an indicator of apoptotic cell death, since both phenomena seem to be related (Verheij & Bartelink 2000, Serrano *et al.* 2011).

On the other hand, remaining living cells presented lower Ca-K ratios (Figure 7.7), i.e., higher amounts of K rather than Ca, such as it is reported in Table 7.3. Moreover, since these data for surviving cells are correlated to the values obtained from untreated cells (Figure 7.8 and Table 7.4) it is possible to confirm that those cells remained undoubtely alive after treatments despite the little content of Pt appearing inside them.

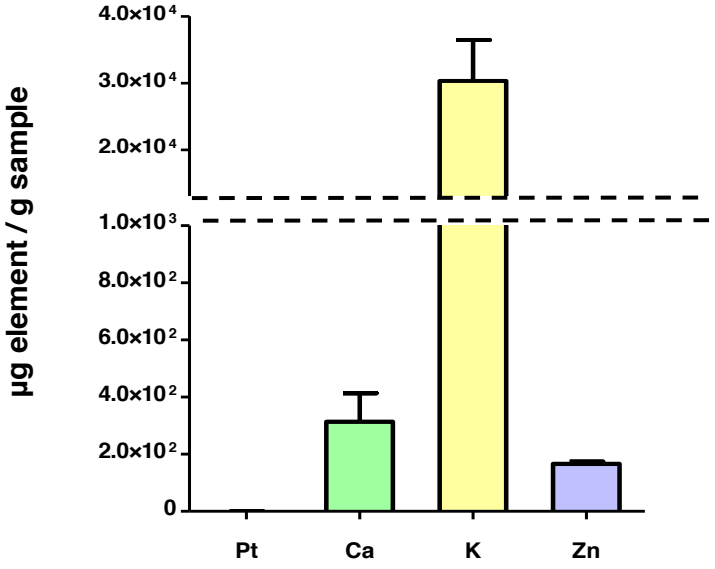

Figure 7.8. *Values (µg/g ± SD) of Pt, Ca, K and Zn found in untreated control cells. Note that K is one of the most abundant ions which can be found inside the cells.*

Conditions	***µg Pt / g***	***µg Ca / g***	***µg K / g***	***µg Zn / g***
Untreated cells	$2.5 \cdot 10^{-1} \pm 5 \cdot 10^{-1}$	$3.1 \cdot 10^{2} \pm 9.9 \cdot 10^{1}$	$3.0 \cdot 10^{4} \pm 6.1 \cdot 10^{3}$	$1.7 \cdot 10^{2} \pm 7.1 \cdot 10^{0}$

Table 7.4. *µg/g ± SD of Pt, Ca, K and Zn found in untreated control cells. These values are represented in histograms in Figure 7.8.*

Besides Ca and K, the content of another trace element such as Zn appeared to differ among samples, as it is represented in Figure 7.9 and in Table 7.5.

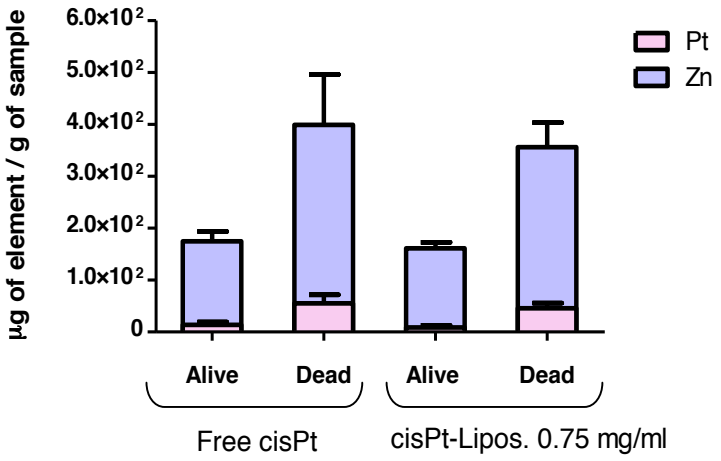

Figure 7.9. *Values (µg/g) of Pt and Zn found for the different cell populations previously treated either with cisPt associated to liposomes (cisPt-Lipos. 0.75 mg/ml) or cisPt without them (free cisPt).*

Whereas the Zn content in living cells (Table 7.5) is almost identical to that found in untreated cells (Table 7.4), almost the same increase of Zn content could be detected in dead cells after both treatments, based on free cisPt and cisPt associated to liposomes. This increase of Zn in dead cells seemed to be correlated with the amount of Pt, exhibiting both elements the same trend (Figure 7.9).

Conditions	***Alive cells (µg Zn/g)***	***Dead cells (µg Zn/g)***	***Alive cells (µg Pt/g)***	***Dead cells (µg Pt/g)***
Free cisPt 7 µM	$1.7 \cdot 10^2 \pm 1.9 \cdot 10$	$4.0 \cdot 10^2 \pm 9.7 \cdot 10$	$1.4 \cdot 10 \pm 5.7$	$5.5 \cdot 10 \pm 1.6 \cdot 10$
CisPt 7 µM - Liposomes 0.75 mg/ml	$1.6 \cdot 10^2 \pm 1.2 \cdot 10$	$3.6 \cdot 10^2 \pm 4.8 \cdot 10$	8.8 ± 4.0	$4.6 \cdot 10 \pm 1.0 \cdot 10$

Table 7.5. *µg/g of Pt and Zn found for the different cell populations previously treated either with cisPt associated to liposomes (cisPt-Lipos. 0.75 mg/ml) or cisPt without them (free cisPt). These values are represented in histograms in Figure 7.9.*

Since intracellular Zn plays an essential role in the function of metallothionein (MT) proteins, which provide protection against metal toxicity, this correlation could help to understand better the mechanisms by which glioma cells may acquire resistance against cisPt treatments. This hypothesis will be further developed through the Discussion section.

7.2 Distribution of Pt and trace elements within glioma cells: ID22NI

Synchrotron X-ray fluorescence emission was used only to determine the metal distribution within cells. One of the main reasons for that was the lack of enough data to obtain quantitative results, since only one or two cells per condition could be irradiated. In addition, in samples containing liposomes, the presence of these vesicles interfere in the quality of images since they appear covering part of the cells.

Since not only the quantification, but also the distribution of Pt inside the cells will determine the effectiveness of chemo-radiotherapeutic treatments, measurements of synchrotron X-ray fluorescence emission at the nanoscale were performed at ID22NI station (ESRF).

By scanning the sample in the hard X-ray nanoprobe, elemental maps are produced for the metal presents in the cells. In fact, analyses were performed only for living cells due to their good appearance after treatments, keeping intact all their internal structures. The X-ray fluorescence spectrum of each sample was analyzed by using the non-linear least-squares fitting code PyMCA (Solé *et al.* 2007) developed at the ESRF. Those analyses were splited into 2 parts: 1) the batch peak fitting process, followed by 2) the 2D representation of the resulting quantification. Both steps are explained hereafter:

1) Peak fitting. This process is based on the fact that the pattern of peaks detected in each spectrum is directly related to the elements present in the sample (Solé *et al.* 2007).

   However, in order to obtain the fully identification of peaks, prior calibration of the detector was required. For that it was needed to account all the data concerning the detector that was saved during irradiations. After that, the peak fitting could be started, identifying firstly both peaks, Ar present in the air (K-edge = 2.96 keV) and backscatted photons which had the same energy than the incident ones (17 keV). The program uses by default a built-in database, which allows to identify the remaining peaks of the spectrum (Solé *et al.* 2007).

The final spectrum for each sample is like those represented in Figure 7.10, that in this case corresponds to an untreated cell (control).

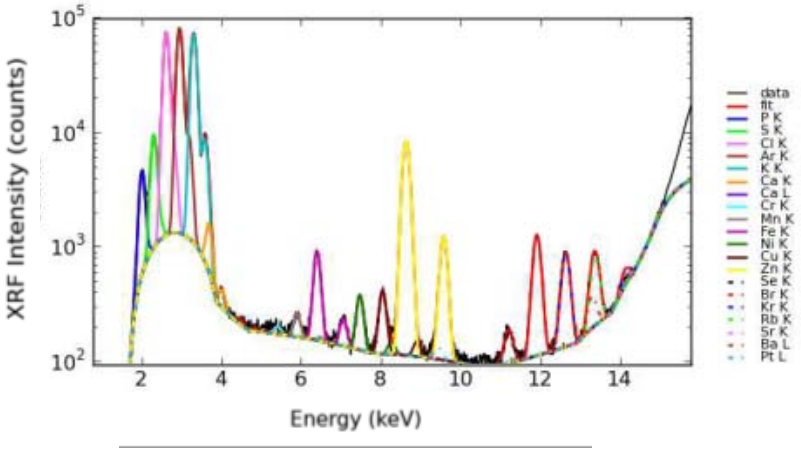

Figure 7.10. *X-ray fluorescent spectrum obtained by PyMCA, corresponding to an untreated cell irradiated at ID22NI beamline.*

2) Fluorescent map. The obtention of those images requires the prior fitting of all the peaks appearing in the spectrum., i.e., each map is obtained via the program batch fitting.

The resulting fluorescent maps could be either of the global fluorescence emission (Figure 7.11-A) or only of the element of interest, Pt in this Ph.D. dissertation (Figure 7.11-B).

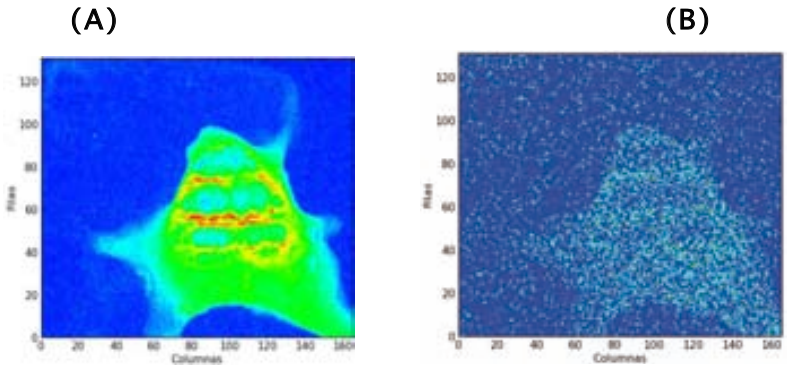

Figure 7.11. *Two fluorescence maps for an untreated cell: A) Global fluorescence map, and B) Pt fluorescence map.*

In particular, the aim was the determination of Pt distribution inside living cells depending on the way by which cisPt was delivered (the same samples that ones used for PIXE analyses):

i) cisPt 7 μM administered free, or
ii) cisPt 7 μM associated to liposomes 0.75 mg/ml

Only the images of cells treated with cisPt alone are depicted. Despite the images of cells treated with cisPt associated to liposomes show a similar elemental's distribution, liposomes interact with cells. This fact implies that liposomes appear in the fluorescence mappings, covering part of the cellular region.

In particular, the Pt fluorescence map depicted in Figure 7.12 shows a distribution of this metal quite uniform inside the cells.

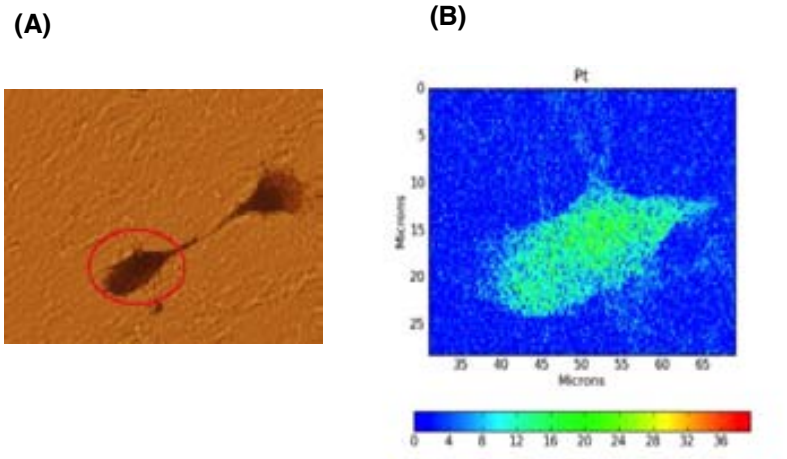

Figure 7.12. *Images corresponding to one cell which survived to the treatment with cisPt 7 μM: A) Microscopic image at 40x, and B) Intracellular Pt fluorescence map (blue: low signal intensity, red: high signal intensity).*

Nevertheless, a little amount of Pt seems to be localized mainly in the central part of the cell, where the nucleus is supposed to be. From the qualitative analyses made at ID22NI it is difficult to appreciate differences on the amount of Pt in the nucleus of living cells in the presence or not of liposomes. However, the proportion of Pt must be very low in the two cases since cells survived to both treatments.

On the other hand, fluorescence maps for Ca (Figure 7.13-A) and K (Figure 7.13-B), allow to corroborate the quantitative results obtained before by PIXE measurements.

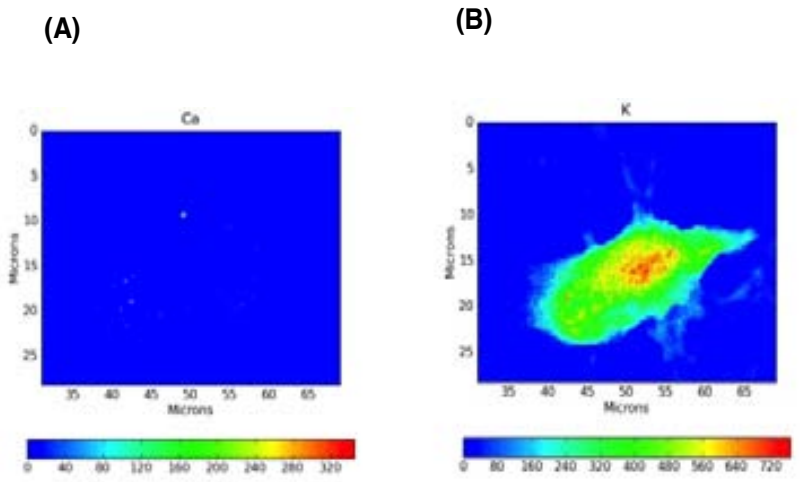

Figure 7.13. *Fluorescence maps (blue: low signal intensity, red: high signal intensity) corresponding to one surviving cell previously treated with cisPt 7 μM: A) intracellular Ca distribution, and B) intracellular K distribution.*

In all surviving cells (regardless of the treatment) Ca presence was almost negligible inside of them. By contrast, the content of intracellular K was substantially higher for both treatments, specially within the nucleus. These findings were coherent with the lower Ca-K ratios of living cells (Figure 7.7 and Table 7.3), analyzed with PIXE and BS.

The amount of Zn was lower, specially in the nucleus of living cells (see Figure 7.14). Moreover, Zn seems to accumulate in a granular-shape mainly in the cytoplasm of cells treated with cisPt administered either with or without liposomes.

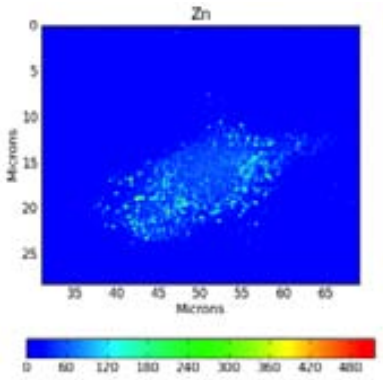

Figure 7.14. *Fluorescence map (blue: low signal intensity, red: high signal intensity) of Zn for one living cell pre-treated with cisPt 7 μM.*

Discussion

Information on the concentration and distribution of Pt inside the cells could allow to better understand the mechanisms of action of cisPt. For that aim, several techniques were performed to compare both parameters as a function of the cisPt delivery system used.

In particular, PIXE and BS measurements were performed with cells treated with lower concentrations of cisPt and liposomes in comparison with ICP-MS. The decrease of cisPt concentration had the aim of reduce the high lethality of the drug observed at concentrations of 15 μM by flow cytometric analyses (data not shown). In addition, this reduction of cisPt until concentrations of 7 μM led also to minimize the presence of liposomes in the dried-frozen samples. This allowed to avoid as much as possible the errors due to the quantitative analysis of liposomes instead of cells.

By using both ICP-MS and PIXE techniques, the concentration of Pt inside the cells was assessed. Higher contents of intracellular Pt were detected in dead cells in comparison with surviving ones. An optimal cisPt-to-liposomes concentration ratio of around 1:1000 could lead to a higher efficiency in the drug delivery with a larger amount of Pt within dead cells. Under those conditions, a decrease of the cisPt concentration would be thus feasible, decreasing the impact of cisPt on healthy tissues and enhancing the concomitant effects between this drug and a subsequent irradiation. The increase in the presence of liposomes would not involve inconvenients since they do not present any cell toxicity. Nevertheless, the Pt concentration, even in liposomes-delivery treatments was found to be too much little to produce any dose enhancement after irradiation of loaded cells, as confirmed by Monte Carlo simulations.

PIXE technique not only enabled to corroborate ICP-MS results but also allowed the quantification of other trace metals present inside the cells. For instance, an increase of the Ca-to-K content ratio could be detected in dead cells, specially in those treated previously with cisPt associated to liposomes 0.75 mg/ml. The increase of cytosolic Ca after this treatment can be associated hypothetically to an increase of cells dying by apoptosis. It could be feasible since it is well-determined that the inability for cells to exclude cytoplasmatic Ca can culminate in caspase activation and cell death by apoptotic pathway (Verheij & Bartelink 2000, Zong & Thompson 2006, Serrano *et al.* 2011).

However, taking into account that the content of intracellular Pt did not differ significantly between dead cells resulting from cisPt treatments either with or without liposomes, the large rate of apoptotic cell dead after treatments based on cisPt-liposomes 0.75 mg/ml could be explained by two hypothesis:

i) Liposomes can produce alterations in the membrane potential of treated cells leading to a cellular imbalance of Ca transport.

ii) The amount of intracellular Pt does not differ in presence or not of liposomes 0.75 mg/ml, but however, the Pt delivery is more efficient when the drug is associated to these vesicles. Under these conditions, Pt could reach the DNA more efficiently, leading to a large percentage of apoptotic cells. However, from the qualitative analyses made at ID22NI it is difficult to appreciate differences on the amount of Pt in the nucleus of living cells in the presence or not of liposomes.

Although further analyses are warranted to corroborate these two hypothesis, liposomes seem to provide a higher efficiency in the drug delivery, not only increasing probably the ratio of apoptotic cells, but also allowing the decrease of the cisPt concentration, which can lead to the aforementioned advantages. This effectiveness can become higher by optimizing the concentration (and other features, such as composition, size etc.) of liposomes.

In addition, all dead cells presented similar values of Zn, and higher than those detected in alive cells. That fact resembles the trend observed for Pt in both treatments, indicating a direct relationship between these two metals. The interaction between Pt and Zn has been already highlighted in other investigations (Ortega *et al.* 1996). Since Zn binds metallothionenins (MT), which are a kind of proteins involved in several cell processes such as detoxification of heavy metals (Thirumoorthy *et al.* 2007), an increase of both Zn and Pt concentrations inside the cells would be related to an attempt to overcome the excess of this cytotoxic element (Ortega *et al.* 1996). Nevertheless, further experiments are warranted to understand better this process.

Despite the limit of detection of PIXE is around 2 μg/g, whereas for ID22NI beamline is of around 0.1 μg/cm^2, synchrotron X-ray fluorescence emission was used only to determine the metal distribution within cells. One of the main reasons for that was the lack of enough data to obtain quantitative results, since only one or two cells per condition could be irradiated. In addition, in samples containing liposomes, the presence of these vesicles interfere in the quality of images since they appear covering part of the cells. Despite this inconvenient, the same

samples in PIXE and in ID22NI were used, although only the distribution of each element was determined in ID22NI.

The analysis was focused only on living cells since they offered a good preservation of their structures, keeping intact their membranes. A quite uniform Pt distribution could be detected inside all alive cells, with a slighltly larger amount of Pt observed in the nuclear part. Those findings agree with the known reactivity of cisPt which binds to numerous nucleophilic sites in the cytosol and in the nucleus (Ortega *et al*. 2006).

On the other hand, K was found mainly in the nucleus, whereas Ca was almost not detected intracellularly. That fact could support the premise by which an increase of cytosolic Ca may become toxic and trigger apoptosis in a subsequent step.

Finally, Zn seems to form little grains distributed through the cytoplasm, where the MT are expected to be found. This finding is coherent with the quite uniform Pt distribution observed inside all alive cells. In addition, very low presence of Zn was detected in the nucleus, where DNA-Pt adducts are removed by NER pathway instead of by MT, and Zn is not required.

CHAPTER IV. Results: *In vitro* experiments II

8 Comparison of effectiveness of COE and white BB synchrotron radiation

This section reports the comparison of the cell damage after irradiations with a clinical orthovoltage equipment (COE) and with synchrotron sources. Both sources differ in the dose-rate (COE of 0.02 Gy s^{-1} and white BB synchrotron irradiations of 5000 Gy s^{-1} approximately), and in the mean energy (35 keV for COE and 100 keV for BB).

The same doses (6, 12, 18 and 24 Gy), prescribed at the bottom of each well as a reference, were deposited with an orthovoltage machine and with white BB at the synchrotron.

The results obtained are presented throughout the next sections.

8.1 Assessment of γH2AX IF on the cellular DNA: 2 and 17 h after irradiations

The radiation-induced γH2AX IF intensity on F98 glioma rat cells were performed 2 and 17 h after orthovoltage clinical-like X-ray and synchrotron irradiations. Note that results of white BB synchrotron-based irradiations are exactly the same that those showed in section 4.

- Assessment of γH2AX IF in F98 glioma rat cells analyzed by bivariant flow cytometry 2 h after irradiations:

Large nuclear damage is expected to be reported on F98 glioma cells short time after both kind of irradiations. In fact, more than 90% of cells exhibit large γH2AX IF signal 2 h after both orthovoltage clinical-like and white BB irradiations (Figure 8.1).

Nevertheless, differences between them can be detected at 6 Gy. At this dose, whereas COE exhibits a percentage of damaged cells of 91 ± 7 (mean % ± SD), white BB synchrotron-based mode leads to a smaller percentage of cells with γH2AX corresponding to 57 ± 19 (see Figure 8.1).

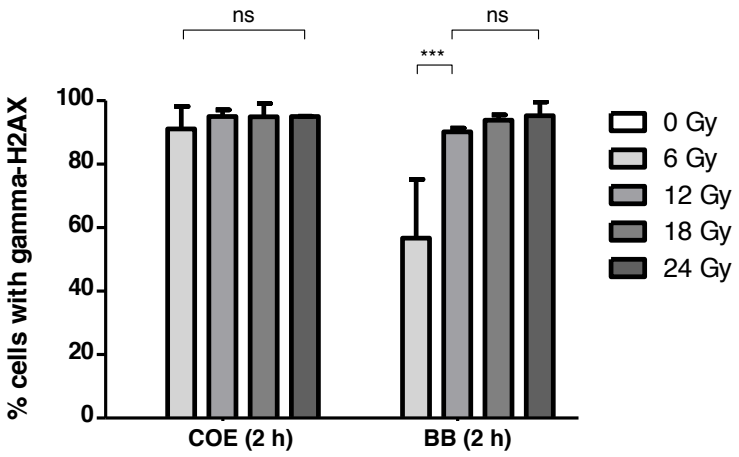

Figure 8.1. *Percentage (%) of cells with γH2AX 2 h after both COE and white BB irradiations, according to the dose escalation up to 24 Gy.*

Probably as a consequence of their respective mean energies, a different trend in the saturation of the radiation-induced damage is observed for both radiation techniques. COE, which it is featured by a lower energy spectrum, exhibits an endpoint in terms of % of cells with γH2AX 2 h after irradiations of around 6 Gy. This is lower with respect to the same endpoint for white BB exposures, which was assessed at ~ 12 Gy. Besides there is little *in vitro* or *in vivo* data regarding the radiobiological properties of low-energy X-rays, it is well assumed that low-energy photons interact mainly through photoelectric process. This leads to a local density of induced damage directly and/or through the release of ROS (see section 1.4), which may increase the number of cells exhibiting DSBs (Mestres *et al.* 2008).

Differences between both irradiation modes can also be detected in the γH2AX IF intensity, i.e., the frequency of DNA DSBs, induced on cells, as it is depicted in Figure 8.2.

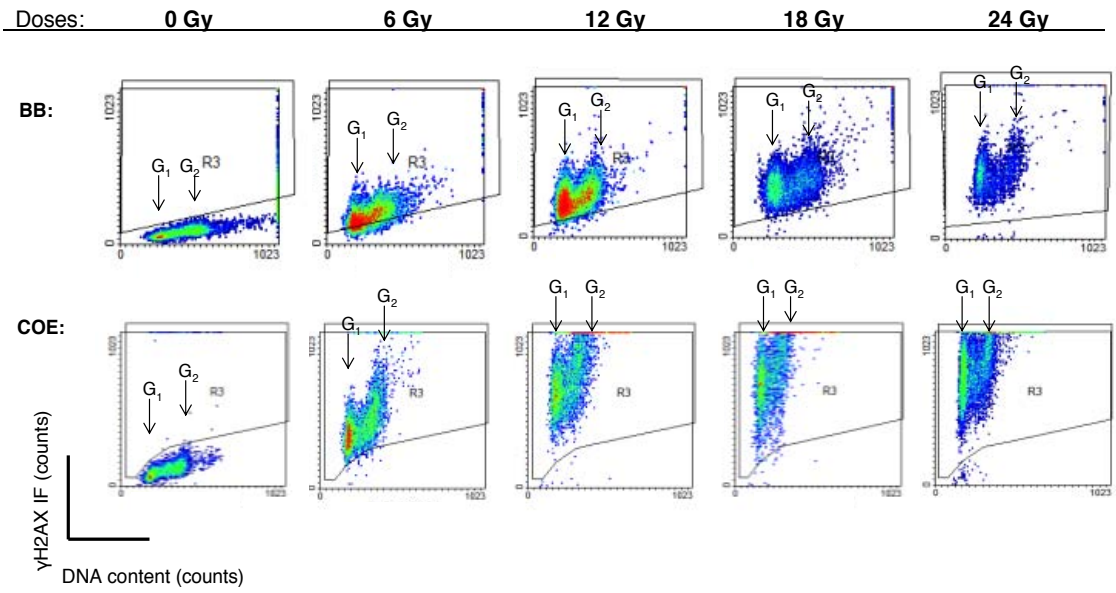

Figure 8.2. *Counts of γH2AX IF versus cellular DNA content stained with PI of F98 glioma rat cells 2 h after COE and BB irradiations at 0, 6, 12, 18, 24 Gy. Cells in G_1- or G_2 phases of cell cycle are indicated in the plots. Although the experiment was performed at least by triplicate, only the result of one experiment is shown.*

Despite γH2AX IF intensity increases as a function of dose for both radiation modes, this signal is more intense in cells irradiated with the clinical-like source (Figure 8.2). It is noteworthy to highlight that cells exhibiting the highest Alexa staining intensity, like in the case of cells irradiated with the COE, are included in the analysis despite to be set at the axis (section 2.3.1 of Materials and methods).

According to the results, this orthovoltage-based source seems to generate a higher amount of DSBs per nucleus compared with white BB SR. Therefore, low-energy photons not only lead to increase the number of cells exhibiting DSBs, but also the ratio of DSBs per cell.

- Analysis of γH2AX IF intensity according to the DNA content of F98 glioma rat cells 2 h after irradiations:

Regarding the DNA content measured in Figure 8.2, the induction of DSBs is higher in G_1 phase of cell cycle rather than in S and G_2 phases. This is due to the fact that 2 h after irradiations cells have not enough time to progress through the cell cycle, i.e., S and G_2 phases.

- Assessment of γH2AX IF in F98 glioma rat cells analyzed by bivariant flow cytometry 17 h after irradiations:

Like in the aforementioned case of MBRT and BB exposures, remaining foci after the doubling time of F98 glioma rat cells could be correlated with lethal lesions.

Complementary measurements, which are depicted in Figure 8.3, have been performed 17 h after both kind of X-rays exposures. In particular, a common high decrease in the number of γH2AX positive glioma cells is observed 17 h after both irradiations in comparison with analyses performed at 2 h (see Figure 8.1).

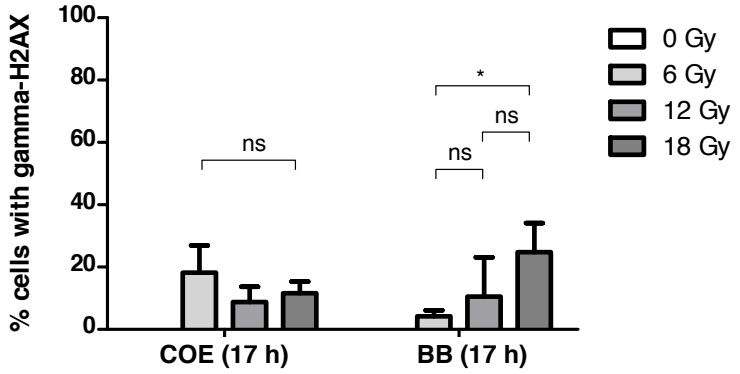

Figure 8.3. *Percentage (%) of cells with γH2AX 17 h after both COE and white BB irradiations, as a function of the dose escalation up to 18 Gy.*

No differences among doses ($p > 0.05$) are observed in the percentage of damaged cells analyzed at 17 h for the COE exposures (≈ 13%). The endpoint seems to be still at around 6 Gy (as it was previously observed at 2 h), since no variation in the percentage of damaged cells are detected from this dose up to 18 Gy. On the other hand, BB irradiations lead to almost the same percentage of nuclear-damaged cells that COE exposures at doses ≥ 12 Gy (≈ 13%). Since the larger % of cells with γH2AX can be detected at 12 Gy (remaining unchanched up to 18 Gy) after white BB synchrotron irradiation, the endpoint can be established around this dose for this technique.

This is also confirmed by analyzing the γH2AX IF cellular intensity 17 h after both X-rays radiation modes (Figure 8.4).

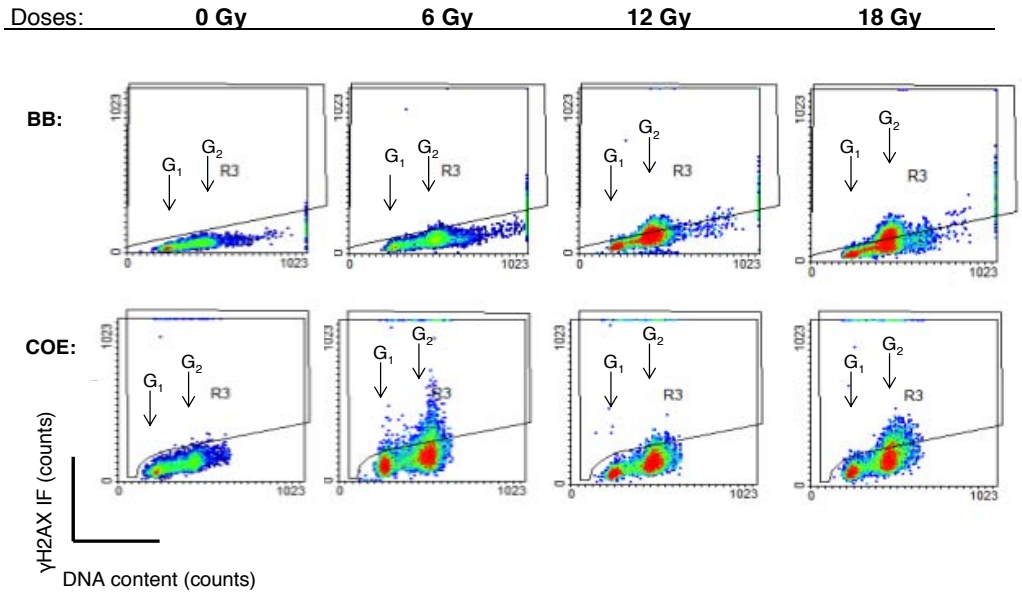

Figure 8.4. *Counts of γH2AX IF versus cellular DNA content stained with PI of F98 glioma rat cells 17h after COE and white BB irradiations at 0, 6, 12 and 18 Gy. Cells arrested in G_1- and G_2 phase appear indicated in the plots. Although the experiment was performed at least by triplicate, only the result of one experiment is shown.*

Despite the remarkable decrease of γH2AX IF cell intensity observed 17 h after both irradiations, a slightly higher γH2AX signal within the cell nucleus can be still detected after COE compared with white BB irradiations up to 18 Gy (Figure 8.4).

- Analysis of γH2AX IF intensity according to the DNA content of F98 glioma rat cells 17 h after MBRT and BB irradiations:

Analysis of γH2AX IF intensity as a function of DNA cell content 17 h after the two X-rays radiation modes (Figure 8.4) reveales that almost all γH2AX positive cells are arrested mainly in G_2 phase after their progression through the cell cycle.

8.2 Survival analysis assessed by flow cytometry

Flow cytometric analyses were performed 48 h hours after treatments to correlate the proportion of remaining γH2AX foci 17 h after irradiations with the amount of apoptotic cells. Normalized data for surviving cells (Table 8.1), and plotted in histograms in Figure 8.5-A are in the frame of results obtained in the previous section.

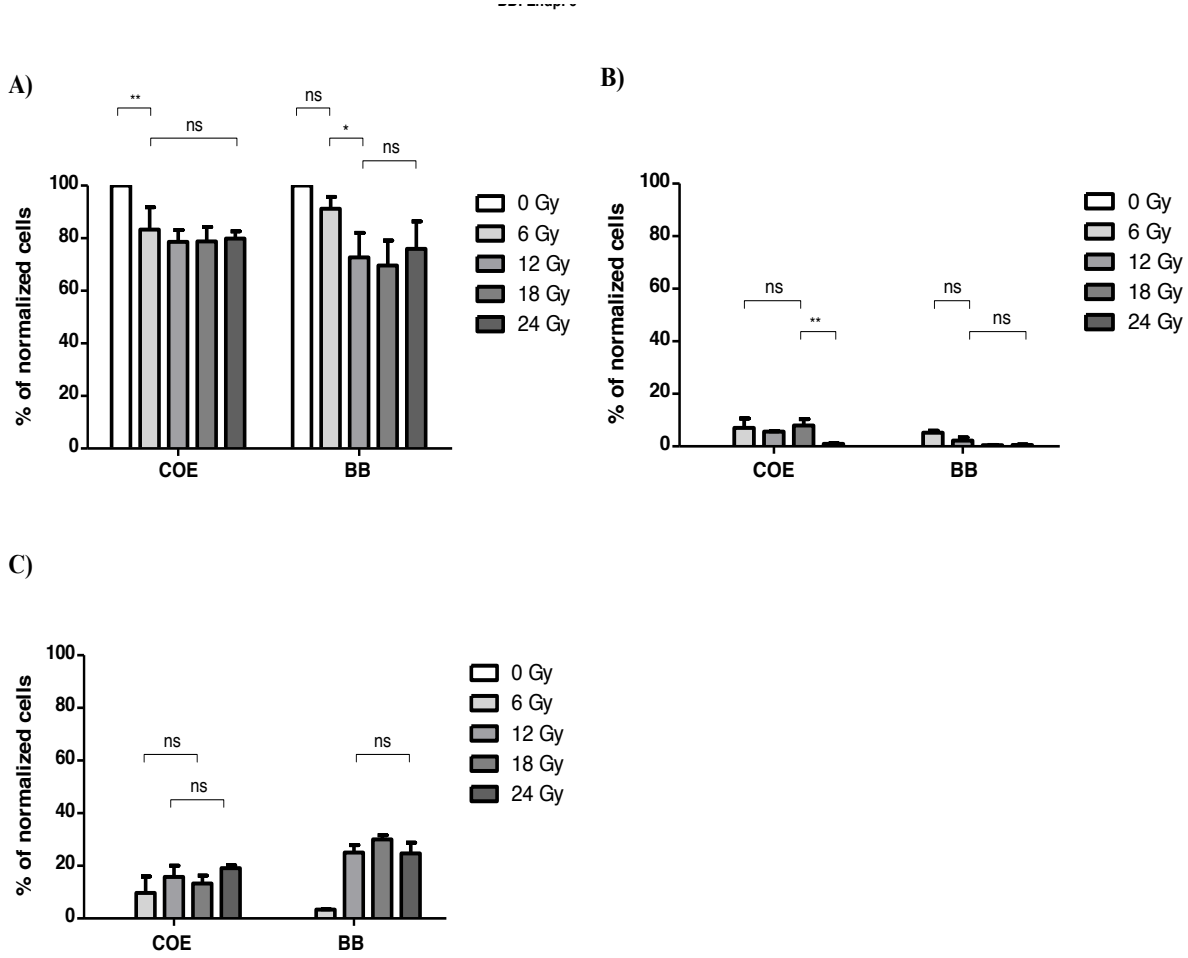

Figure 8.5. *Percentage of normalized A) living, B) early apoptotic and C) dead cells after COE and white BB irradiations in a dose escalation ranging from 0 to 24 Gy.*

Although, cells irradiated with lower dose rates seem to exhibit a smaller percentage of dead (specially via necrosis as it is detected in Figure 8.5), it seems that the endpoint, defined as the threshold dose required to achieve the maximal effectiveness in terms of cell survival, can be established again at around 6 Gy for COE, and at around 12 Gy for white BB synchrotron radiation. Almost the same percentage of surviving cells are detected at doses ≥ 12 Gy (see Table 8.1).

Doses (Gy)	*% of normalized surviving cells after COE (Mean % ± SE)*	*% of normalized surviving cells after BB (Mean % ± SE)*
0	100	100
6	83 ± 8	91 ± 5
12	79 ± 5	73 ± 9
18	79 ± 6	70 ± 10
24	80 ± 3	76 ± 10

Table 8.1. *Percentages of normalized values for surviving cells analyzed by flow cytometry 2 days after COE and white BB irradiations. These data are graphically represented in histograms in Figure 8.5-A.*

In addition, the process of cell death seems to differ as a function of radiation mode. Indeed, the percentage of cells undergoing early apoptosis 48 h after kV clinical-like exposures is higher when compared to the same population for BB irradiations (Figure 8.5-B and Table 8.2).

Seamless and valley doses (Gy)	*% of normalized early apoptotic cells after COE (Mean % ± SE)*	*% of normalized early apoptotic cells after BB (Mean % ± SE)*
0	0	0
6	7 ± 4	5.2 ± 0.8
12	5.6 ± 0.2	2.2 ± 1.1
18	8 ± 2	0.4 ± 0.1
24	0.9 ± 0.2	0.6 ± 0.2

Table 8.2. *Percentages of normalized values for early apoptotic cells analyzed by flow cytometry 2 days after COE and white BB irradiations. These data are graphically represented in histograms in Figure 8.5-B.*

Orthovoltage irradiations at the hospital show an increased number of pre-apoptotic cells, which remain unchanged until 18 Gy. Only at doses as high as 24 Gy, the percentage of early apoptotic cells decreases (Table 8.2).

In contrast, according to both Figure 8.5-C and Table 8.3, the normalized percentage of cells undergoing late apoptosis and necrosis 48 h after treatments is higher for treatment based on white BB synchrotron radiation. However, the percentage of dead cells at 6 Gy is very low due to the sparse effectiveness of BB at this dose, which is set below the endpoint. For the rest of doses ranging from 12 to 24 Gy, no significant differences are observed. Moreover, the percentage of dead cells at the highest doses, i.e., 24 Gy, reported in Table 8.3 seems not to differ according to the radiation's features.

Seamless and valley doses (Gy)	*% of normalized dead cells after COE (Mean % ± SE)*	*% of normalized dead cells after BB (Mean % ± SE)*
0	0	0
6	10 ± 6	3.4 ± 0.2
12	16 ± 4	25 ± 3
18	13 ± 3	30.0 ± 1.7
24	19.2 ± 1.1	25 ± 4

Table. 8.3. *Percentages of normalized values for dead cells, including late apoptotic and necrotic cells analyzed by flow cytometry 2 days after COE and white BB irradiations. These data are graphically represented in histograms in Figure 8.5-C.*

8.3 Metabolic recovery analyzed by QBlue test

The metabolic activity of living cells was analyzed by using the non-toxic QBlue assay. In this case, the first measurement was performed at the third day after treatments, when cells irradiated at doses as low as 6 Gy show a significant recovery after both irradiation modes (Figure 8.6-D). At this time, a larger cell recovery can be detected in cells irradiated at any dose with COE.

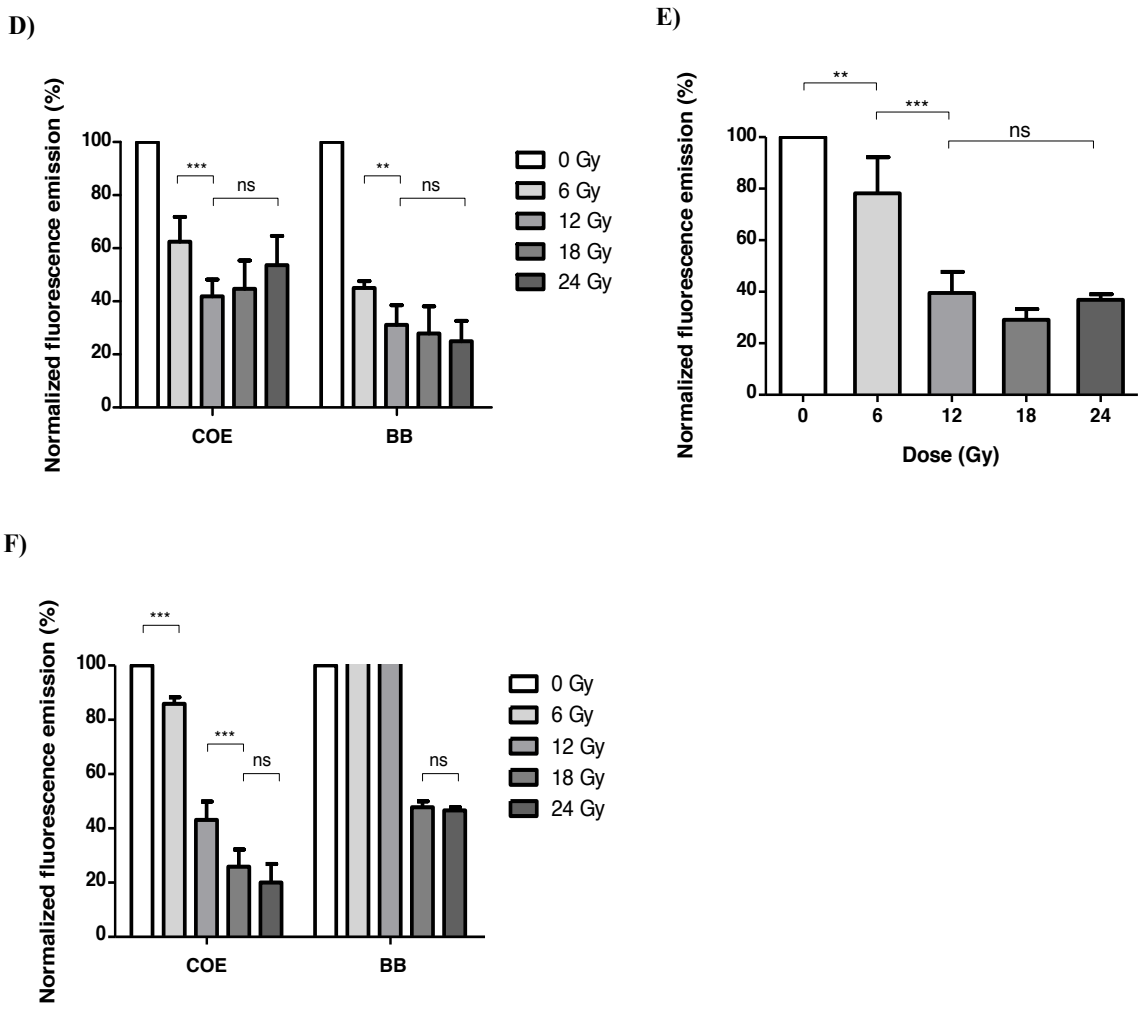

Figure 8.6. *Percentage of normalized cellular fluorescence emitted at 615 nm on D) day 3, E) day 6, and F) day 9 after COE and white BB irradiations. Note that E) corresponds only to clinical orthovoltage values. Doses ranged from 0 to 24 Gy.*

The QBlue assay performed at the fourth day after white BB irradiations (Figure 8.6-E) showed the same trend that QBlue measurements carried out at the sixth day after orthovoltage clinical-like exposures (Figure 8.6-E). The maximal cell recovery is achieved at 6 Gy of dose for both techniques. Despite this fact, further comparisons among them should be avoided since cells evaluated on day 6 after irradiations had indeed more time to recover than those analyzed on day 4 after treatment.

Comparisons between both radiation-based treatments could be performed by analyzing the QBlue normalized measurements performed on day nine (Figure 8.6-F). A complete cell recovery is observed for cells irradiated with BB at doses ≤ 12 Gy, as aforementioned in section 4.3. Within the same dose range (up to 12 Gy) a larger cell recovery is found for cells irradiated with orthovoltage clinical-like source. Therefore, these irradiations lead to an increased metabolic cell activity than those obtained with white synchrotron BB (Figure 8.6-F). The reason is that 12 Gy delivered by COE are above the endpoint found by flow cytometric analyses at around 6 Gy. By contrast, 12 Gy corresponds to the threshold dose for white BB synchrotron exposures.

It could be hypothesized that this higher cell recovery after clinical-like exposures may a consequence of its low dose rate. The reason is under low dose-rate RT conditions, the cell recovery from the sublethal damage is favored, mainly by NHEJ due to its relatively stable during all the cell cycle (Tomita *et al.* 2008). Nevertheless, the role of the energy spectrum must also be taken into account to analyze in a correct way the global cellular effects. In this frame, the low-energy COE would allow to deposit ~ 6 Gy instead of ~ 12 Gy (like in white BB irradiations) in order to produce a significant increase in the effectiveness of treatments in terms of DNA DSBs and cell survival.

Discussion

As it has already been explained through Introduction, parameters like beam energy, LET, dose rate, etc. lead to different biological responses and therefore to different RBE. It is well known that the RBE increases when the photon energy decreases (Mestres *et al.* 2008). At these low energies, photons interact with biological matter mainly through photoelectric process. As a result, a larger number of secondary particles of relatively high LET are generated, which are able to deposit their energy in/near to the DNA of tumor cells, which are able to induce a higher number of DSBs (Mestres *et al.* 2008) .

In fact, the COE used in the experiments had an energy spectrum ranging from 15 - 100 keV approximately, with a mean energy set at 35 keV. This was lower than the mean energy for white BB SR, which was set at 100 keV. Therefore, a larger photoelectric cross-section was expected to take place after these kV clinical-like irradiations, increasing the ratio of ionized water molecules which are present in the biological samples. As a consequence, a larger proportion of ROS molecules would arise as a product of these reactions, which can largely damage the DNA through diffusion in the tumor cells, leading to: i) higher γH2AX IF nuclear intensities, ii) larger proportion of early apoptotic cells, as previously observed in Results section.

Therefore, according to the results, it could be said that the RBE could increase after COE irradiations, increasing the biological effects at these decreased photon energies. The increase of cellular damage with COE in comparison with white BB SR means that less radiation dose (6 Gy for COE and 12 Gy for BB SR) is required to produce a given biological effect (Dale *et al.* 2008).

The dose-rate effect is crucial in radiotherapy since it is correlated to the sublethal repair damage during a long X-rays radiation exposure (Mayles *et al.* 2007, Mestres *et al.* 2008). At low dose rate, each cell that suffers a particle interaction will experience a larger delay before a second particle interact again enabling a major cell recovery during irradiation (Hall & Giaccia 2006, Mayles *et al.* 2007). Hence, lower RBE values are expected from these sources in terms of dose rate.

Indeed, so different dose-rate values between COE and BB SR do not seem to play an important role in the treatment effectiveness as one could have expected. Some effects such as a larger cell recovery could be detected after low dose-rate irradiations with orthovoltage clinical-like machine, since more sublethal damage can be repaired by NHEJ during the treatment (Tomita *et*

al. 2008). This would favor the larger percentage of apoptotic cells detected after orthovoltage clinical-like irradiations in comparison with BB SR.

The low energy for clinical-like irradiations would give cells slightly more damaged, and thus, with higher γH2AX IF nuclear intensities. However, due to the low dose rate of such irradiations they would also present a larger recovery ability. This would lead to obtain cells with moderate damage, which were more prone to undergo apoptosis.

CHAPTER V. Results: *In vivo* experiments

9 Dose tolerances of healthy rat brain to MBRT

Despite not to be the main responsible of this experiment, unlikely all those *in vitro*, I could participate on it, helping with irradiations and with the later immunochemistry labelling (not shown since it is still in progress).

Since thicker beams, such as minibeams, may lead to different biological responses than those observed with MRT (Uyama *et al.* 2011), an investigation regarding the effects of MBRT on healthy rat brains must be performed. For that aim, rats were irradiated at peak doses of 50, 100, 150, 200, 250 and 400 Gy. This last value was used in order to analyze the effects of doses as high as those used in MRT but in the MBRT configuration.

- Follow up of the animals:

The status of animals was controlled regularly. Rats were weighted twice per week from the third day after irradiations.

The gain of weight was larger for rats irradiated from 50 to 150 Gy of peak dose. All those rats were long survivors, without any sign of dose toxicity more than one year after MBRT irradiations. However, despite doses as high as 200 Gy led to an initial loss of weight in animals 10 days after MBRT exposures, a significant gain of weight was observed after that time, as it is depicted in Figure 9.1.

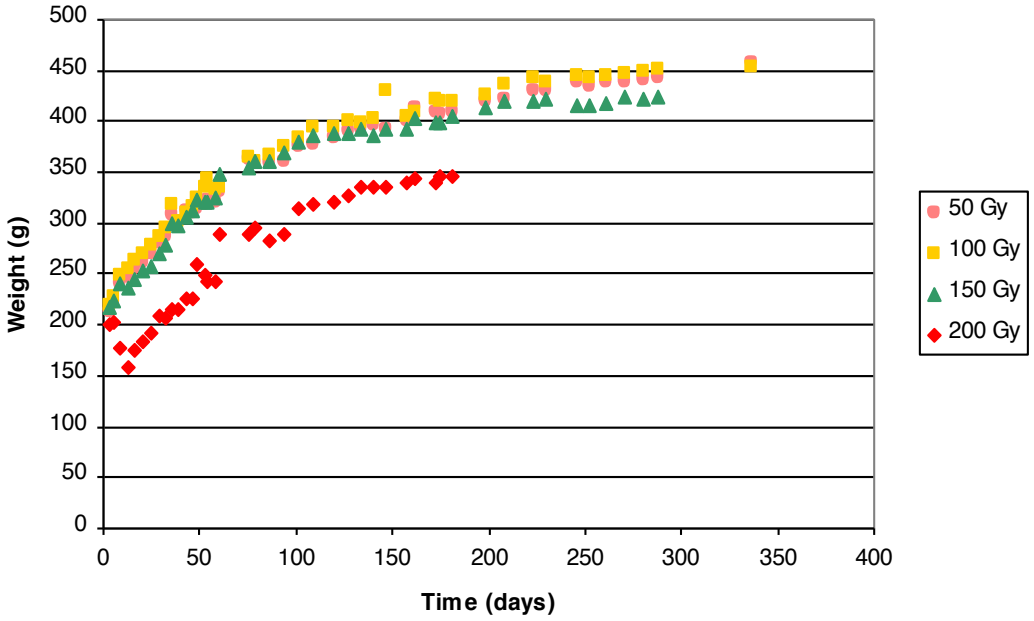

Figure 9.1. *Weight of animals (g) versus days after MBRT irradiations in a wide dose escalation range. The gain of weight was larger for rats irradiated at doses ≤ 150 Gy, which exhibited none symptom of dose toxicity.*

However, only one of the three animals that received 200 Gy was still alive 175 days after irradiations, which in addition showed hyperactivity in some moments. The other two rats were euthanized due to the symptoms of overdose exposure, such as apathy, incapacity to feed, etc.

- Survival curves:

The largest percentage of survival is achieved for peak doses up to 150 Gy (see Figure 9.2). In fact, all rats were alive 480 days after MBRT irradiations, exhibiting a good general state. Moreover, none sign of dermatitis was observed on the animal's skin, even after exposures of 400 Gy of peak dose.

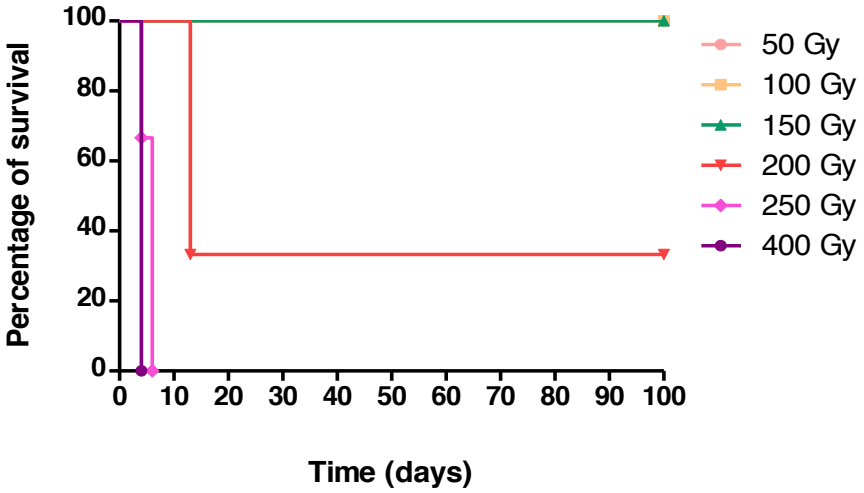

Figure 9.2. *Survival curves as a function of time for healthy rat brains irradiated with MBRT exposures from 50 to 400 Gy of peak dose.*

Irradiations at 200 Gy of peak dose led to a notable decrease of rats survival. Whereas doses as high as 250 and 400 Gy caused death in all rats few days after irradiations (Figure 9.2).

Thus, peak doses up to 150 Gy with MBRT exposures seem to be well tolerated for healthy rat tissues. Increasing peak doses of until 200 Gy begin to exhibit some toxicity on the healthy brain, whereas MBRT irradiations at higher doses are lethal for healthy rats.

Discussion

Although increasing the field size with respect to the thinner beams used in MRT, the tolerance doses of MBRT remains remarkably high. Peak doses up to 150 Gy delivered in one fraction seem to be well tolerated in healthy rats brain and no damages on those healthy tissues were indeed reported. This result is coherent with that obtained previously by Dilmanian *et al.* (2006) by studying unidirectional 0.68-mm thick minibeams, with a c-t-c distance of 1.36 mm and with a mean energy of 120 keV. This work showed that 170 Gy of peak dose were well tolerated for healthy rats brain. The small variations regarding the tolerance dose can be explained by the different MBRT configuration in both experiments. This might allow the use of higher and potentially curative doses in clinical cases where tissue tolerances are a limit for conventional methods. These doses achieved with MBRT configuration are more than one order of magnitude higher than those delivered with treatments based on stantard clinical treatments. For instance, the tolerance doses associated with a 50% injury rate within 5 years is 70 Gy for the skin, 60-70 Gy for the brain, and 40 Gy for the segmental bone marrow (Washington & Leaver 2009).

Recent investigations seem to point at the biological repair of the microscopic lesions by the minimally irradiated contiguous cells (Laissue *et al.* 1998, Dilmanian *et al.* 2001, 2007, Serduc *et al.* 2006) as the feasible explanation for the sparing healthy tissues of MRT and MBRT. Undamaged undifferentiated glial cells (like stem cells) in healthy tissues would migrate from the valley to peak regions several days after irradiations. Once there, those cells irradiated within the dose tolerance range could proliferate and differenciate leading to a complete tissue recovery several months later (Dilmanian *et al.* 2007). Migration and differentiation of the undifferentiated glial cells could be initiated by distant bystander effects from dying cells (Dilmanian *et al.* 2007). This fact could be explained by the hypothesis known as stem cell depletion (Yaes & Kalend 1988). This is based on the fact that for each organ it exists a limiting critical volume that can be repopulated by a single stem cell and for which damage can be repaired by repopulation. As a consequence, irradiations at doses below the tolerance limit for healthy tissues assures the complete recovery of these.

Peak dose of 150 Gy (10 Gy of valley dose) still remains insufficient against both F98 and 9L cell lines. According to our results, valley doses up to 18 Gy with MBRT irradiations are warranted to avoid any F98 cell recovery with time. For 9L treatments, 20 Gy of valley dose are required to achieve the same biological response. The interlacing of two arrays of orthogonal minibeams allows to deposite a higher dose in the tumor, while keeping the

tolerance dose in healthy tissues. Indeed, the interlacing of two arrays of 100 Gy of peak dose each one led to an ILS of 215%, whereas unidirectional irradiations at 150 and 180 Gy were in the limit of toxicity for healthy tissues (Prezado *et al.* 2012).

Thus, all these data pointed at MBRT to increase the therapeutic index of glioma treatments, specially by interlacing two arrays of beams, which allow to deposit curative doses in the tumor whilst keeping the healthy tissues within the tolerance doses (Prezado *et al.* 2012). Moreover, MBRT offers the advantage to be feasible its exportation to clinical equipments with the proper technical improvements.

CHAPTER VI. Final conclusions

10 Final conclusions and work diffussion

This Ph.D. thesis reports the first results obtained *in vitro* concerning the response of glioma cells to MBRT. The effects of MBRT were compared with those of white BB irradiations. New ways to increase the effectiveness of such irradiations by combining them with one of the most used chemotherapy compound as cisPt were investigated.

The main conclusions of this thesis are:

- **The endpoints for MBRT and BB were assessed.**

  The endpoint regarding direct damage on DNA and cell survival was established at 12 Gy of (valley) dose for both techniques. The endpoints concerning cell recover were observed at around 18 Gy for MBRT (valley dose) and BB. Hence, it appears essential to use several complementary techniques to study the effectiveness of a treatment.

  Despite the fact that the studied endpoints are comparable for both RT techniques, MBRT provides a higher effectiveness in terms of cell killing, specially through apoptosis. This higher percentage of cells undergoing apoptosis after MBRT is a consequence of the moderate- and long-term maintenance of damage, when the valley dose is equal or sensibly higher than the endpoint. Oppositely, cells placed at the beam paths die by necrosis due to the excess of damage.

  Therefore, the valley dose is a very important parameter in the effectiveness of MBRT. Moreover, the distribution of dose becomes more relevant that the dose by itself in terms of cell killing.

- To further enhance the effectiveness of white MBRT and BB, new combinations of chemo- and radiotherapy were investigated by using cisPt. A prior optimization of drug conditions was required. The main conclusions of such experiments are explained hereafter:

  The optimal parameters of cisPt were 7 µM of drug concentration and 24 h of incubation time.

The endpoint of the treatments based on cisPt 7 µM incubation followed by an irradiation (6 Gy), either at 81 keV or with MBRT, could be reduced in comparison with both radiations alone (12 Gy). CisPt administrtion prior RT led to decrease the percentage of living glioma cells, increasing the proportion of cells undergoing apoptosis.

The effectiveness of the treatment based on cisPt 7 µM was equivalent to that observed when the drug was administered concomitantly to 81 keV or MBRT irradiations at 6 Gy. That fact, together with the results obtained from Monte Carlo simulations, suggest that **Auger electrons do not play a significant role enhacing the dose deposition locally, and other synergic factors are involved in those treatments.**

- Deeper studies based on the cellular mechanisms of cisPt are requested to understand better those findings. In that framework, investigations on cisPt concentration and distribution were performed.

The concentration of Pt inside the cell nucleus analyzed by both ICP-MS and PIXE/BS techniques was found to be too much little to lead surviving cells to any dose enhancement with a subsequent irradiation.

The cisPt was found uniformly distributed inside the alive cells.

- Two strategies were investigated in order to reduce the cisPt cytotoxicity whilst keeping the effectiveness on tumor cells. The first one was to compensate the reduction in cisPt concentration by combining it with AuNPs:

The presence of of AuNPs provided a higher cell lethality via apoptosis after a subsequent irradiation with a monochromatic beam of 81 keV at doses of 6 Gy.

The combination of cisPt with AuNPs permitted to reduce significantly the concentration of cisPt (and therefore the cytotoxicity), while keeping a comparable level of effectiveness.

The second mechanism investigated was to deliver the cisPt into the cells associated to a lipidic vesicles called liposomes. The conclusions of these experiments, which are the first ones in analyzing the dead cells are:

To achieve a significant increase of Pt concentration inside the F98 dead cells, a cisPt-to-liposomes concentration ratio of around 1000 is requested according to both ICP-MS and PIXE/BS techniques.

A significant increase of the Ca-to-K content ratio was detected in dead cells when cisPt was associated to liposomes. **Moreover, all dead cells exhibited similar and high values of Zn.** That fact resembles the trend observed for Pt, indicating a direct relationship between these two metals through MT involved in detoxification of heavy metals, specially in the cytoplasm.

- MBRT not only seems to be more effective, but also exhibits sparing of the healthy tissue. This might allow the use of higher and potentially curative doses in clinical cases where tissue tolerances are a limit for conventional methods.

  One of the first *in vivo* experiments showed that peak doses up to 150 Gy delivered in one single fraction seemed to be well tolerated in healthy rats brain. The histological analysis must be concluded.

- The comparison of the cell damage after irradiations with a COE and with synchrotron sources led to the next conclusions:

  Slightly higher amount of cell damage was obtained after irradiations with a COE, since lower threshold doses were needed to reach the same biological effect with respect to BB irradiations. That could be a consequence of the larger cellular damage provided by both direct and indirect effects of radiation at those lower energies, which led to a larger percentage of apoptotic cells detected after orthovoltage clinical-like irradiations in comparison with BB SR.

  A larger cell recovery was detected after low dose-rate irradiations with COE, since more sublethal damage could be repaired by NHEJ during the treatment. Nevertheless, dose rate dose not seem to play a major role.

In summary, the objectives accomplished in this thesis have provided the first insight look at cellular effects of new synchrotron-based RT techniques. I was able to establish the therapeutic doses needed to kill the glioma cells, and possible ways to improve the therapeutic index were investigated.

These results joined to the high tissue sparing observed *in vivo* makes MBRT a very promising RT technique to be explored, with the asset that it has the potential to be extended outside synchrotrons.

Further studies will include to assess the effect of MBRT in different normal and tumor tissues, as well as new combinations of chemo-radiotherapy.

Part of the results of this Ph.D. dissertation have been compiled in five publications:

1- Gil, S., Fernández, M., Prezado, Y., Biete, A., Bravin, A. & Sabés, M. (2011). Synchrotron radiation in cancer treatments and diagnostics: an overview. *Clin. Transl. Oncol.* **13**:715-720.

2- Gil, S., Prezado, Y. & Sabés, M. (2012). Double-strand breaks on F98 glioma rat cells induced by minibeam and broad-beam synchrotron radiation therapy. *Manuscript submitted to J. Synchrotron Rad.*

3- Gil, S., Sarun, S., Biete, A., Prezado, Y. & Sabés, M. (2011). Survival analysis of F98 glioma rat cells following minibeam or broad-beam synchrotron radiation therapy. *Rad. Oncol.* **6**:37-45.

4- Prezado, Y., Sarun, S., Gil, S., Deman, P., Bouchet, A. & Le Duc, G. (2012). Increase of lifespan for glioma-bearing rats by using minibeam radiation therapy. *J. Synchrotron Rad.* **19**:60-65. **(Featured article according to the editor's choice).**

In addition, I was able to present part of my results:

- Oral communication: "*In vitro* radiotherapy experiments with Synchrotron Radiation" (2009): AUSE workshop at the UAB *(Barcelona, Spain)*.

- Poster: "*In vitro* treatments based on irradiations with D3100 Gulmay superficial radiotherapy against glioma" (2010): 29th ESTRO *(Barcelona, Spain)*.

- Poster: "Complementary data analysis for chemo-radiotherapy treatments with synchrotron against *in vitro* F98 glioma rat cells" (2010): MASR workshop (*Melbourne, Australia)*.

- Oral communication: "The multiple effects of Minibeam Radiation Therapy on F98 glioma rat cells" (2011): AUSE workshop at the *Universidad de Valencia, (Valencia, Spain)*.

- Poster: "Nano-X-ray fluorescence imaging of Pt in F98 glioma rat cells" (2011): AUSE workshop at the *Universidad de Valencia (Valencia, Spain)*. (**The poster was awarded as the second best project in the workshop).**

- Oral communication: "*In vitro* treatments with Synchrotron Radiation Therapy on F98 glioma rat cells" (2011): Clinical sessions at the *Hospital Clínic de Barcelona, (Barcelona, Spain).*

APPENDICES

- **A. 1: Monte Carlo simulations to evaluate the possible dose enhancement of monochromatic irradiations in presence of Pt 7 µM**

The dose deposited on the cells was assessed by using the PENELOPE 2006 code for coupled electron-photon transport developed by F. Salvat *et al*. (2003) at the University of Barcelona (UB). See section 2.2.1 of "Materials and methods" for further details of the program.

PENELOPE has been already tested for radiation transport in condensed matter within the micrometric escale (Bernal & Liendo 2009). To determine the energy deposited on cells, a 24-well plate and the medium were modeled (see Figure A.1.1) by using the geometry package in PENELOPE.

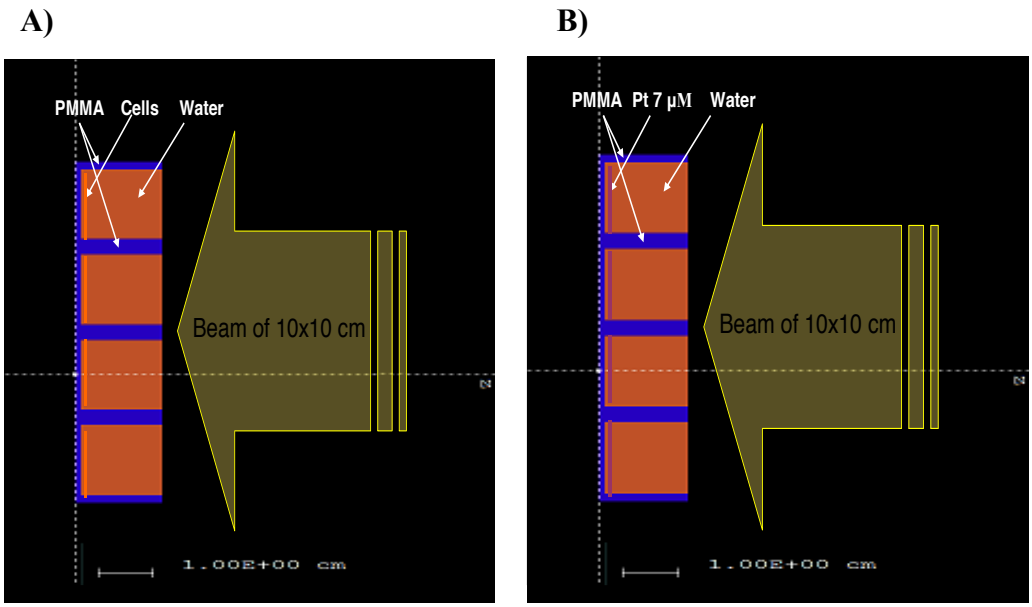

Figure A.1.1. *Representation of the geometry used for the simulation performed with PENELOPE based on a partial 24-well plate where A) cells (represented as water) and B) Pt 7 µM were set at the bottom. The monochromatic beam covered a field of 10 cm of wide x 10 cm of length.*

The simulations were performed using 10^9 photons as primary particles. The beam energy was 79 keV. The simulation parameters were also identical for the three materials: i) the absortion energy was set at 100 eV, ii) the elastic scattering parameters for secondary particles were set both at 1 keV, and iii) the cut-off energy losses for inelastic collisions and bremsstrahlung emission were established at 5 and 10 keV respectively. Doses were tallied in voxels of 1 µm along the direction of X and Y, and 0.002 µm along Z (parallel to the beam's direction).

The first simulation was done with a monochromatic beam of 79 keV without cisPt. After changing the geometry field, the subsequent simulation was performed to evaluate the effect of irradiating Pt (= cisPt) 7 μM instead of water at energy of 79 keV.

The dose enhacement factor (DEF) was calculated after both simulations. For that, the energy deposited on the cell region after irradiations in presence of Pt 7 μM was divided by the energy deposited on the same region but in absence of Pt, i.e., only with H_2O. The values obatined are reported in Table A.1.1.

Cellular conditions	*Deposited Energy (eV ± SD)*	***DEF***
H_2O	$3.35 \cdot 10^{-2} \pm 2.4 \cdot 10^{-3}$	-
Pt 7 μM	$3.36 \cdot 10^{-2} \pm 2.4 \cdot 10^{-3}$	$\mathbf{1.003 \pm 2.4 \cdot 10^{-3}}$

Table A.1.1. *DEF calculated from the energy deposited on water (equivalent to cells) and on Pt 7 μM (equivalent to cells treated with cisPt at this concentration) after irradiations at 79 keV.*

Since the DEF is negligible, it can be assumed that treatments based on the administration of cisPt at concentration of 7 μM (assuming uniform distribution of Pt) followed by a synchrotron irradiation at 79 keV do not cause any dose enhancement in cells. Moreover, the so-slightly increase of 2 keV up to 81 keV, like in the experiments described in section 6, is expected to keep the DEF value constant at around 1 at those metals concentrations.

Therefore, the effectiveness of those chemotherapeutic treatments based on such small concentrations can not be explained by any dose enhancement due to the emission of Auger electrons as previously predicted (Bencokova *et al.* 2007).

- A. 2: A kinetic study of the cell response to radiation

This work was performed in order to find the optimal time after irradiations to analyze the different cell populations arising, i.e., living, early apoptotic and dead cells. For that purpose, a kinetic study was performed with the F98 cell line. Cells were cultured in 24-well plates as explained in section 2.1.1. After that time, cells were irradiated at 12 Gy with a COE because of its wider availability. This dose was chosen since it is above the endpoint (6 Gy approximately). Therefore dead cell populations could detected in an easier way.

The subsequent flow cytometries were performed at least by triplicate at several times (ranging from 1.5 to 48 h) after irradiations. Untreated controls were analyzed in parallel to each irradiation. No differences were detected among them according to both the cell population and the time (data not shown).

- Results:

The percentage of normalized living cells at different points after 12 Gy of COE irradiations is represented in **Figure A.2.1**.

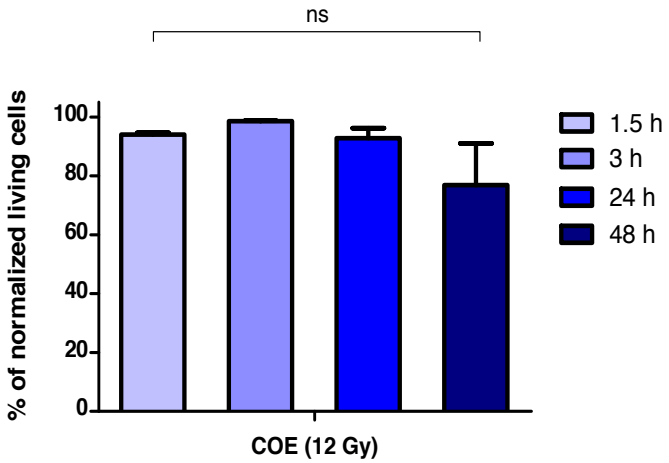

Figure A.2.1. *Percentage (%) of normalized living cells after COE irradiations at 12 Gy ranging from 1.5 to 48 h.*

No difference on cell survival ration could be detected among times. Nevertheless, the error bar at 48 h could hide a decreased cell survival percentage (see **Table A.2.1**).

Time (h)	*% of normalized surviving cells after COE (Mean % ± SD)*
1.5	94.1 ± 0.5
3	98.6 ± 0.2
24	93 ± 4
48	77 ± 14

Table A.2.1. *Percentages (%) of normalized values for surviving cells analyzed by flow cytometry at different times after COE irradiations at 12 Gy. These data are graphically represented in histograms in Figure A.2.1.*

The percentage of cells undergoing early apoptosis at different times after COE exposures is small, as it was already observed in section 8.2 of results (Figure A.2.2). In addition, any difference can be yet detected among post-irradiation times as it is reported in Table A.2.2.

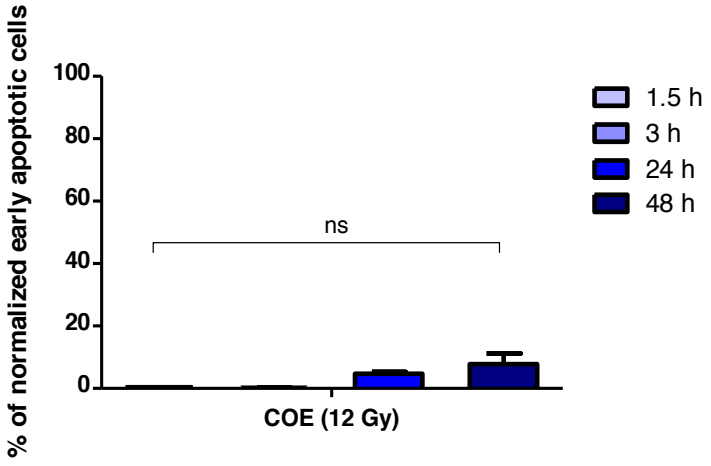

Figure A.2.2. *Percentage (%) of normalized early apoptotic cells after COE irradiations at 12 Gy ranging from 1.5 to 48 h.*

Time (h)	*% of normalized early apoptotic cells after COE (Mean % ± SD)*
1.5	0.4 ± 0.0
3	0.2 ± 0.0
24	4.7 ± 0.5
48	8 ± 3

Table A.2.2. *Percentages (%) of normalized values for early apoptotic cells analyzed by flow cytometry at different times after COE irradiations at 12 Gy. These data are graphically represented in histograms in Figure A.2.2.*

Regardless of the post-irradiation time, the normalized percentage of cells undergoing late apoptosis and necrosis was higher than apoptotic ones (see Figure A.2.3).

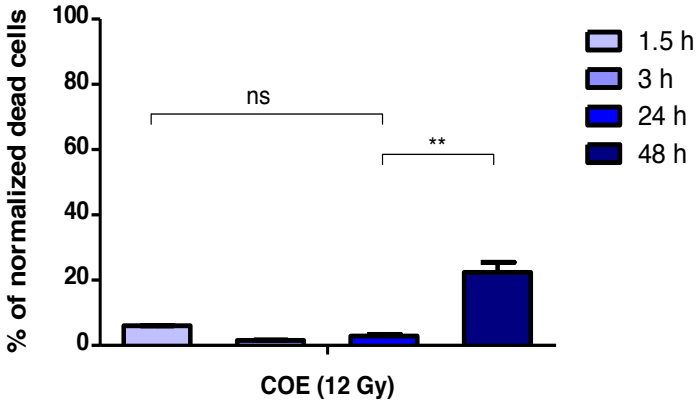

Figure A.2.3. *Percentage (%) of normalized dead cells after COE irradiations at 12 Gy ranging from 1.5 to 48 h.*

The only difference could be detected above 24 h (see Table A.2.3). In particular, 48 h seems to be the optimal time in order to perform the flow cytometric analyses due to the remarkable increased proportion of dead cells.

Time (h)	*% of normalized early apoptotic cells after COE (Mean % ± SD)*
1.5	6.0 ± 0.1
3	1.6 ± 0.1
24	2.9 ± 0.5
48	22 ± 3

Table A.2.3. *Percentages (%) of normalized values for early apoptotic cells analyzed by flow cytometry at different times after COE irradiations at 12 Gy. These data are graphically represented in histograms in Figure A.2.3.*

All the aforementioned results are obviously in the frame with those corresponding to 12 Gy described in section 8.2 of Results.

Despite the percentage of each cell population will vary according to the irradiation mode, the larger proportion of dead cells is expected 48 h after any irradiation. For this reason all flow cytometries explained through this work were carried out at that time.

REFERENCES

References

Adam, J.F., Elleaume, H., Joubert, A., Biston, M.C., Charvet, A.M., Balosso, J., Le Bas, J.F. & Estève, F. (2003). *Int. J. Radiat. Oncol. Biol. Phys.* **57**:1413-1426.

Adam, J.F., Biston, M.C., Joubert, A., Charvet, A.M., Le Bas, J.-F., Estève, F. & Elleaume, H. (2005*a*). *Int. J. Radiat. Oncol. Biol. Phys.* **61**:1173-1182.

Adam, J.F., Nemoz, C., Bravin, A., Fiedler, S., Bayat, S., Monfraix, S., Berruyer, G., Charvet, A.M., Le Bas, J.-F., Elleaume, H. & Estève., F (2005*b*). *J. Cereb. Blood Flow Metab.* **25**:145-153.

Adam, J.F., Joubert, A., Biston, M.C., Charvet, A.M., Peoc'h , J.F., Le Bas, J.F., Balosso, J., Estève, F. & Elleaume, H. (2006). *Int. J. Radiat. Oncol. Biol. Phys.* **64**:603-611.

Adam, J.F., Biston, M.C., Rousseau, J., Boudou, C., Charvet, A.M., Balosso, J., Estève, F. & Elleaume, H. (2008). *Phys. Med.* **24**:92-97.

Amirlak, B. & Couldwell, W.T. (2003). *J. Neurooncol.* **63**:129-145.

Astor, M.B., Hilaris, B.S., Gruerio, A., Varricchione, T. & Smith, D. (2000). *Int. J. Radiat. Oncol. Biol. Phys.* **47**:809-813.

Banáth, J.P., MacPhail, S.H. and Olive, P.L. (2004). *Cancer Res.* **64**:7144-7149.

Barth, R.F. (1998). *J. Neurooncol.* **36**:91-102.

Barth, R.F., Coderre, J.A., Vicente, M.G.H. & Blue, T.E. (2005). *Clin. Cancer Res.* **11**:3987-4002.

Baruchel, J., Cloetens, P., Härtwig, J., Ludwig, W., Mancini, L., Pemot, P. & Schlenker, M. (2000). *J. Synchrotron Rad.* **7**:196-201.

Behin, A., Hoang-Xuang, K., Carpentier, A.F. & Delattre, J.Y. (2003). *Lancet Oncol.* **361**:323-331.

Beier, D., Röhrl, S., Deepu, R., Schwarz, S., Kunz-Schughart, L.A., Leukel, P., Proescholdt, M., Brawanski, A., Bogdahn, U., Trampe-Kieslich, A., Giebel, B., Wischhusen, J., Reifenberger, G., Hau, P. & Beier, C.P. (2008). *Cancer Res.* **68**:5706-5715.

Belyaev, I.Y. (2010). *Mutat. Res*. **704**:132-141.

Bencokova, Z., Balosso, J. & Foray, N. (2007). *J. Synchrotron Rad.* **15**:74-85.

Bernal, M.A. & Liendo, J.A. (2009). *Med. Phys.* **36**:620-625.

Biston, M.C., Joubert, A., Adam, J.F., Elleaume, H., Bohic, S., Charvet, A.-M., Estève, F., Foray, N. & Balosso, J. (2004). *Cancer Res.* **64**:2317:2323.

Biston, M.C., Joubert, A., Charvet, A.-M., Balosso, J. & Foray, N. (2009). *Cancer Res.* **172**:348:358.

Bosselmann, S. & Williams, R.O. III. (2012). *Drug Dev. Ind. Pharm.* **38**:158-170.

Boudou, C., Balosso, J., Estève, F. & Elleaume, H. (2005). *Phys. Med. Biol.* **50**:4841-4851.

Brahme, A. (2004). *Int. J. Radiat. Oncol. Biol. Phys.* **58**:603-616.

Bräuer-Krisch, E., Requardt, H., Brochard, T., Berruyer, G., Renier, M., Laissue, J.A. & Bravin, A. (2009). *Rev. Sci. Instrum.* **80**:74301-1-74301-6.

Callisen, H.H., Norman, A. & Adams, F.H. (1979). *Med. Phys.* **6**:504-509.

Carmona, A., Devès, G. & Ortega, R. (2008). *Anal. Bioanal. Chem.* **390**:1585-1594.

Casals, E., Pfaller, T., Duschl, A., Oostingh, G.J. & Puntes, V. (2010). *ACS Nano.* **4**:3623-3632.

Chen, T.-C., Lai, K.-C., Yang, J.-S., Liao, C.-L., Hsia, T.-C., Chen, G.W., Lin, J.-J, Lin, H.-J., Chiu, T.-H., Tang, Y.-J. & Chung, J.-G. (2009). *Int. J. Oncol.* **34**:1681-1690.

Cherry, P. & Duxbury, A. (1998). *Practical Radiotherapy*. London (United Kingdom): Greenwich Medical Media Ltd.

Corde,S., Biston, M.C., Elleaume, H., Estève, F., Charvet, A.M., Joubert, A., Ducros, V., Bohic, S., Simionovici,A., Brochard, T., Nemoz, C., Troprès, I., Fiedler, S., Bravin, A., Thomlinson, W., Le Bas, J.F. & Balosso, J. (2002). *Radiat. Res.* **158**:763-770.

Corde, S., Balosso, J., Elleaume, H., Renier, M., Joubert, A., Biston, M.C., Adam, J.F., Charvet, A.-M., Brochard, T., Le Bas, J.F, Estève, F. & Foray, N. (2003). *Cancer Res.* **63**:3221-3227.

Costes, S.V., Boissiere, A., Ravani, S., Romano, R., Parvin, B. & Barcellos-Hoff, M.H. (2006). *Radiat. Res.* **165**:505-515.

Curtis, H.J. (1967). *Radiat. Res. Suppl.* **7**:250-257.

Dale, R.G., Jones, B. & Cárabe-Fernández, A. (2009). *Appl. Radiat. Isot.* **67**:387-392.

Darzynkiewicz, Z., Juan, G., Li, X., Gorkzyca, W., Murakami, T. & Traganos, F. (1997). *Cytometry* **27**:1-20.

De Jong, W.H., Hagens, W.I., Krystek, P., Burger, M.C., Sips, A.J.A.M. & Geertsma, R.E. (2008). *Biomaterials* **29**: 1912-1919.

Deman, P., Vautrin, M., Stupar, V., Barbier, E.L., Elleaume, H., Esteve, F. & Adam, J.F. (2011). *Phys. Med. Biol.* **56**:4465-4480.

Dilmanian, F.A., Morris, G.M., Le Duc, G., Huang, X., Ren, B., Bacarian, T., Allen, J. C., Kalef-Ezra, J., Orion, I., Rosen, E.M., Sandhu, T., Sathé, P., Wu, X.Y., Zhong, Z. & Shivaprasad, H.L. (2001). *Cell. Mol. Biol.* **47**:487-493.

Dilmanian, F.A., Button, T.M., Le Duc, G., Zhong, N., Pena, L.A., Smith, J.A.L., Martinez, S.R., Bacarian, T., Tammam, J., Ren, B., Farmer, P. M., Kalef-Ezra, J., Micca, P.L., Nawrocky, M.M., Nieder, J.A., Recksieck, F.P., Fuchs, A. & Rosen, E.M. (2002). *J. Neurooncol.* **4**:26-38.

Dilmanian, F.A., Morris, G.M., Zhong, N., Bacarian, T., Hainfeld, J.F., Kalef-Ezra, J., Brewington, L.J., Tammam,J. & Rosen, E.M. (2003). *Radiat. Res.* **159**:632-641.

Dilmanian, F.A., Zhong, Z., Bacarian, T., Benvenlste, H., Romanelli, P., Wang, R., Welwart, J., Yuasa, T., Rosen, E.M. & Anschel, D.J. (2006). *Proc. Natl. Acad. Sci. U.S.A.* 103:9709-9714.

Dilmanian, F.A., Qu, Y., Feinendegen, L.E., Peña, L.A., Bacarian, T., Henn, F.A., Kalef-Ezra J., Liu, S., Zhong, Z. & McDonald, J.W. (2007). *Exp. Hematol.* **35**:69-77.

Duzgunes, N. (2003). *Methods in Enzymology. Liposomes.* **367A**. California, (USA): Elsevier Academic Press.

Edouard, M., Broggio, D., Prezado, Y., Estève, F., Elleaume, H. & Adam, J.F. (2010). *Med. Phys.* **37**:2445-2456.

Faichild, R.G. & Bond, V.P. (1984). *Strahlentherapie* **160**:758-763.

Fortin-Ripoche, J.-P., Martina, M.S., Gazeau, F., Ménager, C., Wilhem, C., Bacri, J.-C., Lesieur, S. & Clément, O. (2006). *Radiology* **239**:415-424.

Friedman, H.S., Kerby, T. & Calvert, H. (2000). *Clin. Cancer Res.* **6**:2585-2597.

Gorczyca, W. (1997). *Endocrine-Related Cancer* **6**:17-19.

Hainfeld, J.F., Slatkin, D.N. & Smilowitz, H.M. (2004). *Phys. Med. Biol.* **49**:N309-N315.

Hainfeld, J.F., Slatkin, D.N., Focella, T.M. & Smilowitz, H.M. (2006). *Br. J. Radiol.* **79**:248-253.

Hainfeld, J.F., Dilmanian, F.A., Zhong, Z., Slatkin, D.N., Kalef-Ezra, J.A. & Smilowitz, H.M. (2010). *Phys. Med. Biol.* **55**:3045-3059.

Hall, E.J. & Giaccia, A.J. (2006). *Radiobiology for the Radiologist*, 6th edition. Philadelphia (USA): Lippincott Williams & Wilkins.

Huang, X., Okafuji, M., Traganos, F., Luther, E., Holden, E. & Darzynkiewicz, Z. (2004). *Cytometry A* **58A**:99-110.

Huang, X., Halicka, D., Traganos, F., Tanaka, T., Kurose, A. & Darzynkiewicz, Z. (2005). *Cell Prolif.* **38**:223-243.

Huang, X. & Darzynkiewicz, Z. (2006). *Methods Mol. Biol.* **314**:73-80.

IAEA-TRS-461. (2008). *Relative biological effectiveness in ion beam therapy.* Technical Report, International Atomic Energy Agency. Vienna (Austria).

Iwamoto, K.S., Norman, A., Kagan, A.R., Wollin, M., Olch, A., Bellotti, J., Ingram, M. & Skillen, R.G. (1990). *Radiother. Oncol.* **19**:337-343.

Iwamoto, K.S., Norman, A., Freshwater, D.B., Ingram, M. & Skillen, R.G. (1993). *Radiother. Oncol.* **26**:76-78.

Jackson, J.D. (1998). *Classical electrodynamics*, 3rd edition. New York (USA): John Wiley and Sons.

Jamieson, E.R. & Lippard, S.J. (1999). *Chem. Rev.* **99**:2467-2498.

Jane, E.P. & Pollack, I.F. (2010). *Eur. J. of Cancer* **46**:412-419.

Karnas, S.J., Yu, E., McGarry R.C. & Battista, J.J. (1999). *Phys. Med. Biol.* **44**:2537-2549.

Kartalou, M. & Essingmann, J.M. (2001). *Mutat. Res.* **478**:1-21.

Kataoka, Y., Bindokas, V.P., Duggan, R.C., Murley, J.S. & Grdina, D.J. (2006). *J. Radiat. Res.* **47**:245-257.

Laissue, J.A., Geiser, G., Spanne, P.O., Dilmanian, F.A., Gebbers, J.-O., Geiser, M., Wu , X.-Y., Makar, M.S., Micca, P.L., Nawrocky, M.M., Joel, D.D. & Slatkin, D.N. (1998). *Int. J. Cancer* **78**:654-660.

Laissue, J.A., Lyubimova, N., Wagner, H.P., (1999). *SPIE* **3770**:38-45.

Lawrence, Y.R., Li, X.Q., El Naqa, I., Hahn, C.A., Marks, L.B., Merchant, T.E. & Dicker, A.P. (2010). *Int. J. Radiat. Oncol. Biol. Phys.* **76**:S20-S27.

Legler, J.M., Ries, L.A., Smith, M.A., Warren, J.L., Heineman, E.F., Kaplan, R.S. & Linet, M.S. (1999). *J. Natl. Cancer Inst.* **91**:1382-1390.

Lengeler, B. (2001). *Naturwissenschaften* **88**:249-260.

Ling, C.C., Guo, M., Chen, C.H. & Deloherey, T. (1995). *Cancer Res.* **55**:5207-5212.

Löbrich, M., Shibata, A., Beucher, A., Fisher, A., Ensminger M., Goodarzi, A.A., Barton, O. & Jeggo, P.A. (2010). *Cell Cycle* **9**:662-669.

Mah, L.J., Orlowski, C., Ververis, K., Vasireddy, R.S., El-Osta, A. & Karagiannis, T.C. (2011). *Genome Integr.* **2**:3-14.

Marková, E,. Schultz, N. & Belyaev, I.Y. (2007). *Int. J. Radiat. Biol.* **83**:319-329.

Martinez-Criado, G., Tucoulou, R., Cloetens, P., Bleuet, P., Bohic, S., Cauzid, J., Kieffer, I., Kosior, E., Labouré, S., Petitgirard, S., Rack, A., Sans, J.A., Segura-Ruiz, J., Suhonen, H., Susini, J. & Vilanova, J. (2012). *J. Synchrotron Radiat.* **19**:10-18.

Martínez-Rovira, I., Sempau, J., Fernández-Varea, J.M., Bravin, A. & Prezado, Y. (2010). *Phys. Med. Biol.* **55**:4375-4388.

Martínez-Rovira, I. & Prezado, Y. (2011). *Phys. Med.* **38**:4430-4439.

Mayles, P., Nahum, A. & Rosenwald, J.C. (2007). *Handbook of Radiotherapy Physics*. Florida (USA): Taylor & Francis Group.

Menichetti, L., Gaetano, L., Zampolli, A., Del Turco, S., Ferrari C., Bortolussi, S., Stella, S., Altieri, S., Salvadori, P.A. & Cionini, L. (2009). *S. Appl. Radiat. Isot.* **67**:S336-S340.

Mesa, A.V., Norman, A., Solberg, T.D., Demarco, J.J. & Smathers, J.B. (1999). *Phys. Med. Biol.* **44**:1955-1968.

Mestres, M., Caballín, M.R., Barrios, L., Ribas, M. & Barquinero, J.F. (2008). *Radiat. Res.* **170**:93-100.

Meyn, R.E., Stephens, L.C., Hunter, N.R., Ang, K.K. & Milas, L. (1994). *Int. J. Radiat. Oncol. Biol. Phys.* **30**:619-624.

Nguyen, D. X. & Massagué, J. (2007). *Nature Rev. Genet.* **8**:341-352.

Nikjoo, H., Emfietzoglou, D. & Charlton, D.E. (2008). *Int. J. Radiat. Biol.* **84**:1011-1026.

Nishikawa, R. (2010). *Neurol. Med. Chir.* **50**:713-719.

Norman, A., Ingram, M., Skillen, R.G., Freshwater, D.B., Iwamoto, K.S. & Solberg, T. (1997). *Radiat. Oncol. Invest.* **5**:8-14.

O'Brien, J., Wilson, I., Orton, T. & Pognan, F. (2000). *Eur. J. Biochem.* **267**:5421-5426.

Olive, P.L. & Durand, R.E. (1997). *Int. J. Radiat. Biol.* **71**:695-707.

Olive, P.L. (2011). *Radiother. Oncol.* **101**:18-23.

Olivier, D., Douillard, S., Lhommeau, I. & Patrice, T. (2009). *Radiat. Res.* **172**:451-462.

Ortega, R., Moretto, P., Fajac, A., Bénard, J., Llabador, Y. & Simonoff, M. (1996). *Cell. Mol. Biol.* **42**:77-88.

Ortega, R., Devès, G. & Carmona, A. (2009). *J. R. Soc. Interface* **6**:S649-S658.

Paciotti, G.F., Kingston, D.G.I. & Tamarkin, L. (2006). *Drug Dev. Res.* **67**:47-54.

Paull, T.T., Rogakou, E.P., Yamazaki, V., Kirchgessner, C.U., Gellert, M. & Bonner, W.M. (2000). *Curr. Biol.* **10**:886-895.

Poncelet, B.P., Wedeen, V.J. Weisskoff, R.M. & Cohen, M.S. (1992). *Radiology* **185**:645-651.

Prezado, Y., Fois, G., Edouard, M., Nemoz, C., Renier, M., Requardt, H., Estève, F., Adam, J.F., Elleaume, H. & Bravin, A. (2009*a*). *Med. Phys.* **36**:725-733.

Prezado, Y., Thegumpallil, S., Renier, M. & Bravin, A. (2009*b*). *Med. Phys.* **36**:4897-4902.

Prezado, Y., Fois, G., Le Duc, G. & Bravin, A. (2009*c*). *Med. Phys.* **36**:3568-3574.

Prezado, Y., Renier, M. & Bravin, A. (2009*d*). *J. Synchrotron Rad.* **16**:582-586.

Prezado, Y., Martínez-Rovira, I., Thegumpallil, S. & Deman, P. (2011). *Med. Phys.* **38**:5012-5019.

Prezado, Y., Sarun, S., Gil, S., Deman, P., Bouchet, A., & Le Duc, G. (2012). *J. Synchrotron Rad.* **19**:60-65.

Regnard, P., Le Duc, G., Bräuer-Krisch, E., Troprès, I., Siegbahn, E.A., Kusak, A., Clair, C., Bernard, H., Dallery, D., Laissue, J.A. & Bravin, A. (2008). *Phys. Med. Biol.* **53**:861-878.

Renier, M., Brochard, T., Nemoz, C., Requardt, H., Bräuer-Krisch, E., Estève, F., Balosso, J., Suortti, P., Baruchel, J., Elleaume, H., Barruyer, G., Berkvens, P. & Bravin, A. (2008). *Eur. J. Radiol.* **68S**:S147-S150.

Revet, I., Feeney, L., Bruguera, S., Wilson, W., Dong, T.K., Oh, D.H., Dankort, D. & Cleaver, J.E. (2011). *Proc. Natl. Acad. Sci.* **108**:8663-8667.

Rogakou, E.P., Boon, C., Redon, C. & Bonner, W.M. (1999). *J. Cell. Biol.* **146**:905-916.

Roos, W.P. & Kaina, B. (2006). *Trends Mol. Med*. **12**:440-450.

Rose, J.H., Norman, A., Ingram, M., Aoki, C., Solberg, T. & Mesa, A. (1999). *Int. J. Radiat. Oncol. Biol. Phys*. **45**:1127-1132.

Rousseau, J., Barth, R.F., Fernandez, M., Adam, J.-F., Balosso, J., Estève, F. & Elleaume, H. (2010). *J. Neurooncol.* **98**:287-295.

Salvat, F., Fernández-Varea, J.M. & Sempau, J. (2003). *OECD Nuclear Energy Agency (Issy-les-Molineaux-France), [http://www.nea.fr]*.

Santos-Mello, R., Callisen, H.H., Winter, J., Kagan, A.R. & Norman, A. (1983). *Med. Phys.* **10**:75-78.

Serduc, R., Pascale, V., Vial, J.-C., Farion, R., Rocas, L., Rémy, C., Fadlallah, T., Bräuer E., Bravin, A., Laissue, J., Blattmann, H. & van der Sanden, B. (2006). *Int. J. Radiat. Oncol. Biol. Phys.* **64**:1519-1527.

Serduc, R., Christen, T., Laissue, J., Farion, R.,Bouchet, A., van der Sanden, B., Segebarth, C., Bräuer-Krisch, E., Le Duc, G., Bravin, A., Rémy, C. & Barbier E.L. (2008). *Phys. Med. Biol.* **53**:3609-3622.

Serduc, R., Bouchet, A., Bräuer-Krisch, E., Laissue, J.A., Spiga, J., Sarun, S., Bravin, A., Fonta, C., Renaud, L., Boutonnat, J., Siegbahn, E.A., Estève, F. & Le Duc, G. (2009). *Phys. Med. Biol.* **54**:6711-6724.

Serrano, F.A., Matsuo, A.L., Monteforte, P.T., Bechara, A., Smaili, S.S., Santana, D.P., Rodrigues, T., Pereira, F.V., Silva, L.S., Machado Jr., J., Santos, E.L., Pesquero, J.B.,

Martins, R.M., Travassos, L.R., Caires, A.C.F. & Rodrigues, E.G. (2011). *BMC Cancer* **11**:296-311.

Seymour, C.B., Mothersill, C. & Alper, T. (1986). *Int. J. Radiat. Biol.* **50**:167-197.

Siegbahn, E.A., Stepanek, J., Bräuer-Krisch, E. & Bravin, A. (2006). *Med. Phys.* **33**:3248-3259.

Slatkin, D.N., Spanne, P., Dilmanian, F.A. & Sandborg, M. (1992). *Med. Phys.* **19**:1395-1400.

Slatkin, D.N., Spanne, P., Dilmanian, F.A., Gebbers, J.-O. & Laissue, J.A. (1995). *Proc. Natl. Acad. Sci. USA* **92**:8783-8787.

Sneed, P.K., McDermott, M.W. & Gutin, P.H. (1997). *Semin. Surg. Oncol.* **13**:157-166.

Solé, V.A., Papillon, E., Cotte, M., Walter, P. and Susini, J. (2007). *Spectrochim. Acta Part B* **62**:63-68.

Stupp, R., Mason, W.P., van den Bent, M.J., Weller, M., Fisher, B., Taphoorn, M.J.B., Belanger, K., Brandes, A.A., Marosi, C., Bogdahn, U., Curschmann, J., Janzer, R.C., Ludwin, S.K., Gorlia, T., Allgeier, A., Lacombe, D., Cairncross, J.G., Eisenhauer, E. & Mirimanoff, R.O. (2005). *N. Engl. J. Med.* **352**:987-996.

Stupp, R., Hegi, M. & Weller, M. (2010*a*). *Expert. Rev. Anticancer Ther.* **10**:1675-1677.

Stupp, R., Tonn, J.-C., Brada, M. & Pentheroudakis, G. (2010*b*). *Ann. Onco l. (Suppl. 5).* **21**:190-193.

Suortti, P. & Thomlinson, W. (2003). *Phys. Med. Biol.* **48**: R1-R35.

Thirumoorthy, N., Manisenthil Kumar, K.T., Shyam Sundar, A., Panayappan, L. & Chatterjee, M. (2007). *World J. Gastroenterol.* **13**:993-996.

Tomita, M., Morohoshi, F., Matsumoto, Y., Otsuka, K. & Sakai, K. (2008). *J. Radiat. Res.* **49**, 557-564.

Uyama, A., Kondoh, T., Nariyama, N., Umetani, K., Fukumoto, M., Shinohara, K. & Kohmura, E. (2011). *J. Synchrotron Rad.* **18**:671-678.

Van Veelen, L.R., Cervelli, T., van de Rakt, M.W.M.M., Theil, A.F., Essers, J. & Kanaar, R. (2005). *Mutat. Res*. **574**:22-33.

Verheij, M. & Bartelink, H. (2000). *Cell Tissue Res.* **301**:133-142.

Wang, D. & Lippard, S.J. (2005). *Nature* **4**:307-320.

Washington, C.M. & Leaver, D.T. (2009). *Principles and practice of radiation therapy.* 3rd edition. Saint Louis (USA): Mosby editorial.

Winzel, E., Van der Merwe, E.J., Groenewald, W., Pistorius, S., Slabbert, J.P.,, Robinson, L. & Böhm, L. (1987). *S. Afr. Med. J.* **71**:693-695.

Yaes, R.J. & Kalend, A. (1988). *Int. J. Radiat. Oncol. Biol. Phys.* **14**:1247-1259.

Yongwon, J. & Lippard, S.J. (2007) *Chem. Rev.* **5**: 1387-1407.

Yuan, J., Adamski, R. & Chen, J. (2010). *FEBS Letters* **584**:3717-3724.

Zeman, W., Curtis, H.J., Gebhard, E.L. & Haymaker, W. (1959). *Science* **130**:1760-1761.

Zhang S.-C. (2001). *Nature Rev. Neurosci.* **2**: 840-842.

Zhou, P.K., Sproston, A.R.M., Marples, B., West, C.M., Margison, G.P. & Hendry, J.H. (1998). *Radiother. Oncol.* **47**:271-276.

Zong, W.-X. & Thompson, C.B. (2006). *Genes Dev.* **20**:1-15.